UNIVERSIDADE FEDERAL DE SANTA CATARINA
CENTRO TECNOLÓGICO
PROGRAMA DE PÓS-GRADUAÇÃO EM ENGENHARIA QUÍMICA - PósENQ

Francisco António Paquete Lima

Síntese e Caracterização de Óxido de Níquel e sua Aplicação na Reação de Desidrogenação Oxidativa de Etano

Florianópolis
2021

Francisco António Paquete Lima

Síntese e Caracterização de Óxido de Níquel e sua Aplicação na Reação de Desidrogenação Oxidativa de Etano

Tese submetida ao Programa de Pós-Graduação em Engenharia Química da Universidade Federal de Santa Catarina para a obtenção do título de Doutor em Engenharia Química
Orientador: Prof. Dr. Dachamir Hotza
Coorientador: Prof. Dr. Jean Guillaume Eon

Florianópolis
2021

Ficha de identificação da obra elaborada pelo autor,
através do Programa de Geração Automática da Biblioteca Universitária da UFSC.

Lima, Francisco António Paquete
Síntese e Caracterização de Óxido de Níquel e sua Aplicação na Reação de Desidrogenação Oxidativa de Etano / Francisco António Paquete Lima ; orientador, Dachamir Hotza, coorientador, Jean Guillaume Eon, 2021.
100 p.

Tese (doutorado) - Universidade Federal de Santa Catarina, Centro Tecnológico, Programa de Pós-Graduação em Engenharia Química, Florianópolis, 2021.

Inclui referências.

1. Engenharia Química. 2. Desidrogenação Oxidativa. 3. Etano. 4. Catalisador de Óxido de Níquel. 5. Defeitos. I. Hotza, Dachamir. II. Eon, Jean Guillaume . III. Universidade Federal de Santa Catarina. Programa de Pós Graduação em Engenharia Química. IV. Título.

Francisco António Paquete Lima

Síntese e Caracterização de Óxido de Níquel e sua Aplicação na Reação de Desidrogenação Oxidativa de Etano

O presente trabalho em nível de doutorado foi avaliado e aprovado por banca examinadora composta pelos seguintes membros:

Prof. Gizelle Inacio Almerindo, Dr.
Univali

Dr. Camilla Daniela Moura Nickel, Dr.
PosENQ/UFSC

Prof. Sergio Gomez, Dr.
PosENQ/UFSC

Certificamos que esta é a **versão original e final** do trabalho de conclusão que foi julgado adequado para obtenção do título de doutor em Engenharia Química.

Documento assinado digitalmente
Debora de Oliveira
Data: 27/10/2021 19:29:18-0300
CPF: 728.453.929-15
Verifique as assinaturas em https://v.ufsc.br

Coordenação do Programa de Pós-Graduação

Documento assinado digitalmente
Dachamir Hotza
Data: 27/10/2021 18:54:51-0300
CPF: 495.235.039-87
Verifique as assinaturas em https://v.ufsc.br

Prof. Dachamir Hotza, Dr.
Orientador

Florianópolis, 2021.

Este trabalho é dedicado a todos que de alguma forma contribuíram para a concretização desse processo.

AGRADECIMENTOS

O Deus pela saúde, a vida e por ter me acompanhado por todo tempo sempre indicando as melhores diretrizes na minha vida.

À minha Mãe e meu saudoso Pai, pelo amor incondicional pelos apoios nas minhas decisões, indicando sempre as melhores soluções, pelos conselhos, sempre buscando o melhor para mim.

Aos meus familiares, pela preocupação e pelos apoios em todos os sentidos, em especial as minhas irmãs pela infância inesquecível e pelos apoios e incentivos durante todos os momentos.

Aos meus orientadores pela orientação, incentivos, ensinamentos realizados ao longo do trabalho e a oportunidade em desenvolver este trabalho de pesquisa.

Aos professores e funcionários do PósENQ de uma forma geral, por compartilhar os conhecimentos durante o curso, em especial às Professoras Cíntia Soares e Débora de Oliveira e ao Chefe de Expediente Edevilson Silva, pelo auxílio e acompanhamento no início desse processo.

Aos meus conterrâneos e amigos, pelos momentos divididos ao longo desses anos que vou levar por toda a vida.

Aos colegas e colaboradores do grupo LabMASSA & LabSIN, pela amizade e momentos de descontração.

À Equipe Técnica dos laboratórios da IQ-UFRJ, pelos apoios oferecidos durante o desenvolvimento do trabalho e pelas análises físicas e químicas.

À Equipe Técnica dos Laboratórios LABNANO/CBPF (Rio de Janeiro) e LCME-UFSC, pelo suporte técnico durante a aquisição de micrografia eletrônica.

À Equipe Técnica do Laboratório CAEQA da UFSC, pelos apoios na caracterização físico-química.

À CAPES (processo nº 88882.345052/2019-01), pelo suporte financeiro para o desenvolvimento desse trabalho de pesquisa

E a todos que não foram citados, mas que contribuíram para o desenvolvimento desse trabalho de pesquisa, fica aqui o meu agradecimento.

RESUMO

Neste trabalho, foram investigados as propriedades e o comportamento catalítico de óxido de níquel na reação de desidrogenação oxidativa de etano em eteno (ODH), subdividido em três subseções: influência de precursores; efeito da temperatura de calcinação e efeito da concentração do promotor. Todas as amostras foram caracterizadas por XRD, FTIR, UV-Vis, SEM e TEM. A atividade catalítica e a seletividade na reação ODH foram quantificadas em linha por cromatografia gasosa. Na primeira estudou-se a influência do precursor, sintetizando seis precursores diferentes por diferentes métodos de síntese: α-hidróxido, β-hidróxido, hidróxido misto, nitro-hidróxido, carbonato básico e oxalato de níquel. Os óxidos obtidos apresentaram estrutura cúbica com diferentes graus de cristalinidade, tamanho de partícula, área superficial específica e morfologia. Os óxidos resultantes dos precursores carbonato básico e hidróxido misto apresentaram as maiores áreas superficiais de 197 e 155 m^2/g e partículas na ordem de 5 a 6 nm. O melhor desempenho catalítico foi atribuído ao precursor de hidróxido alfa com 22% de conversão e 66% de seletividade para etileno; nesse caso, o óxido apresentou estrutura esponjosa e porosa de diâmetro médio de 56 Å. Os ensaios realizados a 270 ° C mostraram uma variação da atividade intrínseca entre $4,24 \times 10^{-10}$ e $15,90 \times 10^{-10}$ $\mu mol.m^{-2}.s^{-1}$, e energia de ativação de 66-81 kJ/mol. O óxido obtido a partir do α-$Ni(OH)_2$ apresentou maior rendimento e menor energia do band gap, 2,69 eV, em relação aos demais, denotando a possibilidade de sua influência no desempenho catalítico da reação etano ODH. Na segunda subseção, foi selecionado o β-$Ni(OH)_2$ sintetizado por precipitação-oxidação para estudar o efeito do tratamento térmico na propriedade dos óxidos. Assim como na seção anterior, os produtos obtidos apresentaram estrutura cúbica de NiO puro com diferentes graus de cristalinidade, tamanho do cristalito e área de superfície específica. O aumento da temperatura de calcinação causou um aumento no tamanho médio do cristalito de 28 Å a 250 ° C para 104 Å a 400 ° C, enquanto a forma das partículas não apresentou diferenças significativas; o diâmetro do poro aumentou de 35 Å para 69 Å e a área de superfície específica diminuiu de 245 m^2/g para 82 m^2/g. O teste realizado a 240 °C mostrou um decréscimo na conversão, de 8,75% para 4,25%; as amostras mais cristalinas apresentaram a maior atividade intrínseca com seletividade ao eteno próxima a 60%. Nenhuma influência da energia de band gap nas propriedades catalíticas foi observada. Na subseção três, foi investigado o efeito de dopagem por cátions Na^+ nas propriedades e no comportamento catalítico de soluções sólidas de NiO. Um planejamento fatorial 2^3 com ponto central em triplicata foi utilizado para avaliar o efeito de três parâmetros independentes (tempo de reação, temperatura de lavagem e temperatura de calcinação) e sua influência na atividade catalítica de cada amostra. Além disso, foram estudadas propriedades como a composição, tamanho de partícula, tamanho de cristalito, energia de gap óptico e como eles influenciam a atividade e seletividade das amostras. Os resultados indicaram a formação de estrutura cristalina homogêneo com a mesma estrutura do óxido de níquel inicial, indicando a formação da solução sólida. Altas concentrações de Na^+ resultaram na diminuição da atividade catalítica, mas apresentando melhor seletividade ao etileno. Baixas concentrações de Na^+ apresentaram um aumento da atividade catalítica, correspondendo a uma conversão de 22%, mas com seletividade moderada ao etileno entre 66-68%. A temperatura de calcinação foi o fator maior influência para a tamanho do cristal de NiO. Os melhores rendimentos ao etileno e a maior estabilidade nas condições de reação foram obtidos nos catalisadores de baixas concentrações de Na^+. Demonstrou-se que a introdução de sódio foi benéfica para ODH, aumentando a seletividade do eteno para valores maiores que 90% com uma queda relativamente pequena na reatividade para o etano conforme a concentração de sódio aumenta.

Palavras-chave: Desidrogenação Oxidativa. Etano, Catalisador de Óxido de Níquel. Oxigênio Estequiometria. Defeitos e Vacância. Solução Sólida. Íons Dopantes, Planejamento Fatorial.

RESUMO EXPANDIDO

Introdução

O aumento da demanda mundial por olefinas leves demostra a sua importância como matéria-prima ou intermediário na cadeia produtiva de alguns setores industriais em crescimento como petroquímicas e automobilístico [1, 2]. Toda a produção mundial das olefinas, atualmente é via processos tradicionais de craqueamento catalítico a vapor (*stream cracking*) e FCC, muito extensivo em consumo energético [3, 4]. A busca por eficiência energética aliado ao baixo preço do gás natural (etano) vem impulsionado o desenvolvimento de tecnologia alternativas para a produção do eteno. Uma rota promissora e muito investigada é a desidrogenação oxidativa de etano (*oxidative dehydrogenation*, ODH) [5, 6]. As principais vantagens desta tecnologia são o menor consumo energético, alta atividade e seletividade para olefinas em baixa temperatura [6]. Historicamente, a reação ODH não é usada na produção de etileno em larga escala, por não ser uma tecnologia economicamente atrativa em função da atividade e seletividade dos catalisadores utilizados na reação atualmente. Esse problema tornou-se um desafio para pesquisadores tanto na catálise aplicada quanto na academia. A solução seria o desenvolvimento de catalisadores capazes de ativar ligação estável de C – H [7, 8] em uma molécula de alcano e, ao mesmo tempo, prevenir as reações consecutivas dos produtos etileno, que é mais reativo que o etano [1, 9, 10]. Nesse contexto, diversos materiais com propriedades redox têm sido desenvolvidos e aplicados com o objetivo de auxiliar no entendimento do mecanismo de reações em nível molecular em fase gasosa, adsorção de reagentes e dessorção do produto formado [6]. A grande maioria dos catalisadores propostos como ativos para a reação ODH do etano se enquadra na categoria de metais redox ativos e seguem o mecanismo de Mars-van Krevelen [11]. Dentre os catalisadores explorados temos de óxido baseados em metais de transição, como molibdênio, [12] vanádio [13–15] e níquel, [16–18], assim como misturas entre eles. Uma das misturas de melhor desempenho a baixa temperatura e com eficiência relativamente alta é óxidos de Mo–V–Nb [19]. Essa combinação óxido metálico misto com adição de outros elementos tem ganhado preferência para reação ODHE, no entanto, a preparação complicada limita sua aplicação prática [20]. O óxido de níquel também tem atraído considerável interesse e apresenta como um promissor e potencial candidato e para catalisar a reação ODH de etano a baixas temperaturas, mas o entendimento e melhorar suas propriedades catalíticas se tornam necessária [17, 18, 21].

O óxido de níquel puro e estequiométrico é um composto isolante de cor verde com estrutura do sal NaCl. No entanto, quando preparado a partir da decomposição térmica de sais de níquel na presença de ar é considerado um semicondutor do tipo p cristalino não estequiométrico com excesso de ânions de oxigênio da rede NiO_x, onde $x \approx 1$ [22–24]. A não estequiometria é acompanhada por uma mudança de cor de verde para preto ou cinza-preto devido à existência de vacâncias catiônicas (Ni^{2+}) na rede de cristal de NiO [25]. A presença de vacâncias catiônicas (Ni^{2+}) causa a oxidação de dois íons Ni^{2+} ao redor da vacância para íons Ni^{3+} para obter neutralidade [26]. Os íons Ni^{3+} ou buracos (h^+) considerados como principais portadores de carga são responsáveis pela melhoria na conversão de etano devido à geração de espécies eletrofílicas O^- ($h^+ + O^{2-} \rightarrow O^-$) [8, 24]. Tanto o excesso de oxigênio quanto as vacâncias tendem a desempenhar um papel importante na atividade e seletividade nas reações de desidrogenação oxidativa do etano [27]. No entanto, as propriedades catalíticas (atividade e seletividade) também são determinadas pelo tamanho, forma e morfologia das partículas de catalisador, áreas de superfície específicas, bem como a estrutura local do sítio ativo [28, 29]. O fator chave na obtenção de óxidos de níquel com diferentes propriedades tem

sido o uso de diferentes precursores e métodos de preparação [30]. Como relatado por Ying Wu, et al. [31] as nanopartículas de NiO quando sintetizadas por diferentes métodos, como moagem de estado sólido, precipitação, sol-gel e microemulsão reversa mostrando vários diâmetros, formas e distribuições de tamanho. Essas variações também foram observadas no tamanho das partículas e na área superficial que influenciam a propriedade adsortiva, que tem íntima conexão com seu comportamento catalítico [32, 33].

A temperatura de decomposição dos sais de níquel também tem influência nas propriedades físico-químicas do NiO como tamanho do cristalito, área superficial, tamanho e volume dos poros, energia do gap, entre outros [21, 34]. Como observado por Abbas e Jung [35], o aumento da temperatura de calcinação do α-$Ni(OH)_2$ mesoporoso causou a diminuição da área de superfície e do volume dos poros das amostras microesféricas de NiO. Comportamentos semelhantes de área de superfície e volume de poro foram observados por Lin, et al. [36] durante a decomposição térmica do $Ni(OH)_2$ sintetizado pelo método sol-gel. Esses autores também observaram um aumento do tamanho médio do cristalito com o aumento da temperatura de calcinação. Outros pesquisadores [37] constataram que o aumento do tamanho médio do cristalito dos filmes de NiO com a temperatura de recozimento é acompanhado por uma diminuição no gap óptico.

As imperfeições químicas (defeitos) incluem lacunas e a incorporação de elementos diferentes (impurezas). A incorporação de impurezas ou promotores por dopagem da rede com cátion de metal secundário para formar uma estrutura de solução sólida, tem sido explorado para a melhoria do desempenho catalítico ou eletroquímico do óxido de níquel. [26, 38]. Dependendo da aplicação, a rede de óxido pode ser dopada por cátion de metal monovalente Li^+, Na^+, Ag^+, divalente Mg^{2+}, Ca^{2+}, Zn^{2+} trivalente In^{3+}, Ga^{3+}, Cr^{3+} ou estados de alta valência Sn^{4+} Ti^{4+}, Ta^{5+} Nb^{5+}, W^{5+}. [27, 39–47]. Os efeitos da dopagem de íons univalentes, divalentes e trivalentes ou de estados de alta valência resultam da diminuição ou aumento da concentração de cátions Ni^{3+} no óxido de níquel. A adição de cátions metálicos monovalentes na rede de NiO geralmente leva a um aumento na quantidade de cátions Ni^{3+}, aumentando assim a atividade [40, 44]. Ao contrário da dopagem univalente que produz buracos (íons Ni^{3+}), um íon trivalente substituindo o Ni^{2+} que será eletricamente compensado pela formação de lacunas de níquel adjacentes simples ou duplamente ionizadas, ou então pelo excesso de elétrons. Assim como o trivalente, os estados de alta valência na rede de NiO geralmente levam a uma diminuição na quantidade de Ni^{3+}, o que pode alterar o desempenho da reação dos catalisadores obtidos [27, 43]. Entre os íons metálicos aplicados na dopagem com NiO, o íon nióbio é o mais estudado para melhorar a seletividade do etileno na reação de desidrogenação oxidativa do etano, devido ao fato de que cátions Nb^{5+} preenchem as lacunas de Ni^{2+} em vez de substituir os cátions Ni^{2+} na rede NiO [48].

As propriedades de NiO dopado com íons monovalentes, particularmente lítio (íons Li^+), têm sido estudadas extensivamente. No entanto, apenas alguns pesquisadores relataram o efeito dos íons sódio nas propriedades do NiO. Isso pode estar relacionado ao fato de que o tamanho do raio iônico do íon de lítio ser muito próximo ao Ni^{2+}, assim o íon de lítio pode ser facilmente dopado em óxido de níquel até certo limite. O óxido de níquel dopado tende a mostrar célula unitária de rede semelhante em comparação com óxido de níquel puro não dopado [49]. De acordo com o balanço de massa e a neutralidade elétrica, o óxido de níquel dopado produzirá íons Ni^{3+} adjacente ao Li^+ [50]. Foi estabelecido que as propriedades semicondutoras e catalíticas do óxido de níquel dependem do defeito estrutural e da composição da superfície. De acordo com a regra da neutralidade de carga, a introdução de sódio (Na^+) no óxido também pode levar à formação de íons Ni^{3+} e diminuição da concentração de íons Ni^{2+} na rede de óxidos [51]. Além disso, a presença de cátions de metais alcalinos como o sódio, além de modificar o equilíbrio dos defeitos, também altera a acidez dos óxidos de níquel por ser considerada base forte, de acordo com Pearson [52].

A adição de aditivos como metal alcalino ao sistema de óxido pode modificar propriedades ácido-básicas e energia de ligação metal-oxigênio com efeito benéfico na seletividade para olefinas na reação de ODH de alcanos leves. Grabowski et al. [53] demonstrou esse efeito para a reação ODH do propano a partir de catalisadores $_{VOx}$ / TiO_2 e MoO_x / TiO_2 com adição de Li, K e Rb. O mesmo comportamento foi observado por Chen et al. [54] usando catalisadores MoO_x / ZrO_2 com Li, K e Cs para a reação ODH do propano. Martin-Aranda et al [55] também observaram o mesmo comportamento na reação ODH do butano sobre o molibdato de níquel com adição de Li, Na, K e Cs. O estudo das propriedades ácido-básicas e redox e os dados catalíticos deste sistema podem ser úteis para o entendimento do mecanismo e a ação dos catalisadores óxidos nas reações ODH.

Este trabalho está estruturado com uma parte introdutória apresentando uma visão geral dos temas abordados e os objetivos gerais e específicos, seguido pela descrição das metodologias empregadas, apresentação e discussão dos resultados obtidos e por último as considerações finais e as perspectivas para trabalhos futuros. Foram propostos e estudados três temas em subseções: influência de precursores; efeito da temperatura de calcinação e efeito da concentração do promotor. Na subseção um foi propostos e discutidos diferentes métodos de preparação de óxido de níquel a partir de vários precursores para comparar os efeitos do tamanho, a morfologia e as facetas expostas, atribuído de forma empírica e ambígua ao desempenho catalítico. Na subseção dois, foi analisada a influência da temperatura de calcinação na morfologia, na energia do band-gap no desempenho catalítico do óxido de níquel na reação ODH do etano em etileno. Os materiais foram obtidos a partir de β-$Ni(OH)_2$ sintetizado por precipitação-oxidação seguida de tratamento térmico em ar em diferentes temperaturas. Na subseção três, foi investigado o efeito da dopagem dos cátions Na^+ nas propriedades e no comportamento catalítico de soluções sólidas de NiO obtido a partir do tratamento térmico de hidróxido de níquel. Um planejamento fatorial 2^3 com ponto central em triplicado foi utilizado para avaliar o efeito de três parâmetros independentes (tempo de reação, temperatura de lavagem e temperatura de calcinação) e sua influência na atividade catalítica de cada amostra. Todas as amostras de óxido não estequiométrico desse trabalho foram estudadas por difração de raios-X (XRD), infravermelho com transformada de Fourier (FTIR), espectrofotometria ultravioleta-visível (UV-vis) e microscopia eletrônica de varredura (SEM) e de transmissão (TEM).

Objetivos

O objetivo deste trabalho foi estudar as preparações, as propriedades físicas e químicas e a atividade catalítica do óxido de níquel na reação de desidrogenação oxidativa de etano, visando à verificação da influência do precursor, a temperatura de tratamento e aditivos no desempenho catalítico.

Objetivos Específicos

- Obter óxidos de níquel a partir de diferentes percursores adotando diversos métodos de síntese.
- Caracterizar os óxidos bem como os seus respectivos precursores através de técnicas físicas e químicas
- Avaliar a influência dos percursores e do método de preparação, da temperatura de tratamento na propriedade como do desempenho catalíticos dos óxidos.
- Avaliar a influência do aditivo tanta na propriedade como do desempenho catalíticos dos óxidos obtidos por dopagem

•Avaliar a influência dos parâmetros sugerida no planejamento experimental nas propriedades e no desempenho catalítico dos óxidos.

Metodologia

Para a avaliação da influência do precursor nas propriedades e no desempenho catalítico, os óxidos de níquel foram obtidos a partir da calcinação a 350 °C dos diferentes sais de níquel. Os precursores sintetizados e os respectivos métodos de preparação foram os seguintes: alpha hidróxido de níquel (coprecipitação invertida), o beta hidróxido (coprecipitação oxidativa), hidroxi-nitrato (solvotérmica), carbonato básico (hidrotermal) e oxalato de níquel (coprecipitação). Para a avaliação do efeito da temperatura de tratamento foi selecionado o beta-hidróxido de níquel que se decompõe em óxido a menor temperatura, oferecendo maior faixa de temperatura de calcinação (250° - 400 °C) para o estudo. Os óxidos dopados com (Na^+) foram obtidos a partir hidróxidos alpha. Para avaliação a influência e a interação entre alguns parâmetros sintéticos sobre as propriedades e o desempenho catalítico, a etapa final do processo foi conduzido por um planejamento experimental fatorial 2^3.

As fases dos precursores assim com os seus respectivos óxidos foram investigados e identificados a partir dos difratogramas de raios-X complementadas com as informações dos espectros de FTIR para identificação das espécies presente. Para a determinação da área superficial dos sólidos utilizamos o método desenvolvido por (Brunauer, Emmet e Teller, BET) através das isotermas de adsorção e dessorção de nitrogênio. A concentrações proporcionais nos íons Ni(II) e Ni(III) bem como o calculo da energia de gap óptico fora obtido através da análises e transformação dos dados do espectro de refletância difusa de UV-visível. A fluorescência de raios-X (FRX) foi utilizada para avaliação semi-quantitativa dos componentes químicos das amostras de óxido dopadas com cátions de sódio. A avaliação da morfologia e a distribuição do tamanho das partículas foram estudadas com auxílio de microscopia eletrônica de varredura e de transmissão. Os ensaios catalíticos foram realizados a pressão atmosférica, usando um microrreator de leito fixo colocado no interior de um forno tubular elétrico. O fluxo da mistura gasosa e a temperatura da reação foram controlados eletronicamente. Os reagentes e produtos da reação foram analisados usando cromatografia em fase gasosa conectada em linha com o reator. O programa *Statistica* versão 7.0 foi usado para avaliar os efeitos dos fatores principais e de interação resultantes do planejamento fatorial. A análise de variância foi utilizada para avaliar o efeito das variáveis independentes na resposta por meio do modelo matemático.

Resultados e Discussão

Todos os precursores estudados (alpha hidróxido - AH, beta hidróxido - BH, hidroxi-nitrato - HN, carbonato básico - BC e oxalato de níquel - OX) demonstraram a formação das suas respectivas fases quando comparadas com as fases de referência da base ICSD ou dos artigos publicados. Os difratograma de raios-X dos óxidos obtidos a partir da calcinação dos sais apresentaram estrutura cúbica de NiO, quando indexados com o padrão da base ICSD. O cálculo do tamanho de cristalito dos óxidos a partir dos dados do difratogamas apresentaram valores distintos: MH (61 Å) < AH (62 Å) < BH (70 Å) < BC (85 Å) < HN (107 Å) < OX (168 Å). A maior área especifica foi observado do oxido obtido a partir de carbonato básico, de acordo com a seguinte sequência: OX (74 m^2/g) < HN (105 m^2/g) < AH (127 m^2/g) < BH (131 m^2/g) < MH (155 m^2/g) < BC (197 m^2/g). O diâmetro médio dos poros aumentou nesta sequência: AH (56 Å) < BH (57 Å) < HN (75 Å) < OX (109 Å) < BC (128 Å). As diferentes áreas superficiais BET e diâmetro médio dos poros para cada precursor, reafirmando sua influência nas propriedades dos óxidos. Em termo de morfologia as imagens da microscopia de varredura para os óxidos obtidos a partir do alfa hidróxido (AH), do hidróxido misto (MH) e do carbonato básico (BC) apresentam aglomerados de partículas em forma de placas. No

entanto, o grau de aglomeração de partículas varia de acordo com o precursor, resultando em uma variação significativa na área de superfície medida por BET. As imagens para os óxidos dos precursores de hidróxido beta (BH), nitro-hidróxido (NH) e oxalato de níquel revelaram uma heterogeneidade de tamanho de partícula, a maioria com dimensões superiores 1 μm e estruturas como esponja, flores e lamelares respectivamente. O melhor desempenho catalítico em termo da conversão, seletividade e o rendimento a 310 °C foi observados no óxido obtido a partir dos alpha hidróxido. Para o ensaio conduzido a 270 °C a conversão seguiu esta ordem: HN (3,56 %) < OX (8,88 %) < MN (8,93 %) < BH (11,27 %) < AH (13,05 %) < BC (17,21 %) e a seletividade a eteno HN(41 %) < BC (52 %) < BC (58 %) < AH (62 %)< MN (63 %)< OX (65 %). Para a reação de etano a 270 °C a atividade específica segue a sequência: HN < MH < BH < BC < AH < OX. No entanto, as energias de ativação aparentes apresentou valores menores para o oxalato, e maiores para o precursor de carbonato de níquel básico, seguindo essa ordem: OX (66 kJ/mol) <MH (69 kJ/mol) <BH (70 kJ/mol) <AH (75 kJ/mol) <HN (80 kJ/mol) <BC (81 kJ/mol).

A análise dos difratogramas obtidos após o tratamento térmico do beta hidróxido de níquel a diferente temperatura (250 a 400 °C) demostraram a formação da estrutura cúbica de NiO aumentando a cristalinidade com a temperatura de calcinação, assim como os valores do tamanho de cristalito calculado. As áreas de superfície BET apresentam comportamento semelhante ao encontrado por Abbas e Jung [56] após calcinação de α-$Ni(OH)_2$ mesoporoso. As partículas coalescem durante o aumento da temperatura, levando a um aumento do tamanho das partículas e à diminuição de áreas de superfície específicas. A análise dos dados dos espectros de refletância difusa de UV-visível observa-se que os picos atribuídos aos íons Ni (III) em relação ao Ni (II) aumentam proporcionalmente para a amostra calcinada de 250 a 300 °C e de 300 a 350 °C, mas diminuem de 350 a 400 °C. Os valores de energia do *bandgap* obtidos também presentaram o mesmo comportamento com o maior valor para amostra NiO-350 (3,41 eV). As imagem da microscopia de varredura para estas amostras apresentaram uma heterogeneidade de tamanhos de partícula, maiores que 1 μm de estruturas laminares esponjosas de alta porosidade. A amostra NiO-300 exibiu o melhor desempenho catalítico em termo de conversão, seletividade e rendimento com o aumento da temperatura de reação. Para a reação a 240 °C as amostras apresentaram seletividade crescente nesta sequência: NiO-250 = NiO-400 <NiO-300 = NiO-350 e a conversão segue uma ordem diferente: NiO-250> NiO-300> NiO-350> NiO-400. A reação realizada a 240 ° C, 270 ° C e 310 ° C mostra um aumento da atividade intrínseca com o aumento da temperatura de calcinação das amostras. As energias de ativação aparentes, no entanto, são todas similarmente: NiO-250 (78.4 kJ / mol), NiO-300 (77.8 kJ / mol), NiO-350 (74.7 kJ / mol) e NiO-400 (76.6 kJ / mol). Os resultados sugerem que os valores de energia de ativação aparente seguem qualitativamente os teores de Ni (III) de acordo com as curvas UV-Vis.

Os estudos radiográficos das amostras de NiO dopadas com cátions Na^+ formaram uma fase cristalina homogênea a mesma estrutura cúbica do óxido de níquel, indicando a formação da solução sólida. O estudo do efeito de variáveis independentes mostrou que a temperatura de lavagem e de calcinação foram os fator mais influente nas propriedades físico-químicas e no comportamento catalíticas de soluções sólidas de NiO formadas. A análise dos efeitos mostrou que a temperatura de calcinação foi o fator de efeito mais significativo sobre o tamanho do cristal, com contribuições de 81,39 com pequena contribuição de outros três fatores. O termo quadrático da temperatura de lavagem foi o único fator de efeito significativo para a composição de uma amostra. A análise dos efeitos mostraram que a temperatura de lavagem e o tempo de reação tiveram efeito significativo sobre Eg e apenas a interação entre a temperatura de calcinação e a temperatura de lavagem apresentou efeitos significativos. As imagens de microscopia de varredura mostraram aglomerados de partículas em forma de

placas porosas sem diferenças significativas na morfologia. Foi observados nas imagens de microscopia de transmissão das amostras de NiO essencialmente nanopartículas de diâmetro médio de 5 nm. A amostra E-2 exibiu o melhor desempenho catalítico em termo de conversão (22%) e rendimento a 270 °C e a amostra E-9 em termo de seletividade (92%). A reação a 270 °C a seletividade crescente nesta sequência: E-4 <E-2 <E-3 <E-1 <E6 <E-8 <E-5 = E11 <E-10 <E-7 = E -9. A conversão seguiu uma ordem diferente: E-2> E-3> E-4> E-1> E11> E-6 <E-5> E-7 = E-8 = E-10> E-9. Os testes realizados a 270 °C mostraram uma tendência para diminuir a conversão com o aumento da seletividade. A análise dos efeitos mostrou que a temperatura de calcinação é o único fator significativo para a conversão. Para a seletividade o termo quadrático da temperatura de lavagem foi o único fator de efeito significativo. As amostras com a maior concentração de sódio apresentaram a menor conversão sugerindo um efeito inibitório sobre a atividade. Ao contrário da conversão, a presença de sódio tem um efeito benéfico na seletividade. As amostras com maior concentração de sódio apresentaram o melhor desempenho em termos de seletividade. As amostras com menor teor de sódio apresentaram melhor atividade e baixa seletividade e as mais seletivas apresentaram baixa atividade, um problema típico de desativação por envenenamento.

Considerações Finais

Os precursores, a temperatura de tratamento e a concentração do promotor demonstraram efeito tanto nas propriedades físico-químicas quanto no comportamento catalítico na reação de desidrogenação oxidativa do etano. Na influência do precursor se destaca o comportamento catalítico do NiO na reação, resultando em diferente conversões para cada catalisador testado. Esta diferença foi atribuída de forma empírica à morfologia das partículas, principalmente a microtopografia da superfície exposta que apresentaram estrutura diferente para cada óxido nas imagens da microscopia eletrônica de varredura. A energia de ativação aparente foi considerada independente do conteúdo de Ni (III) e da energia do band-gap para os óxidos calcinados a diferentes temperaturas. Embora a atividade do óxido tenha diminuído com a calcinação, conforme esperado pela diminuição da área específica, observamos que amostras mais cristalina apresentaram a maior atividade intrínseca. Sugerindo que o melhor desempenho catalítico dos catalisadores de NiO devem ter alta cristalinidade e grande área de superfície. A solução sólida de óxidos mistos de níquel demonstrou o grande efeito do dopante nas propriedades físico-químicas e no comportamento catalítico. A atividade catalítica diminuiu com a concentração de Na^+, mas mostrou a melhor seletividade ao etileno. As baixas concentrações de Na^+ mostraram aumento da atividade catalítica, mas com moderada seletividade ao etileno. Portanto, a adição de sódio indicou benefícios promissores para o etano ODH, com aumento da seletividade do eteno e uma queda relativamente pequena na conversão para o etano à medida que a concentração de sódio aumenta.

Referências

1. Zimmermann H, Walzl R (2009) Ethylene. In: Ullmann's Encyclopedia of Industrial Chemistry. Wiley-VCH Verlag GmbH & Co. KGaA, Weinheim, Germany, pp 797–809

2. Tullo AH (2003) PETROCHEMICALS. Chem Eng News Arch 81:21–26. doi: 10.1021/cen-v081n011.p021

3. Ren T, Patel M, Blok K (2006) Olefins from conventional and heavy feedstocks: Energy use in steam cracking and alternative processes. ENERGY 31:425–451. doi:

10.1016/j.energy.2005.04.001

4. Meyers RM and RA (2005) Handbook of Petrochemicals Production Processes, Third. McGraw-Hill Education

5. Cavani F, Trifirò F (1995) The oxidative dehydrogenation of ethane and propane as an alternative way for the production of light olefins. Catal Today 24:307–313. doi: 10.1016/0920-5861(95)00051-G

6. Gärtner CA, vanVeen AC, Lercher JA (2013) Oxidative dehydrogenation of ethane: Common principles and mechanistic aspects. ChemCatChem 5:3196–3217. doi: 10.1002/cctc.201200966

7. Zboray M, Bell AT, Iglesia E (2009) Role of C-H Bond Strength in the Rate and Selectivity of Oxidative Dehydrogenation of Alkanes. J Phys Chem C 113:12380–12386. doi: 10.1021/jp901595k

8. Varghese JJ, Mushrif SH (2017) Insights into the C-H Bond Activation on NiO Surfaces: The Role of Nickel and Oxygen Vacancies and of Low Valent Dopants on the Reactivity and Energetics. J Phys Chem C 121:17969–17981. doi: 10.1021/acs.jpcc.7b05226

9. Stephen Craig Arnold ML, Anne Mae Gaffney WC, Ruozhi Song W, Chuen Yuan Yeh E (2010) Process for producting ethylene via oxidative dehydrogenation (ODH) of ethane. 1:1–5

10. Grabowski R (2006) Kinetics of oxidative dehydrogenation of C2-C3alkanes on oxide catalysts. Catal Rev - Sci Eng 48:199–268. doi: 10.1080/01614940600631413

11. Mars P, van Krevelen DW (1954) Oxidations carried out by means of vanadium oxide catalysts. Chem Eng Sci 3:41–59. doi: 10.1016/S0009-2509(54)80005-4

12. Tsilomelekis G, Christodoulakis A, Boghosian S (2007) Support effects on structure and activity of molybdenum oxide catalysts for the oxidative dehydrogenation of ethane. Catal TODAY 127:139–147. doi: 10.1016/j.cattod.2007.03.026

13. Argyle MD, Chen KD, Bell AT, Iglesia E (2002) Ethane oxidative dehydrogenation pathways on vanadium oxide catalysts. J Phys Chem B 106:5421–5427. doi: 10.1021/jp0144552

14. Martinez-Huerta M V, Gao X, Tian H, et al (2006) Oxidative dehydrogenation of ethane to ethylene over alumina-supported vanadium oxide catalysts: Relationship between molecular structures and chemical reactivity. Catal TODAY 118:279–287. doi: 10.1016/j.cattod.2006.07.034

15. LeBars J, Auroux A, Forissier M, Vedrine JC (1996) Active sites of V2O5/gamma-Al2O3 catalysts in the oxidative dehydrogenation of ethane. J Catal 162:250–259. doi: 10.1006/jcat.1996.0282

16. Heracleous E, Lemonidou AA (2006) Ni-Nb-O mixed oxides as highly active and selective catalysts for ethene production via ethane oxidative dehydrogenation. Part II: Mechanistic aspects and kinetic modeling. J Catal 237:175–189. doi: 10.1016/j.jcat.2005.11.003

17. Skoufa Z, Heracleous E, Lemonidou AA (2015) On ethane ODH mechanism and nature of active sites over NiO-based catalysts via isotopic labeling and methanol sorption studies. J Catal 322:118–129. doi: 10.1016/j.jcat.2014.11.014

18. Popescu I, Skoufa Z, Heracleous E, et al (2015) A study by electrical conductivity measurements of the semiconductive and redox properties of Nb-doped NiO catalysts in correlation with the oxidative dehydrogenation of ethane. Phys Chem Chem Phys 17:8138–8147. doi: 10.1039/c5cp00392j

19. Thorsteinson EM, Wilson TP, Young FG, Kasai PH (1978) The oxidative dehydrogenation of ethane over catalysts containing mixed oxides of molybdenum and vanadium. J Catal 52:116–132. doi: 10.1016/0021-9517(78)90128-8

20. Botella P, Garcia-Gonzalez E, Dejoz A, et al (2004) Selective oxidative dehydrogenation of ethane on MoVTeNbO mixed metal oxide catalysts. J Catal 225:428–438. doi: 10.1016/j.jcat.2004.04.024

21. Dubey P, Kaurav N, Devan RS, et al (2018) The effect of stoichiometry on the structural, thermal and electronic properties of thermally decomposed nickel oxide. RSC Adv 8:5882–5890. doi: 10.1039/c8ra00157j

22. N. N. Greenwood And A. Earnshaw (1997) Chemistry of the Elements, Oxford: Pe. Butterworth-Heinemann

23. Zhang KHL, Xi K, Blamire MG, Egdell RG (2016) P-type transparent conducting oxides. J Physics-Condensed Matter 28:. doi: 10.1088/0953-8984/28/38/383002

24. Gray TJ, darby PW (1956) Semi-conductivity and catalysis in the nickel oxide system. J Phys Chem 60:209–217. doi: 10.1021/j150536a017

25. Boschloo G, Hagfeldt A (2001) Spectroelectrochemistry of nanostructured NiO. J Phys Chem B 105:3039–3044. doi: 10.1021/jp003499s

26. Cox PA (1987) The Electronic Structure and Chemistry of Solids. Oxford University Press, New York

27. Savova B, Loridant S, Filkova D, Millet JMM (2010) Ni-Nb-O catalysts for ethane oxidative dehydrogenation. Appl Catal A-general 390:148–157. doi: 10.1016/j.apcata.2010.10.004

28. Henry CR (1998) Surface studies of supported model catalysts. Surf Sci Rep 31:235–325

29. Taylor HS, A PRSL (1925) A theory of the catalytic surface. Proc R Soc London Ser A, Contain Pap a Math Phys Character 108:105–111. doi: 10.1098/rspa.1925.0061

30. Roldan Cuenya B (2010) Synthesis and catalytic properties of metal nanoparticles: Size, shape, support, composition, and oxidation state effects. Thin Solid Films 518:3127–3150. doi: 10.1016/j.tsf.2010.01.018

31. Wu Y, He Y, Wu T, et al (2007) Effect of synthesis method on the physical and catalytic property of nanosized NiO. Mater Lett 61:2679–2682. doi: 10.1016/j.matlet.2006.10.022

32. Kang YC, Park SB, KANG YW (1995) Preparation of high-surface-area nanophase particles by low-pressure spray-pyrolysis. Nanostructured Mater 5:777–791. doi: 10.1016/0965-9773(95)00289-Q

33. Xie X, Shen W (2009) Morphology control of cobalt oxide nanocrystals for promoting their catalytic performance. Nanoscale 1:50–60. doi: 10.1039/b9nr00155g

34. Zhu Z, Wei N, Liu H, He Z (2011) Microwave-assisted hydrothermal synthesis of Ni(OH)(2) architectures and their in situ thermal convention to NiO. Adv powder Technol 22:422–426. doi: 10.1016/j.apt.2010.06.008

35. Abbas SA, Jung K-D (2016) Preparation of mesoporous microspheres of NiO with high surface area and analysis on their pseudocapacitive behavior. Electrochim Acta 193:145–153. doi: 10.1016/j.electacta.2016.02.054

36. Lin C, Al-Muhtaseb SA, Ritter JA (2003) Thermal treatment of sol-gel derived nickel oxide xerogels. J SOL-GEL Sci Technol 28:133–141. doi: 10.1023/A:1025653607374

37. Akinkuade S, Mwankemwa B, Nel J, Meyer W (2018) Structural, optical and electrical characteristics of nickel oxide thin films synthesised through chemical processing method. Phys b-condensed matter 535:24–28. doi: 10.1016/j.physb.2017.06.021

38. Zhang Y, Zhou YJ, Lin JP, et al (2008) Solid-solution phase formation rules for multi-component alloys. Adv Eng Mater 10:534–538. doi: 10.1002/adem.200700240

39. Turky AM (2003) Electrical surface and catalytic properties of NiO as influenced by doping with CuO and Ag2O. Appl Catal A-GENERAL 247:83–93. doi: 10.1016/S0926-860X(03)00089-9

40. Heracleous E, Lemonidou AA (2010) Ni-Me-O mixed metal oxides for the effective oxidative dehydrogenation of ethane to ethylene - Effect of promoting metal Me. J Catal 270:67–75. doi: 10.1016/j.jcat.2009.12.004

41. Solsona B, Lopez Nieto JM, Concepcion P, et al (2011) Oxidative dehydrogenation of ethane over Ni-W-O mixed metal oxide catalysts. J Catal 280:28–39. doi: 10.1016/j.jcat.2011.02.010

42. Solsona B, Concepcion P, Demicol B, et al (2012) Selective oxidative dehydrogenation of ethane over SnO2-promoted NiO catalysts. J Catal 295:104–114. doi: 10.1016/j.jcat.2012.07.028

43. Zhu H, Ould-Chikh S, Anjum DH, et al (2012) Nb effect in the nickel oxide-catalyzed low-temperature oxidative dehydrogenation of ethane. J Catal 285:292–303. doi: 10.1016/j.jcat.2011.10.005

44. Li Y, Li X, Wang Z, et al (2016) One-step synthesis of Li-doped NiO as high-performance anode material for lithium ion batteries. Ceram Int 42:14565–14572. doi: 10.1016/j.ceramint.2016.06.071

45. Lopez Nieto JM, Solsona B, Grasselli RK, Concepcion P (2014) Promoted NiO Catalysts for the Oxidative Dehydrogenation of Ethane. Top Catal 57:1248–1255. doi: 10.1007/s11244-014-0288-2

46. Schwab GM, Schmid H (1962) Effect Of Added Oxides On P-Conducting Nickel Oxide. J Appl Phys 33:426-. doi: 10.1063/1.1777135

47. Meier GH, Rapp RA (1971) Electrical Conductivities and Defect Structures of Pure NiO and Chromium-Doped NiO. Zeitschrift Fur Phys Chemie-Frankfurt 74:168-. doi: 10.1524/zpch.1971.74.3_6.168

48. Heracleous E, Lemonidou AA (2006) Ni-Nb-O mixed oxides as highly active and selective catalysts for ethene production via ethane oxidative dehydrogenation. Part I: Characterization and catalytic performance. J Catal 237:162–174. doi: 10.1016/j.jcat.2005.11.002

49. Van Houten S (1960) Semiconduction in Lixni(1-X)O. J Phys Chem Solids 17:7–17. doi: 10.1016/0022-3697(60)90169-4

50. Bosman AJ, Crevecoeur C (1966) Mechanism of Electrical Conduction in Li-Doped NIO. Phys Rev 144:763+. doi: 10.1103/PhysRev.144.763

51. Panagopoulos CN, Eloui S (1986) A Study af Na Doped NiO Surface. Zeitschrift Fur Phys Chemie-Leipzig 267:608–612

52. Pearson RG (1963) Hard and Soft Acids and Bases. J Am Chem Soc 85:3533–3539. doi: 10.1021/ja00905a001

53. GrabowskI R, grzybowska B, SAMSON K, et al (1995) Effect of Alkaline Promoters on Catalytic Activity of V2O5/TiO2 and MoO3/Tio2 Catalysts in Oxidative Dehydrogenation of Propane and in Isopropanol Decomposition. Appl Catal A-General 125:129–144. doi: 10.1016/0926-860X(94)00274-6

54. Chen KD, Xie SB, Bell AT, Iglesia E (2000) Alkali effects on molybdenum oxide catalysts for the oxidative dehydrogenation of propane. J Catal 195:244–252. Doi: 10.1006/jcat.2000.3025

55. Martin-Aranda RM, Portela MF, Madeira LM, et al (1995) Effect of Alkali-Metal Promoters on Nickel Molybdate Catalysts and Its Relevance to The Selective Oxidation of Butane. Appl Catal A-General 127:201–217. Doi: 10.1016/0926-860X(95)00037-2

56. Abbas SA, Jung K-D (2016) Preparation of mesoporous microspheres of NiO with high surface area and analysis on their pseudocapacitive behavior. Electrochim Acta 193:145–153. doi: 10.1016/j.electacta.2016.02.054

ABSTRACT

In this work, the properties and catalytic behavior of nickel oxide in the oxidative dehydrogenation reaction of ethane (ODH) in ethene were investigated, subdivided into three subsections: influence of precursors; effect of calcination temperature and effect of promoter concentration. All samples were characterized by XRD, FTIR, UV-Vis, SEM and TEM. The catalytic activity and selectivity in the ODH reaction were quantified online by gas chromatography. In the first one, the influence of the precursor was studied, synthesizing six different precursors by different methods: α-hydroxide, β-hydroxide, mixed hydroxide, nitro-hydroxide, basic carbonate and nickel oxalate. The oxides obtained showed cubic structure with different degrees of crystallinity, particle size, specific surface area and morphology. The oxides resulting from the precursors basic carbonate and mixed hydroxide had the largest surface areas of 197 and 155 m^2/g and particles in the order of 5 to 6 nm. The best catalytic performance was attributed to the alpha hydroxide precursor with 22% conversion and 66% selectivity for ethylene; in this case, the oxide presented a sponge-like and porous structure with an average diameter of 56 Å. Assays performed at 270 °C showed a variation in intrinsic activity between 4.24×10^{-10} and 15.90×10^{-10} $\mu mol.m^{-2}.s^{-1}$, and activation energy of 66-81 kJ/mol. The oxide obtained from α-$Ni(OH)_2$ showed higher yield and lower band gap energy 2.69 eV when compared to the others, denoting the possibility of its influence on the catalytic performance of the ethane ODH reaction. In the second subsection, the β-$Ni(OH)_2$ synthesized by precipitation-oxidation was selected to study the effect of heat treatment on the properties of oxides. As in section one, the products obtained presented cubic structure of pure NiO with different degrees of crystallinity, crystallite size and specific surface area. The increase in the calcination temperature caused an increase in the mean crystallite size from 28 Å at 250 °C to 104 Å at 400 °C, while the shape of the particles did not show significant differences; the pore diameter increased from 35 Å to 69 Å and the specific surface area decreased from 245 m^2/g to 82 m^2/g. The test performed at 240 °C showed a decrease in conversion, from 8.75% to 4.25%; the most crystalline samples showed the highest intrinsic activity with selectivity to ethylene close to 60%. No influence of gap energy on catalytic properties was observed. In subsection three, the effect of doping by Na^+ cations on the properties and catalytic behavior of solid NiO solutions was investigated. A 2^3 factorial design with a triplicate central point was used to evaluate the effect of three independent parameters (reaction time, washing temperature and calcination temperature) and their influence on the catalytic activity of each sample. In addition, the study of physicochemical properties such as composition, particle size, crystallite size and optical gap energy band and how they influence the activity and selectivity of samples. The results indicated a homogeneous crystal with the same structure as the initial nickel oxide, indicating the formation of a solid solution. At high concentrations of Na^+, they resulted in decreased catalytic activity, but with better selectivity to ethylene. Low concentrations of Na^+ showed an increase in catalytic activity, resulting in a conversion of 22%, but with moderate selectivity to ethylene between 66-68%. The calcination temperature was the most influential factor on the NiO crystal size. The best ethylene yields and the greatest stability under reaction conditions were obtained in catalysts with low Na^+ concentrations. The introduction of sodium was the most beneficial for ethane ODH, increasing the ethene selectivity for values greater than 90% with a relatively small drop in reactivity toward ethane as the sodium concentration increases.

Keywords: Oxidative Dehydrogenation. Ethane. Nickel Oxide Catalyst. Oxygen Non-stoichiometry. Vacancy Defects. Solid Solution. Dopant Ions. Factorial Design.

LISTA DE FIGURAS

LISTA DE TABELAS

LISTA DE ABREVIATURAS E SIGLAS

AH	Alpha Hydroxide
BC	Basic Carbonate
BET	Brunauer-Emmett-Teller: surface area analysis
BH	Beta Hydroxide
CHM	Composite-Hydroxide-Mediated
Ea	Activation Energy
Eg	Optical band gap energy
FCC	Fluid Catalytic Cracking
FEG	Field Emission Gun (high-resolution scanning electron microscopy)
FID	Flame Ionization Detector
FTIR	Fourier Transformed Infrared
h -	Planck constant
HN	Hydroxyl Nitrate
hν	Photon Energy
ICSD	Inorganic Crystal Structure Database
LMCT	Ligand-to-Metal Charge Transfer
MH	Mixed Hydroxide
ODH	Oxidative DeHydrogenation
ODHE	Oxidative DeHydrogenation of Ethane
OX	OXalate
R	Gas constant
R∞	Diffuse reflectance
S_{BET}	BET Surface area
SEM	Scanning Electron Microscopy
SG	Sol-Gel
TEM	Transmission Electron Microscopy
UV-Vis	UltraViolet–Visible Spectrophotometry
ν	Intrinsic rate
XRD	X-Ray Diffractometry
W/F	Weight-to-Flow rate

λ	Wavelength

SUMÁRIO

1 INTRODUCTION

The present and future estimates of ethylene consumption have been showing constant growth over the years [1]. The reasons are the importance of olefins in the modern world, the extensive use, and the remarkable growth demand in some expanding sectors linked to the petrochemical industry in which it is used as a valuable intermediary and important basic material for plastics, fibers, and other chemicals [2]. Today all the world production of ethylene is performed via traditional processes of steam cracking and fluid catalytic cracking (FCC) of naphtha with very intensive energy consumption and operate at temperatures above 1000 K [2–4]. The search for energy efficiency combined with the low price of natural gas (ethane) is driving the development of alternative technologies for the production of ethylene. One of the promising routes is oxide hydrogenation of ethane with an important issue from academic research [5]. ODH is catalyzed by simple and mixed inorganic oxides, especially vanadium [6–8], molybdenum [9, 10] and nickel oxides [11–13]. One of the best low-temperature and relatively high-efficiency metal mixtures is Mo–V–Nb oxides [10]. This mixed metal oxide combination with the addition of other elements has gained preference for ODHE reaction; however the complicated preparation limits its practical application [14]. The main advantages of this technology are lower energy requirement, high activity, and high selectivity for olefins at low temperatures. Historically the ethane ODH technology is not used for large-scale ethylene production, due to the low activity and selectivity of the catalysts used in the reaction, not being economically attractive [15, 16]. One of the greatest difficulties is the development of suitable ODH catalysts, which minimize secondary oxidation reactions and the total oxidation of ethane [7]. The olefin product tends to be more reactive than ethane, undergoing secondary oxidation and generating undesired by-products such as CO and CO_2 (Figure 1) [2, 17]

Figure 1: Ethane ODH reaction with parallel-consecutive reactions

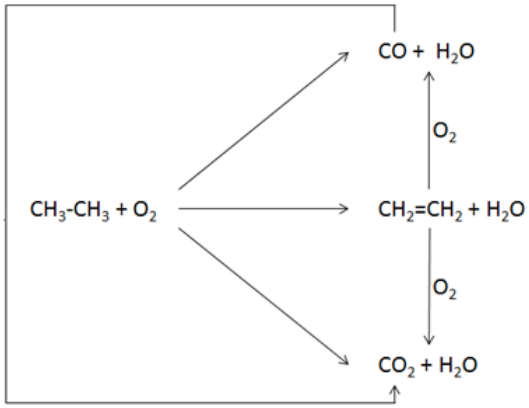

In this context, several materials with redox properties have been developed and applied in order to assist the mechanism of reactions at the molecular level, and reactions in the gas phase [15]. Among those materials, nickel oxide stands out for being a cation-deficient semiconductor as well as being an excellent oxidation catalyst able to activate C-H bond at low temperature [18, 19]. Many studies on catalytic performance and kinetic behavior suggested that ethane ODH on nickel oxide follows the Mars-van Krevelen redox mechanism [20]. The oxidation-reduction cycle begins with the activation of a hydrogen atom from an ethane molecule by a surface O^{2-} species, generating the ethyl radical that is desorbed from the catalyst in the form of ethylene. The remaining hydroxyl species are eliminated as water, leaving a reduced metallic site available to subsequent oxidation by molecular dioxygen from the gas phase [13, 15]. Activation of the C-H bond is the rate-limiting step of the overall reaction due to the high stability of the C-H bond (419.5 kJ/mol) [19, 21]

The pure stoichiometric nickel oxide is a green insulator compound with a rock salt structure. However, nickel oxide prepared by thermal decomposition of nickel salt in air is a crystalline, non-stoichiometric p-type semiconductor. The non-stoichiometry is accompanied by a color change from green to black or gray-black due to the existence of cation vacancies (Ni^{2+}) in the NiO crystal lattice [22]. The presence of cation vacancies (Ni^{2+}) causes the oxidation of two Ni^{2+} ions around the vacancy to Ni^{3+} ions to keep neutrality. The effects of non-stoichiometry must be associated with the existence of excess oxygen in NiO_x, where $x \approx 1$ [23, 24]. Ni^{3+} ions or holes (h^+) have been considered to improve ethane conversion due to the generation of electrophilic O− species ($h^+ + O^{2-} \rightarrow O^-$) [25, 26]. The defected nickel oxide interacts with an oxygen molecule to dissociate it, both nickel vacancies and oxygen play an important role in the catalytic and selectivity of ODH of ethane reaction.

1.1 INFLUENCE OF PRECURSORS

The catalytic properties (activity and selectivity) are also determined by the size, shape, morphology and surface microtopography of the catalyst particles as well as the local structure of the active site and [27, 28]. The key factor in obtaining nickel oxides with different properties has been the use of different precursors and preparation methods [29]. Nickel oxides have been prepared with different degrees of crystallinity, particle sizes [30–32], morphologies [33, 34], and specific surface areas [35] using different precursors and preparation methods. For example, Ying Wu, et al. [36] reported NiO nanoparticles synthesized by different methods such as solid-state milling, precipitation, sol-gel, and reverse

micro-emulsion showing various diameters, shapes, and size distributions. Variations were also observed in particles size and surface area that influence the adsorptive property, which has an intimate connection with their catalytic behavior. Another work developed by Abbas, et al. [37] investigated the conventional sol-gel (SG) method and composite-hydroxide-mediated (CHM) approach to prepare NiO nanoparticles and study their average crystallite size, optical and photocatalytic property. The largest optical band gap value was found for CHM as compared to SG nanoparticles due to smaller average crystallite size, 34 and 68 nm respectively. The best photocatalytic performance was observed for CHM nanoparticles due to their large surface area and higher concentration of oxygen vacancies.

The size, morphology, or exposed facets of some materials are among the factors to which their catalytic performance is often empirically and ambiguously attributed. To compare these effects different preparation methods from several precursors are proposed and discussed in this work.

1.2 EFFECT OF CALCINATION TEMPERATURE

The NiO surface reactions, as well as catalytic and chemisorptive properties, depend strongly on the preparation methods and surface defects created during the heat pretreatment of precursor. [38, 39]. The literature abounds with reported ways to prepare nickel oxide; the choice of the appropriate method to synthesize the precursor depends on the particular chemical or physical desired properties and the production scale. Among these methods, coprecipitation-calcination carried out at a moderately temperature is a simple, potentially scalable method, with advantages of large-scale production, flexible process, less time consumption, and low-cost production [36]. In the case of β-$Ni(OH)_2$, the oxide NiO probably comes from partial dehydration of nickel hydroxide. It has been claimed that dehydration promotes structural and surface defects leading to the formation of Ni^{3+} ion [40]. Cation defects (Ni^{2+} vacancy) at the surface lead to the formation of Ni^{3+} ions, associated with the existence of extra oxygen in the non-stoichiometric p-type oxide $Ni_{1-x}O$ [25, 26, 41]. But O^{2-} vacancies can also be formed. Both O and Ni vacancies tend to play important roles in the activity and selectivity of the catalyst in the oxidative dehydrogenation of ethane [42, 43]. The participation of Ni-O pairs adjacent to Ni vacancies on NiO(100) and NiO(110) surfaces has been examined on a theoretical point of view [26]. The role of the oxygen excess has also been investigated experimentally [44]. An understanding of the chemistry of those surface

processes relies on defining, in some detail, the electronic configurations of metal and oxygen species in the surface region [45].

The thermal dehydration of $Ni(OH)_2$ has some influence on the physicochemical properties of NiO such as crystallite size, surface area, pore size and volume, band gap energy, among others. Abbas and Jung [37] observed a decrease of surface area and pore volume of the mesoporous microspherical NiO samples with increasing calcination temperature of mesoporous α-$Ni(OH)_2$. Surface areas of NiO samples prepared at 250, 300, 350, 400, and 500 ºC were 295, 197, 133, 92 and 10.5 m^2/g, respectively. Similar behaviors of surface area and pore volume were observed by Lin, et al. [46] during the thermal decomposition of $Ni(OH)_2$ synthesized by the sol-gel method. These authors also observed an increasing of the average crystallite size with increase of the calcination temperature. Other researchers [47] found increasing of the average crystallite size of the NiO films with annealing temperature was accompanied with a decrease in the optical band-gap. Another work [48] showed that the gap energy as well as the crystallite size of NiO increase with $Ni(OH)_2$ calcination temperature.

Recently, Getsoian et al. [49] proposed that the apparent activation energy for propene oxidation to acrolein over mixed metal oxides with the scheelite structure correlates with the band-gap of the catalyst, a result which was also supported by theoretical calculations. They noted that the model proposed to explain the correlation could also apply to any oxidation reaction in which activation of the substrate involves LMCT-like excited states of the catalyst, whatever its crystalline structure. In this study, we analyzed the influence of calcination temperature on the morphology, on the band-gap energy and on the catalytic performance of nickel oxide in the ODH reaction of ethane into ethylene. The materials were obtained from β-$Ni(OH)_2$ synthesized by precipitation-oxidation followed by heat-treatment in air at different temperatures.

1.3 EFFECT OF PROMOTER CONCENTRATION

The chemical imperfections (defects) include both vacancies and foreign elements (impurities). The incorporation of promoters into ODH catalysts has been explored to synthesize other chemicals, besides alkenes, directly from alkanes. Incorporation of impurities by doping the lattice with a secondary metal cation to form a solid solution has been shown to improve its performance as a catalytic or electrochemical material [24, 50]. Depending on the

application nickel oxide lattice can be doped by monovalent Li^{+}, Na^{+}, Ag^{+}, divalent Mg^{2+}, Ca^{2+}, Zn^{2+} trivalent In^{3+}, Ga^{3+}, Cr^{3+} or high valence states Sn^{4+} Ti^{4+}, Ta^{5+}, Nb^{5}+, W^{5+} cations [43, 51–60] The effects of doping results in the decrease or in the increase in Ni^{3+} cation concentration in nickel oxide. The addition of monovalent cations into the NiO lattice usually leads to an increase in Ni^{3+} content, thus increasing the activity [53, 58]. Contrary to univalent doping which produces holes (Ni^{3+} ions), a trivalent ion replacing Ni^{2+} will be electrically compensated by the formation of adjacent singly or doubly ionized nickel vacancies, or else by excess electrons. Just like the trivalent the high valence states into the NiO lattice generally leads to a decrease in Ni^{3+} amount, which can alter the reaction performance of the obtained catalysts [11, 43, 57]. The promotion of nickel with several metals has a great effect on the ability of the catalysts to both activate the ethane feed and selectively convert it to ethene. Among the metal ions applied in NiO doping, niobium ion is the most studied for improving the ethylene selectivity of ethane oxidative dehydrogenation reaction, due to that Nb^{5+} cations fill into the Ni^{2+} vacancies instead of replacing the Ni^{2+} cations in the NiO lattice [11]. For example, study reported by Heracleous et al. about Ni–Nb solid solutions showed excellent catalytic behavior, exhibiting high activity and selectivity (~90% ethene selectivity) and yield of 46% at low reaction temperature for the ethane oxidative dehydrogenation reaction. The incorporation of Nb in the NiO lattice, reduced the materials non-stoichiometry and consequently the electrophilic oxygen species (O^{-}) concentration, responsible for the total oxidation of ethane [41]. Another work also developed by Heracleous and Lemonidou [53] reported a study about the effect of different metals (Li, Mg, Al, Ga, Ti, Ta and Nb). The results showed that the catalytic performance for the ODHE were related to the nature of the dopant in Ni-based mixed oxides. The higher valence state of Nb was prone to bind oxygen species, resulting in higher ethylene selectivity. They inferred that the amount of unselective electrophilic oxygen species depending on the nature of the dopant could increase or reduce the catalytic activity.

The NiO properties doped with monovalent ions, particularly lithium (Li^{+} ions), have been studied quite extensively. However, only a few investigators have reported the effect of sodium dopant ions on the properties of NiO. This may be related to the fact that the ionic radius of Li^{+} is very close to that of Ni^{2+}, so that lithium ion can be easily doped into nickel oxide. Doped nickel oxide tends to show similar lattice cell parameters compared with pure, undoped nickel oxide [61]. According to mass balance and electrical neutrality, the doped nickel oxide will produce hole (Ni^{3+} ions) adjacent to Li^{+} [62]. It has been established that the

semiconducting and catalytic properties of nickel oxide depend upon its defect structure and surface composition. According to the rule of charge neutrality, Na^{+} introduction in the oxide can also lead to the formation of Ni^{3+} ions and decrease of Ni^{2+} content in the lattice [63]. In addition, the presence of alkali metal cations such as sodium, besides disturbing the balance of defects, also alters the acidity of the solid, since it is considered as a hard acid of the scale developed by Pearson, 1963 [64].

Alkali metal additives to oxide systems may modify both acid-base properties and metal-oxygen bond energy with beneficial effect on the selectivity to olefins in ODH of light alkanes. Grabowski et al. [65] reported this effect for the ODH reaction of propane by VOx/TiO_2 and $MoOx/TiO_2$ catalysts with Li, K, and Rb. The same behavior was observed Chen et al. [66] using $MoOx/ZrO_2$ catalysts with Li, K, and Cs for the ODH reaction of propane. Martin-Aranda et al [67] also observed the same behavior in the ODH reaction of butane on nickel molybdate with Li, Na, K, and Cs. The acid-base and redox properties and the catalytic data of this system could be useful for description of the mechanism of action of oxide catalysts in the ODH reactions

Despite of decades of intense investigation, nickel oxide (NiO) continues to attract interest due to the possibility of controlling its properties. In this work, we investigate the Na^{+} ions doping effect in the catalytic proprieties of NiO obtained from heat treatment of nickel alpha hydroxide. We analyzed the influence of calcination temperature on the morphology, on the band-gap energy and on the catalytic performance of nickel oxide in the ODH reaction of ethane into ethylene. The non-stoichiometric oxide samples were studied by X-Ray Diffraction (XRD), Fourier-Transform Infrared (FTIR), Ultraviolet-Visible Spectrophotometry (UV-vis), and Scanning Electron Microscopy (SEM).

1.4 OBJECTIVES

The sections describe the general objective and the specific objectives of this work.

1.4.1 General objectives

The objective of this work was to study the preparations, the physical and chemical properties and the catalytic activity of nickel oxide in the oxidative dehydrogenation reaction of ethane, aiming to verify the influence of the precursor, the treatment temperature and additives on the catalytic performance.

1.4.2 Specific objectives

- Obtain nickel oxides from different precursors using different synthesis methods.
- Characterize the oxides as well as their respective precursors through physical and chemical techniques
- Evaluate the influence of precursors and method of preparation, treatment temperature on the property as well as the catalytic performance of the oxides.
- Evaluate the influence of the additive on both the property and the catalytic performance of the oxides obtained by doping
- Evaluate the influence of the parameters suggested in the experimental design on the properties and catalytic performance of the oxides.

2 METHODOLOGY

2.1 CATALYSTS PREPARATION

2.1.1 Influence of precursors

Six NiO samples have been prepared from different precursors: alpha (AH) and beta (BH) hydroxide, mixed hydroxide (MH), hydroxyl nitrate (HN), basic carbonate (BC) and oxalate (OX).

Synthesis route to alpha phase nickel hydroxide, α-$Ni(OH)_2$. The inverse coprecipitation method adapted from Yagi (2013) [68] was use in the synthesis process at room temperature. The aqueous nickel nitrate solution 100 mL (0.0080 M) was added dropwise into the ammonia carbonate precipitant solution 200 mL, (0.350 M) under vigorous stirring. The final product was stirred for 30 minutes at room temperature and then filtered. The filtered precipitate (precursor) was washed with distilled water, dried for 24 h at 60 °C and calcined in air at 350 °C for two hours, at the heating rate of 5 °C/min.

Synthesis route to beta phase nickel hydroxide, β-$Ni(OH)_2$. The synthesis was conducted by the precipitation-oxidation method in aqueous solution, adapted from Tang (2008) [55]. The precipitation process was carried out at 50 °C with 15 mL of 0.6 M $Ni(NO_3)_2 \cdot 6H_2O$ solution added dropwise to 30 ml of 3.2M NaOH solution; 30 mL of H_2O_2 (30 wt%) was then introduced slowly under constant stirring. The precipitate was then filtered, washed with distilled water and dried in an oven at 80 °C for 24 h. The dried $Ni(OH)_2$ was submitted to heat treatment at 350 °C for 2 h, at the heating rate of 5 °C/min under air flow.

Synthesis route to mixed nickel hydroxide, $Ni(OH)_2$. An aqueous nickel nitrate solution of 100 mL (0.0080 M) was prepared by dissolving $Ni(NO_3)_2 6H_2O$ in distilled water. A sodium carbonate solution of 200 mL, (0.350 M Na_2CO_3) for pH control and precipitation was also prepared. These solutions were heated to 80 °C with vigorous stirring (500 rpm). The nitrate nickel solution was added dropwise to the sodium carbonate precipitation solution. The resulting suspension was stirred at 70–80 °C for 30 min and then filtered. The filtered precipitates (precursors) were washed with distilled water (300 mL) at 80°C, dried for 24 h at 80 °C and calcined in air at 350 °C for 2 h, at the heating rate of 5 °C/min.

Synthesis route to nickel hydroxy nitrate, $Ni_2(OH)_3NO_3$. First, 0.349 g $Ni(NO_3)_2 \cdot 6H_2O$ was dissolved in absolute ethanol to form a 40 mL solution with the

concentration of 0.03 M. Then, the solution was transferred to a Teflon-lined cell, and solvothermal synthesis was conducted in a microwave oven at 160 °C for 3 h [69](KONG *et al.*, 2012). After cooling naturally to room temperature, the as-obtained solid was separated by filtration and thoroughly washed with absolute ethanol and deionized water. The precursor was calcined at 350 °C for two hours, at the heating rate of 5 °C/min under air flow.

Synthesis route to basic nickel carbonate, $Ni_{12}(CO_3)_8(OH)_8$. In this case, 45 mmol $Ni(NO_3)_2 \cdot 6H_2O$ and 0.6 mol $CO(NH_2)_2$ were dissolved in 75 mL H_2O under stirring at room temperature, then pH was adjusted to 3.75 using HCl (37%) following a method adapted from Lee's [70] (LEE; LIN, 2019). The solution was transferred into a Teflon-lined cell, placed in a microwave oven and heated to 160 °C for 4 h. After the reaction the sample was washed using distilled water and ethanol, and dried at 60 °C. The precursor was calcined at 350 °C for 2 h at the heating rate of 5 °C/min.

Synthesis route to nickel oxalate $Ni(C_2O_4) \cdot nH_2O$. This sample was prepared by adding a solution of oxalic acid (6.0 g in 100 mL of water) to a boiling solution of $NiSO_4 \cdot 5H_2O$ (8.0 g in 300 mL of water), under stirring. The precipitated fine pale green microcrystalline powder was washed several times with hot water and finally dried in air [71](FIGGIS; MARTIN, 1966). The precursor was calcined at 350 °C for 2 h at the heating rate of 5 °C/min.

2.1.2 Effect of calcination temperature

To study the effect of the calcining temperature on the properties and catalytic performance of nickel oxide, the beta nickel hydroxide was selected because it has a lower temperature for conversion into oxide. The synthesis of nickel oxide catalysts was conducted by precipitation-oxidation in an aqueous media following a methodology adapted from Tang et al. [55]. The precipitation process was carried out at 50 °C with 15 mL of 0.6 M $Ni(NO_3)_2 \cdot 6H_2O$ solution added dropwise to 30 ml of 3.2M NaOH solution; 30 mL of H_2O_2 (30 wt%) was then introduced under constant stirring. The precipitate was then filtered, washed with distilled water, and dried in an oven at 80 °C for 24 h. The dried $Ni(OH)_2$ was submitted to heat treatment under airflow at different temperatures (250 - 400 ◦C) for two hours, at the heating rate of 5 °C/min .

2.1.3 Effect of promoter concentration

In this section a factorial 2^3 experimental design was implemented to prepare several samples of NiO from alpha nickel hydroxide:

The precursor **(α-Ni(OH)$_2$)** was prepared by inverse coprecipitation of a solution containing 10 g of sodium carbonate and 4 g of sodium bicarbonate in 100 mL of H_2O. This solution was maintained at a temperature of about 50°C and kept under stirring while a concentrated solution of nickel sulfate was added. A clear, green solution quite free from suspended basic carbonate was obtained following a methodology adapted from Zheng and Adam [72]. The final stages of the oxide preparation process were conducted through a two-level factorial experimental design with three central points to assess the influence of three factors: reaction time, washing temperature and heat treatment temperature as shown in Table 1. The experimental runs were carried out in random order, and the results were analyzed with the software STATISTICA. The materials obtained were evaluated in terms of particle size, crystallite, morphology, composition, and how these properties influence the catalytic performance (activity, selectivity and stability) in the oxidative dehydrogenation reaction of ethane.

Table 1: Levels of the 2^3 factorial design with added center point for the process.

Independent variables	Levels		
	- 1	0	1
Washing temperature (°C)	0	25	50
Reaction time (h)	1	5	10
Calcination temperature (°C)	300	350	400

2.2 PHYSICAL AND CHEMICAL CHARACTERIZATION

X-Ray diffraction (XRD) patterns of the different samples were obtained using a diffractometer (Ultima IV Rigaku), with Cu-Kα radiation source (λ = 1.5418 Å) operated at 40 kV and current of 20 mA with K-beta filter. The data were recorded by continuous scanning over a range of 2θ angles from 5° to 80° with steps of 0.05°. The crystal structure of each phase of interest was identified using Inorganic Crystal Structure Database (ICSD) files. The analysis of the most intense peaks from XRD data applying the Scherrer equation

allowed the calculation of the average crystallite size of the samples [73]. The data were also used to quantify the percentage of phases present in some samples and to determine the lattice constant, using the Rietveld refinement method in Maud program [74].

Fourier-transform infrared spectroscopy (FTIR) was carried out in the wave number range from 400 to 4000 cm^{-1} using Nicolet-6700 spectrometer. The samples were dispersed in KBr and pressed into waffles at 7 tons/cm^2. The spectra helped to identify the precursor phase as well as the characterization of adsorbed substances and resulting residues in the calcined samples.

Diffuse reflectance UV-visible spectra of the samples have been collected in the range 200-900 nm in UV-vis-Nir under ambient condition by Shimadzu-2600 spectrophotometer equipped with an integration sphere. The spectra of NiO were recorded in powder form, after dilution in $BaSO_2$ (5 wt % of NiO) also used as a reference. The bandgap energy behavior of NiO's or optical band gap energy (Eg) was calculated using the Kubelka-Munk Equation [75]:

$$F(R_\infty) = (1- R_\infty)^2/(2* R_\infty) \quad (1)$$

where R_∞ is the diffuse reflectance of the sample. Using Tauc & Menth function [76] and Equation 2.1, the following equation 2.2 is obtained:

$$[F(R_\infty)h\upsilon]^2 = A(h\upsilon-Eg)^{1/2} \quad (2)$$

where A is a proportionality constant, and hυ is photon energy.

The **nitrogen adsorption/desorption isotherms** at 77 K were acquired using an Autosorb-1 analyzer, after degassing for about 12 h at 300 ° C. The specific surface area of the samples was analyzed using the BET multipoint method, and the pore volumes were estimated from data P / P0 =0.99.

X-ray Fluorescence (XRF) spectra were acquired on a Bruker device, model S2 RANGER. The chemical composition of the samples was measured without any previous treatment.

Scanning electron microscopy (SEM) was performed using a JEOL JSM-6701F Scanning Electron Microscope (FEG), operated at 10KeV to study the microstructure and morphology of the NiO powder.

Transmission electron microscopy (TEM) was performed using a JEM-1011 microscope, working at 100KeV.

2.3 CATALYTIC PERFORMANCE

The catalytic oxidation dehydrogenation of ethane was performed in a conventional fixed-bed reactor operating at atmospheric pressure. The experiment was conducted in the temperature range 150°C - 310°C with a catalyst amount of 0.5 g and fed with a mixture of 3% C_2H_6/ 1% O_2 in N_2 (mol/mol) with catalyst weight-to-flowrate W/F =1 g.s.mL^{-1} for flowrates of 0.5 mL.s^{-1}. Ethane and the reaction products were analyzed on-line by gas chromatography (Agilent GC-7820) with FID detector. Ethane and COx were separated by a Porapak Q capillary column before passing through a methanizer. The intrinsic activity of the catalysts was calculated as $(F_i \times X_i)/(100 \times S_{BET} \times m_{cat} \times V_m)$, where F_i [m³/s] is the flow of ethane at the inlet of the reactor, X_i [%] is the total conversion, m_{cat} [g] is the weight of sample, S_{BET} [m^2/g] is the specific surface area of the catalyst and V_m = 0.0224 [m^3/mol] is the volume occupied by one mole of gas.

2.4 STATISTICAL ANALYSIS

The results were tested with analysis of variance (ANOVA) with 5% level of significance ($p < 0.05$) for rejection of the null hypothesis, using the Statistica software, version 7.0. The principal and interaction effects resulted of the factorial design were calculated and the variance analysis was used to evaluate the effect of independent variables on the response using the mathematical model expressed by equation 3:

$$Y = \beta_0 + \sum_{j=1}^{k} \beta_j x_j + \sum\sum_{i<j} \beta_{ij} x_i x_j + \sum_{j=1}^{k} \beta_{jj} x_j^2 + \varepsilon \quad (3)$$

where Y is the expected response, X_i are the independent variables (washing temperature, reaction time and calcination temperature) and the other terms refer to interaction effects. The term βo is an interception coefficient (regression coefficient at central point), β_i are the linear coefficients, β_{ij} are the interaction coefficients and β_{jj} represent pure second-order or quadratic effects.

3 . RESULTS AND DISCUSSION

3.1INFLUENCE OF PRECURSORS

3.1.1 Physical and chemical properties

XRD patterns and FTIR spectra were employed for investigating and identifying the precursor phases as well as the respective oxides formed after heat treatment.

The sample of **α-Ni(OH)$_2$ (AH)** precursor is amorphous and therefore, the diffraction peaks in 2θ = 10.0; 33.2 and 60.0 were assigned to (003), (012) and (110) crystal planes corresponding to the hexagonal structure (alpha nickel hydroxide), Figure 2 A. The intensity of the peak at 10.0 is stronger than the other, indicating that (003) plane may be preferred growth direction. This structure presents lamellar structure interspersed by water molecules and anionic carbonate similar to structures known as hydrotalcites. The identification of these interlayer species was complemented with the analysis of FTIR spectra (Figure 2 B), which presented a broad band at 3436 cm^{-1} and another less intense band in 1624 cm^{-1}, assigned to interlayer water molecule [77]. The 1466 cm^{-1} and 1405 cm^{-1} bands are mainly due to the vibration of CO_3^{2-} ionic species, related to asymmetric stretching. The sample also exhibited bands at 1064, 847 and 689 cm^{-1} which correspond to the vibration modes of carbonate ions for out-of-plane and in-plane bending vibration respectively [77, 78]. This means that CO_3^{2-} ions are not free in the interlamellar space but interact with nickel ions of the brucite type layers as for unidentate complexes. The peak appearing at 407 cm^{-1} corresponds to ν(Ni–O) the bending vibrations in α-Ni(OH)$_2$ [78].

Figure 2: Characterization of α-Ni(OH)$_2$ (AH): (A) XRD pattern; and (B) FTIR spectrum.

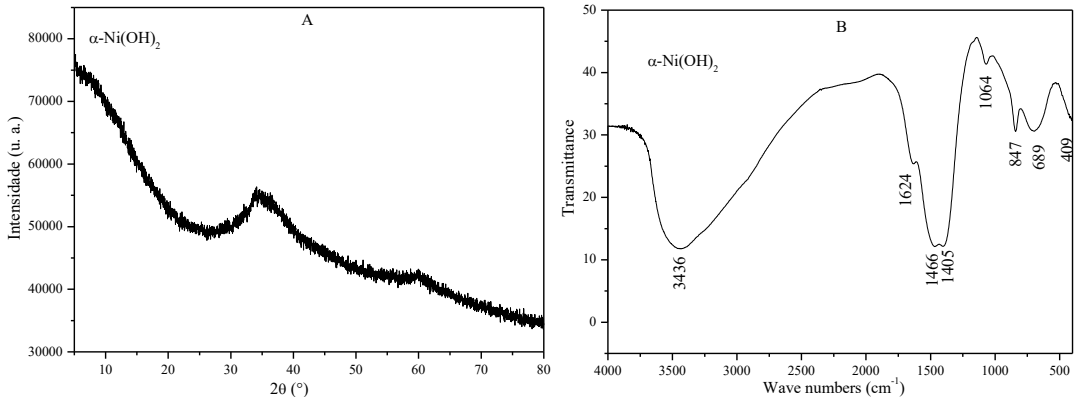

The XRD pattern of **β-Ni(OH)$_2$ (BH)** shows that (Figure 3 A) the as-prepared samples have high crystallinity, and all the characteristic peaks can be indexed to β-Ni(OH)$_2$ phase with the lattice parameters of a =3.08 Å and c = 4.62 Å (ICSD No. 169978), and no impurity is detected. This material belongs to the brucite Mg(OH)$_2$ structure type with Space Group: P-3m1 (164) [77]. Major diffraction peaks at 2θ = 19.2°, 33.2°, 38.4°, 51.9°, 59.3°, 62.8°, 70.1° and 72.8° can be attributed to (001), (100), (101), (102), (110), (111), (103) and (201) crystal planes, respectively. The unusual broadening of the (001) and (100) lines in XRD patterns of Ni(OH)$_2$ (Figure 3 A), may be attributed to stacking faults within the structure along the direction of the crystallographic c-axis [79, 80]. Additionally, FTIR spectrum data (Figure 3 B) presents a sharp band at ν = 3634 cm^{-1} assigned to O-H stretching mode of the hydroxide. The broad absorption band centered at 3440 cm^{-1} is attributed to O–H stretching vibrations, and the band at 1649 cm^{-1} is attributed to the bending mode (H–O–H) of adsorbed water [77]. The other two peaks, which appear at 518 cm^{-1} and 446 cm^{-1} are attributed to δ(O–H) and ν(Ni–O) vibrations in β-Ni(OH)$_2$, respectively. The peaks at about 1455 cm^{-1}, 1382 cm^{-1}, 1053 cm^{-1} and 640 cm^{-1} are attributed to carbonate groups, which originate from chemisorption of CO_2 from air [78, 81]. Thus, the IR spectrum confirms the β-phase structure of the sample.

Figure 3: Characterization of β-Ni(OH)$_2$ (BH): (A) XRD pattern; and (B) FTIR spectrum.

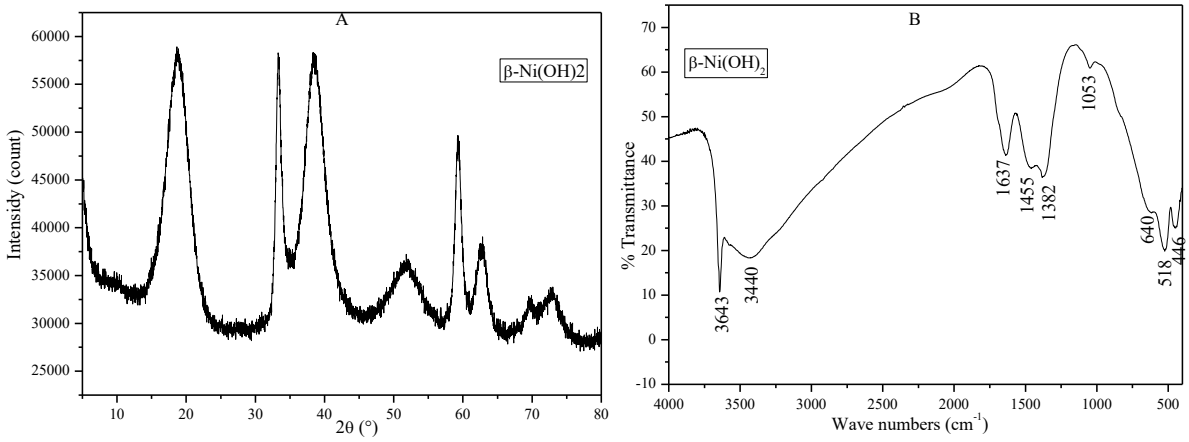

According to the XRD pattern of **Ni(OH)$_2$ (MH)** (Figure 4 A), the as-synthesized material has peaks at 2θ = 19.2°, 33.2°, 38.4°, 51.9°, 59.3°, 62.8°, 70.1° and 72.8° that can be indexed as (001), (100), (101), (102), (110), (111), (103) and (201) crystal planes of the hexagonal structure of β-Ni(OH)$_2$, respectively. The wide peaks and weak intensity imply an imperfect crystal structure of the precursor or small crystallites. The two additional diffraction peaks at 2θ = 10.2 and 16.3 in the low-angle region may be associated with presentation of

light elements such as interlamellar carbonate anions space interacting with nickel ions of the β-$Ni(OH)_2$ compound [77]. Additionally, the FTIR spectrum (Figure 4 B) presents a broad absorption band centered at 3438 cm^{-1} which is attributed to O–H stretching vibrations, and the band at 1649 cm^{-1} attributed to bending mode (H–O–H). The narrow band at 3634 cm^{-1} was attributed to free hydroxyl groups. The peaks at about 1480 cm^{-1}, 1383 cm^{-1}, 1053 cm^{-1} and 616 cm^{-1} are attributed to carbonate groups, which originate from chemisorption of CO_2 from air and interlamellar space interact with nickel ions of the brucite type. The other two peaks at 524 cm^{-1} and 447 cm^{-1} are attributed to δ(O–H) and ν(Ni–O) vibrations in β-$Ni(OH)_2$, respectively [77, 78].

Figure 4: Characterization of mixed nickel hydroxide, $Ni(OH)_2$ (MH): (A) XRD pattern; and (B) FTIR spectrum.

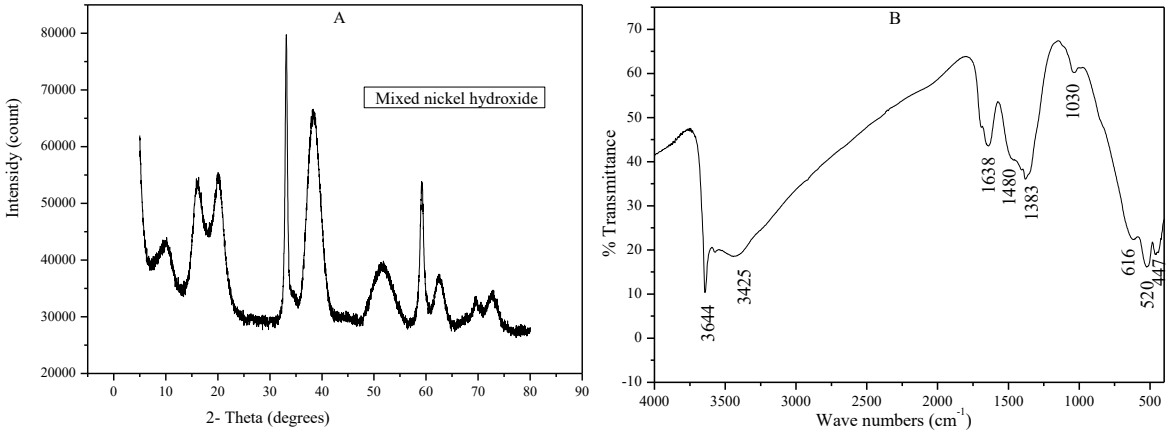

Figure 5 A presents the XRD pattern of nickel hydroxyl nitrate, **$Ni_2(OH)_3NO_3$ (HN)** with characteristic peaks at 2θ=12.2; 24.6 and 33.2 assigned to (001), (002) and (101) crystal planes. The intensity of the first peak (2θ=12.2) is stronger than the other, indicating that (003) plane may be preferred growth direction [82]. The FTIR spectrum (Figure 5 B) confirms the presence of hydroxide anions in the sample with a well-defined band at 3643 cm^{-1} (O-H stretch mode). The broad band at 3400 cm^{-1} and the very weak band at 1637 cm^{-1} are attributed to O–H stretching mode and bending mode (H–O–H) of chemisorbed water, respectively [82, 83]. The bands at 1503, 992 and 640 cm^{-1} are assigned to antisymmetric (ν_4), out-of-plane deformation (ν_2) and in-plane deformation (ν_3) of NO_3^-, stretching vibrations and the bands at 1382 and 1321 cm^{-1} are related to symmetric stretching (ν_1). The two other peaks at 482 cm^{-1} and 410 cm^{-1} are attributed to ν(Ni–O) vibrations in $Ni_2(OH)_3NO_3$ [83].

Figure 5: Characterization of nickel hydroxyl nitrate, $Ni_2(OH)_3NO_3$ (HN): (A) XRD pattern; and (B) FTIR spectrum

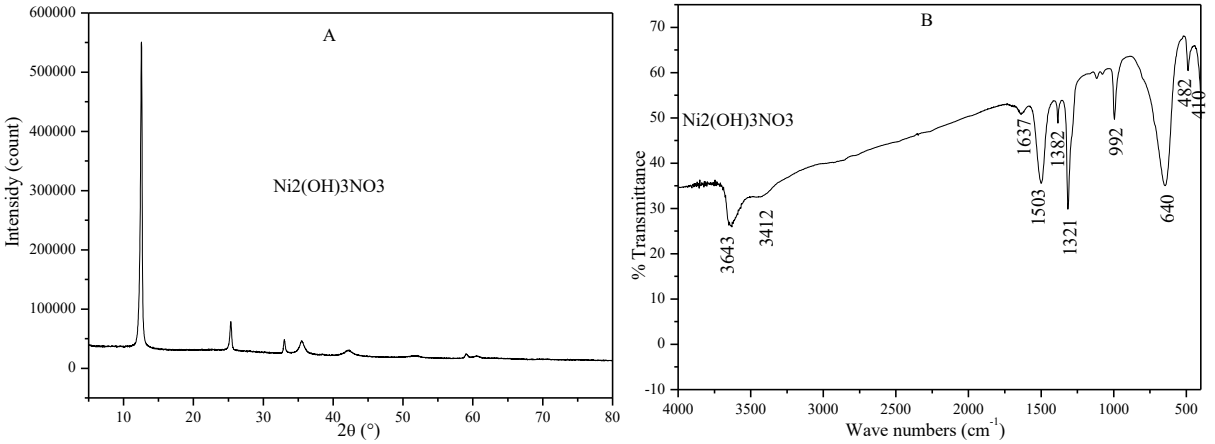

The XRD pattern of the basic carbonate **$Ni_{12}(CO_3)_8(OH)_8$ (BC)** (Figure 6 A) confirms the formation of the phase in agreement with the reference data (ICSD_196120) of the cubic structure with cell parameter a = 8.3815 Å and space group P -4 3 m. The FTIR spectrum (Figure 6 B) presents a weak broad at ν = 3660 cm^{-1} that can be assigned to the O–H stretching vibration of the hydroxyl group in $[Ni_{12}(CO_3)_8(OH)_8 \cdot (5–7)H_2O]$. The other two peaks at 920 and 615 cm^{-1} are attributed to γ(0-H) and δ(O–H) vibrations of lattice water in $[Ni_{12}(CO_3)_8(OH)_8 \cdot (5–7)H_2O]$, respectively. The broad band at ν = 3457 cm^{-1} is assigned to the O-H stretching vibrations of crystal water and the band at ν = 1546 cm^{-1} can be attributed to the O–H bending mode of adsorbed water. The bands at ν = 1448 cm^{-1} and 1400 cm^{-1} are related to asymmetric stretching (ν3) of CO_3^{2-}. The bands exhibited at 1060, 823 and 757 cm^{-1} are related to symmetric stretch (ν1) out-of-plane (ν2) and in-plane (ν4) bending vibration modes of carbonate ions, respectively [78]. The two other peaks that appear at 490 cm^{-1} and 410 cm^{-1} are attributed to ν(Ni–O) vibrations in sample. The absorption band at 1108 cm^{-1} is related to the stretching vibration ν(C-OH) [83, 84].

Figure 6: Characterization of basic nickel carbonate, $Ni_{12}(CO_3)_8(OH)_8$ (BC): (A) XRD pattern; and (B) FTIR spectrum.

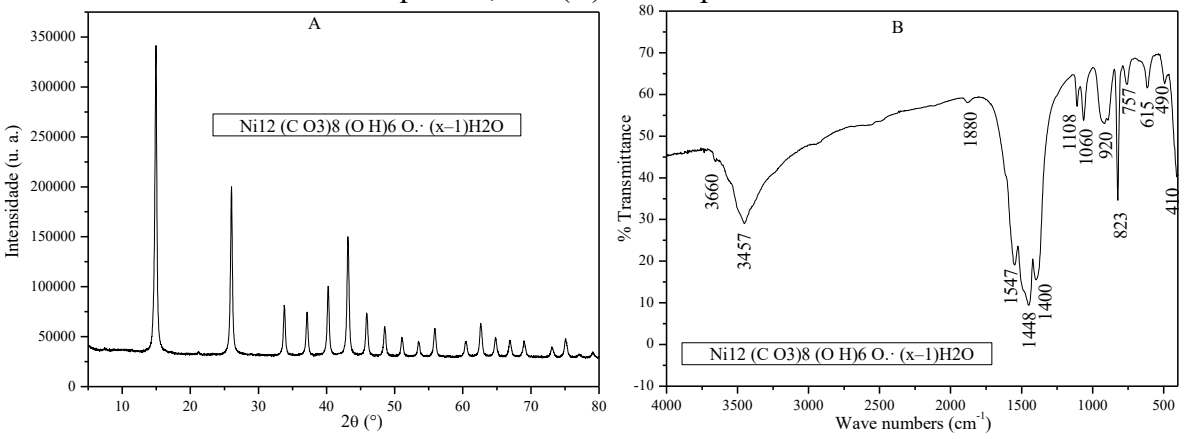

The XRD pattern of hydrated nickel oxalate, **$Ni(C_2O_4)$ nH_2O (OX)** (Figure 7 A) corresponds to the monoclinic phase of $NiC_2O_4 \cdot 2.5H_2O$ space group (C2/c) with high degree of crystallinity [85]. Hydrated nickel oxalate can be considered as a coordination polymer in which the oxalate ion $C_2O_4^{2-}$ acts as a double ligand, linking the four oxygen atoms to the metal ions. The cohesion between the oxalate and nickel ions planes is brought about by intermolecular hydrogen bonding of the H_2O ligands [86]. In the FTIR spectrum (Figure 7 B), the intense and wide band at 3376 cm^{-1} is due to the ν(OH) vibration of the coordinated water, as well as to the strong hydrogen bonds between the water molecules and the oxalate ligand. The band at ν = 1625 cm^{-1} can be attributed to the O–H bending mode of adsorbed water. The strong band that should appear at about 1580 cm^{-1} is related to asymmetric ν(C=O) stretching, overlapping the strong H_2O band at 1625 cm^{-1}. The absorption bands at 1356, 1309 and 828 cm^{-1} correspond to the symmetric stretching vibration of C-O bond and 750 cm^{-1} stretching vibration of δ(O-C=O) band in the oxalate bridge complex. The peak at 628 cm^{-1} is attributed to δ(O–H) vibrations of lattice water and confirms the presence of water in the coordinated form. The strong band at 487 cm^{-1} is assigned to the Ni-O stretching vibration mode [87, 88].

Figure 7: Characterization of hydrated nickel oxalate, $NiC_2O_4 \cdot 2.5H2O$ (OX): (A) XRD pattern; and (B) FTIR spectrum

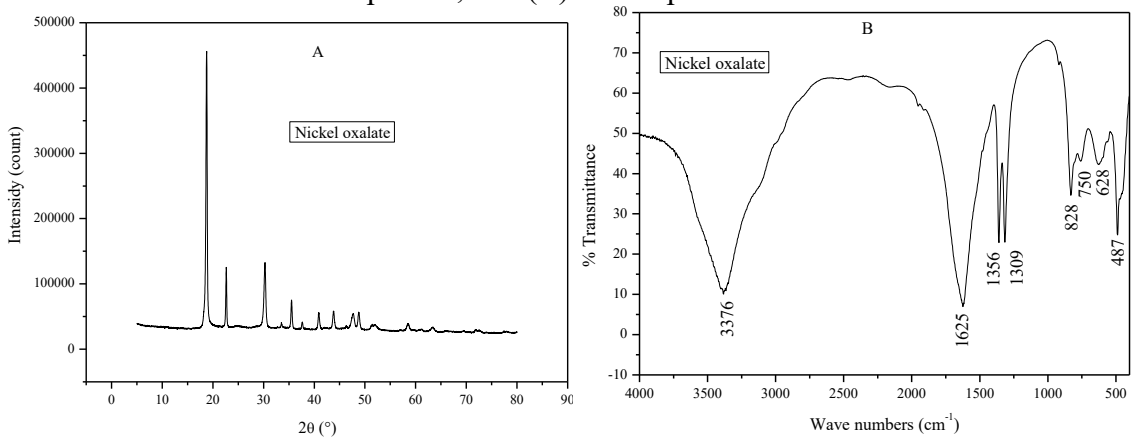

3.1.2 Oxide Characterization

Figure 8 depicts the XRD patterns obtained after heat treatment of the precursors at 350°C. All patterns show peaks corresponding to the (111), (200), (220), (311) and (222) crystallographic planes of cubic NiO (space group Fm-3m), indexed according to standard data ICSD-9866. In overall, the XRD analysis showed a single phase with small variations in the cell parameter, as shown in Table 2. The values of crystallite size, which were calculated from XRD patterns by using the Scherrer equation, are also shown in Table 2. Each nickel

oxide sample had a particular crystal size indicating the direct influence of the precursors on the properties of the materials obtained after heat treatment.

Figure 8: XRD patterns of non-stoichiometric NiO samples after heat treatment at 350°C for 2 h from different precursors.

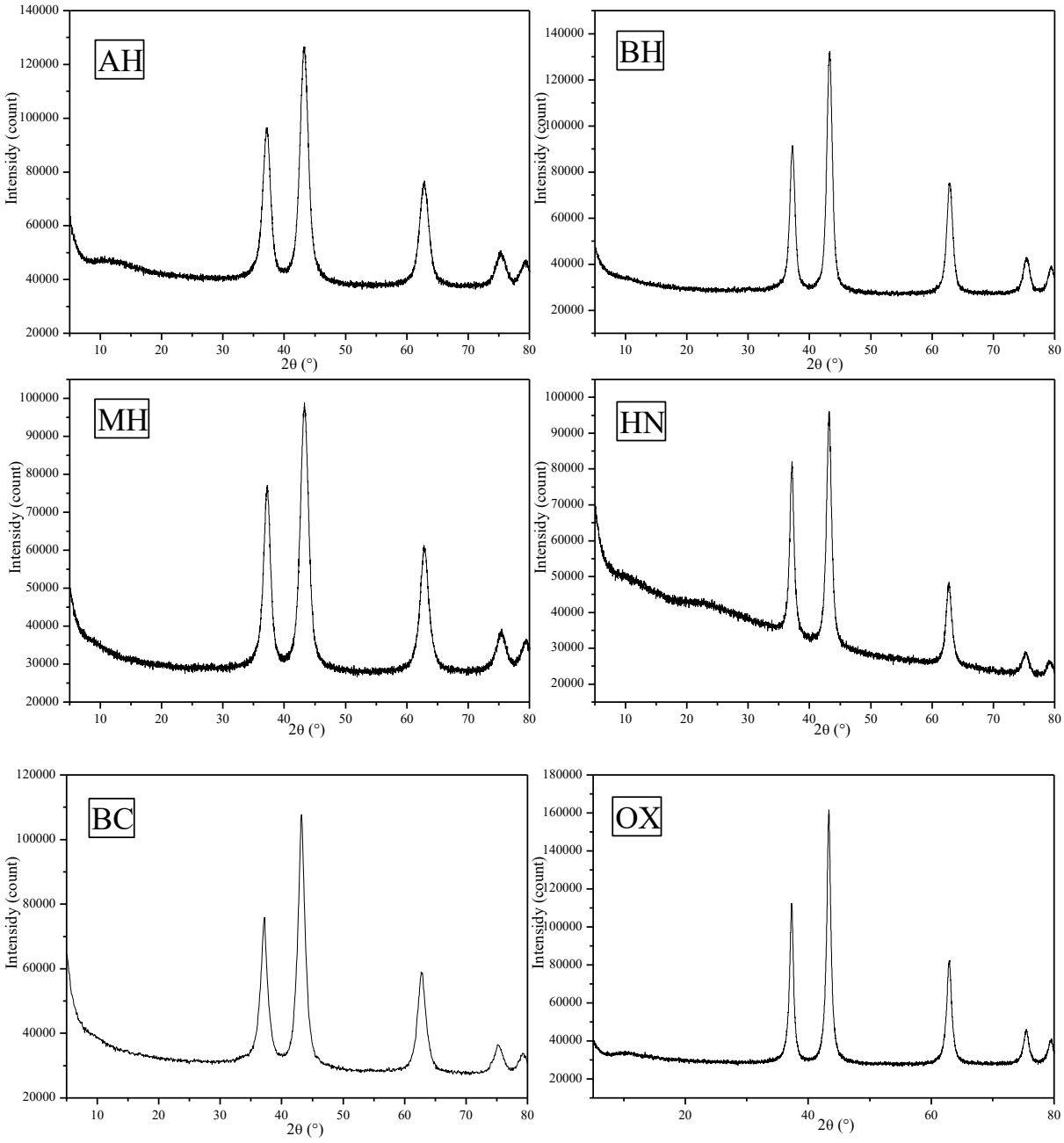

The main physical and chemical characteristics of nickel oxide are listed in Table 2. The oxides obtained after calcination showed BET surface area and average pore diameter different for each precursor, reaffirming its influence on the properties of the oxides

Table 2: The main physicochemical characteristics of nickel oxide obtained from heat treatment of different precursors. Alpha-nickel Hydroxide (AH); Beta-nickel Hydroxide

Samples	Sample data					
	Precursor	Cell p. (Å)	C. size (Å)	S. Area - BET (m^2/g)	Pore D. (Å)	Eg [eV]
AH	α-Ni(OH)2	4.186	62	127	56	2.69
BH	β-Ni(OH)2	4.182	70	131	57	3.43
MH	NiOOH/Ni(OH)2	4.181	61	155	_	3.03
HN	Ni2(OH)3NO3	4.190	107	105	75	3.47
BC	Ni12(CO3)8(OH)8	4.188	85	197	128	3.56
OX	Ni(C2O4) nH2O	4.177	168	74	109	3.38

(BH); Mixed nickel Hydroxide (MH); nickel Hydroxyl Nitrate (HN); Basic nickel Carbonate (BC); nickel Oxalate (OX). C. (Crystallite), p. (parameter), S. (Surface), D. (Diameter) and Eg (Optical band gap)

In the corresponding FTIR spectra (Figure 9), the strong band at 423 cm^{-1} corresponds to the stretching vibration mode of ν(Ni-O) [78]. The broad band about 3445 cm^{-1} and another less intense band at 1624 cm^{-1} are related to the stretching and bending vibrations of the water molecules absorbed by the sample. The band at 1450, 1383 and 1053 cm^{-1} are attributed to carbonate species due to the fact that the calcined powder tends to chemisorb acidic compounds such as CO_2 at basic sites [81, 89]. Analyzing the graphic Figure 2.9 it is observed that each oxide sample presented different intensity for band at 1383 and 433 cm^{-1} referring to carbonate species and stretching vibration mode of ν(Ni-O) respectively.

Figure 9: FTIR spectra of NiO samples after heat treatment at 350 °C for 2 h from different precursors.

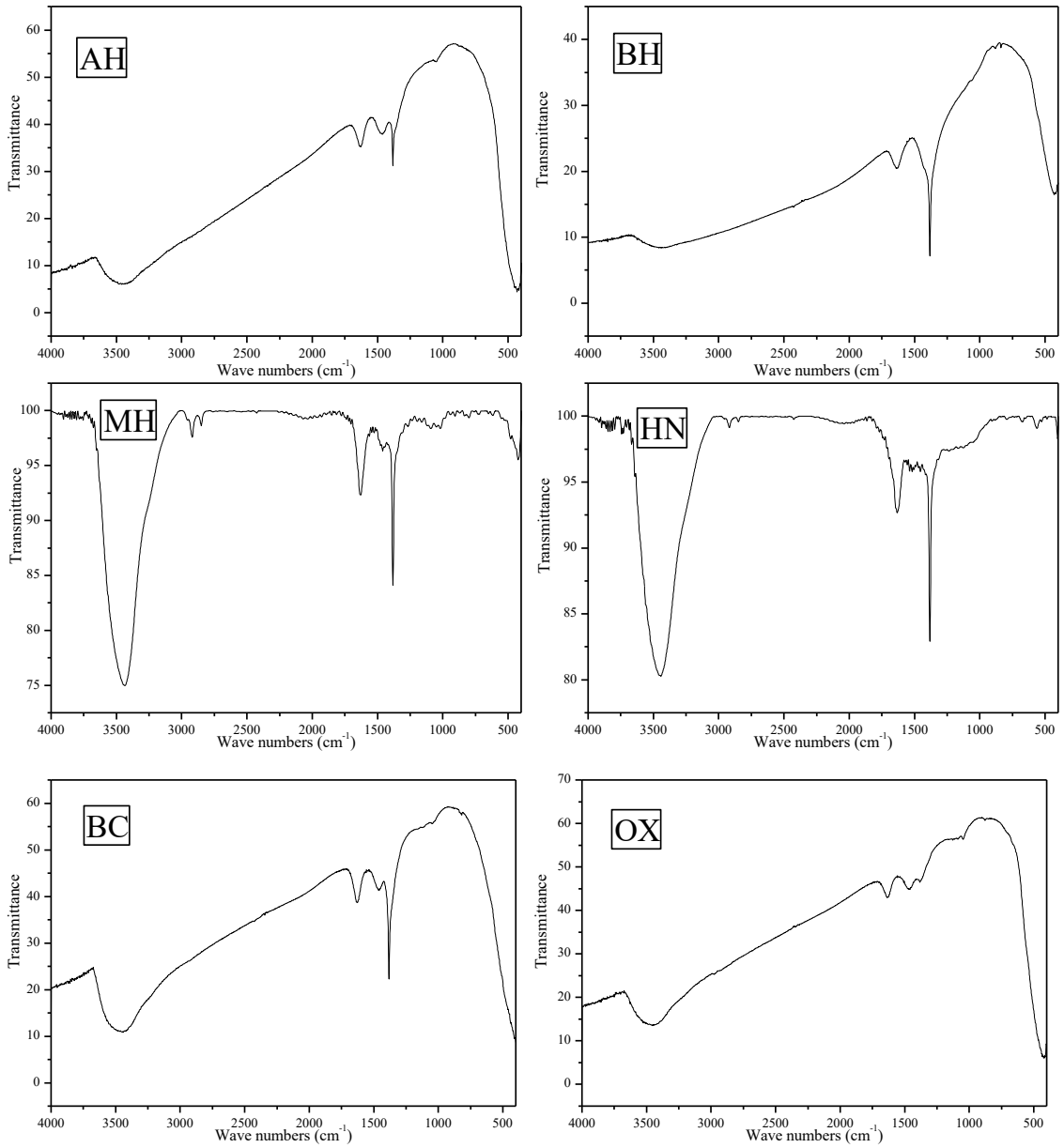

Figure 10 shows the diffuse reflectance UV-VIS spectra of the NiO powder obtained at different precursor. All the NiO samples revealed optical absorption bands at similar positions. Based on analyses of Tanabe-Sugano diagrams, we can infer that the strong band at 14,500 cm^{-1} and the weak band at 20,500 and 26,500 cm^{-1}, ascribed to the $^3A_{2g} \rightarrow {}^3T_{1g}(F)$, $^3A_{2g}(F) \rightarrow {}^3T_{2g}(F)$ and $^3A_{2g} \rightarrow {}^3T_{1g}(P)$ electronic transition in octahedral Ni(II) ion, are fingerprints for NiO. Three bands are expected for Ni(III): the weak absorption band at 30,500 cm^{-1} and the broad band at 35,500 cm^{-1} are supposed to be absorption lines corresponding to $^4T_{1g}(F) \rightarrow {}^4T_{1g}(P)$ and $^4T_{1g}(F) \rightarrow {}^4A_{2g}(F)$, respectively, and are assigned to the transitions in octahedral Ni(III) ($3d^7$) ion.-From the analysis of the graphs in Figure 10, it

can be observed that the samples of HN, BC and OX have a proportionally greater intensity for the peaks attributed to Ni (III) ions in relation to Ni (II). For the BH sample this proportion seems to be smaller, showing the concentration of Ni(III) ions also higher than Ni(II) and for the MH sample the intensity of the peaks presents a semilarity. Unlike other oxides, HA has well-defined peaks attributed to both Ni(III) ions and Ni(II) ions, with peaks related to Ni(III) ions slightly higher in a proportional manner.

Figure 10: UV-Vis reflectance spectra of NiO samples after heat treatment at 350°C for 2 h from different precursors.

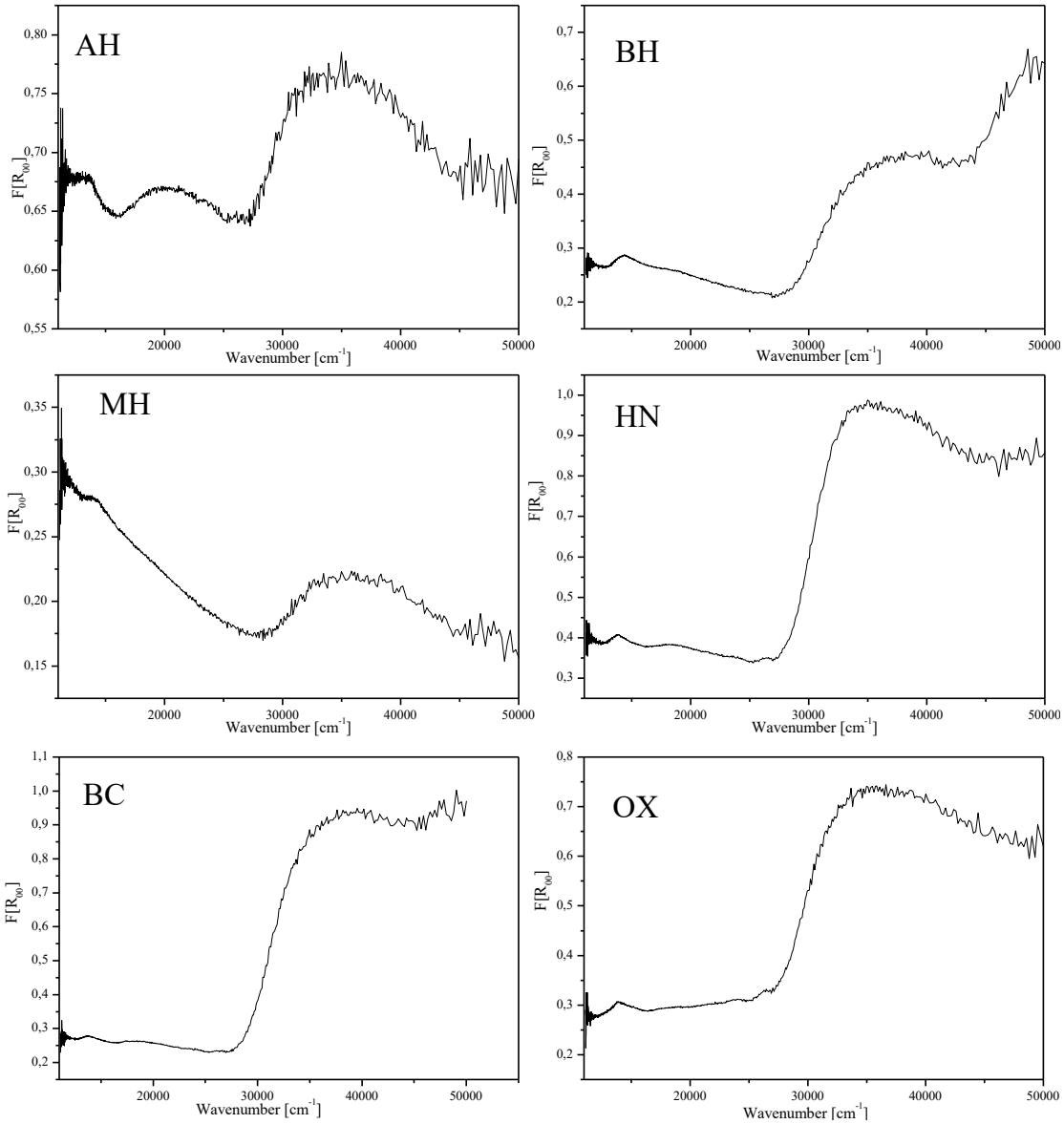

The optical band gap Eg has been estimated by extrapolating the linear fitted region at $[F(R_\infty)h\upsilon]^2 = 0$ in the plot of $[F(R_\infty)h\upsilon]^2$ versus hυ (Figure.11). The resulting band gaps (Eg) are shown in Table 2. The highest values of band gap energy were observed for the oxide from basic nickel carbonate precursor (3.56 eV), the lowest for alpha hydroxide (2.69 eV) and

mixed hydroxide (3.03). The OX, BH and HN samples showed values of (3.38 eV), (3.43 eV) and (3.47 eV) respectively demonstrating the strongly influenced of morphology of the oxide in bandgap energy.

Figure 11: Linearized spectrum allowing the determination optical band gap of NiO samples after heat treatment at 350°C for 2 h from different precursors.

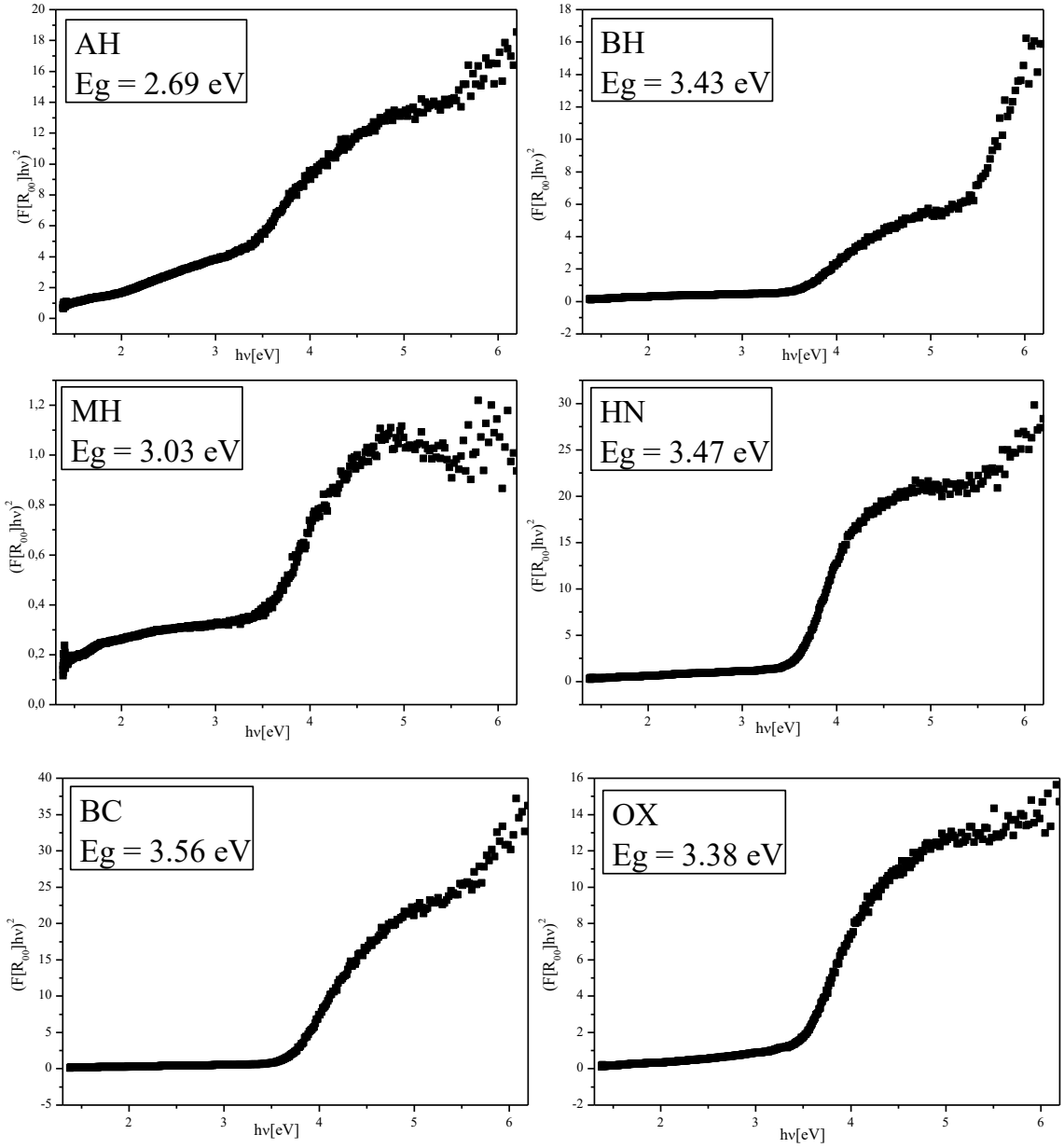

Figure 12 shows SEM images of nickel oxides originated from all precursors. The images for beta-nickel hydroxide precursor (BH) revealed heterogeneity of particle size, most with dimensions larger than 1 μm. In general, they are sponge-like structures with high porosity. The images for oxide obtained from nickel hydroxyl nitrate reveal a flower-like hierarchical structure in the form of nano-flakes with a diameter of around 1 μm. In the case of nickel oxalate (OX), irregular particles in the form of a parallelepiped with dimensions

close to 1 pm and laminar structures of high porosity are observed. The oxides obtained from alpha hydroxide (AH), mixed hydroxide (MH) and basic carbonate (BC) present clusters of particles in the form of plates. However, the degree of particle agglomeration varies according to the precursor resulting in a significant variation in the surface area measured by BET (Table 2). Apparently, there are no important differences in morphology between these three samples.

Figure 12: SEM image at different magnification of NiO samples after heat treatment at 350°C for 2 h from different precursors.

AH

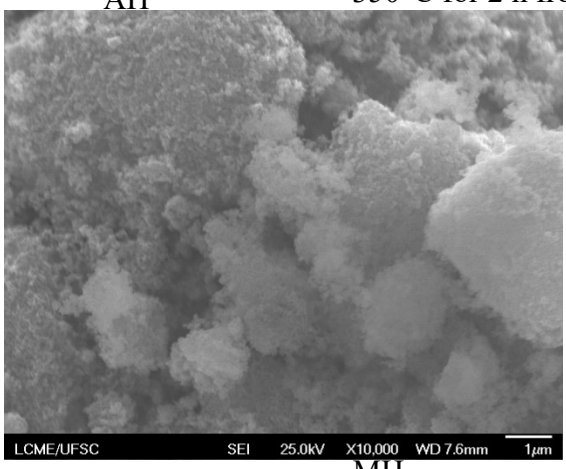

BH

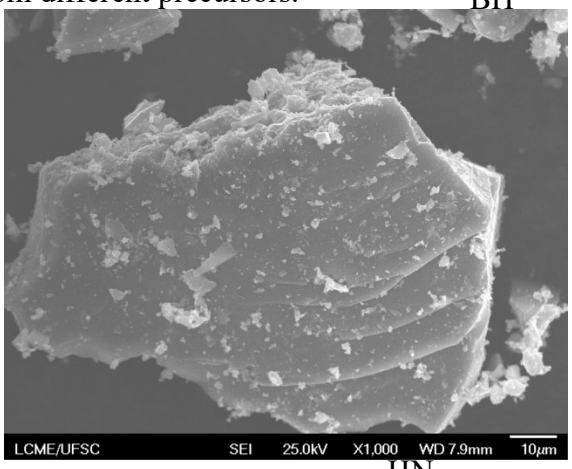

MH

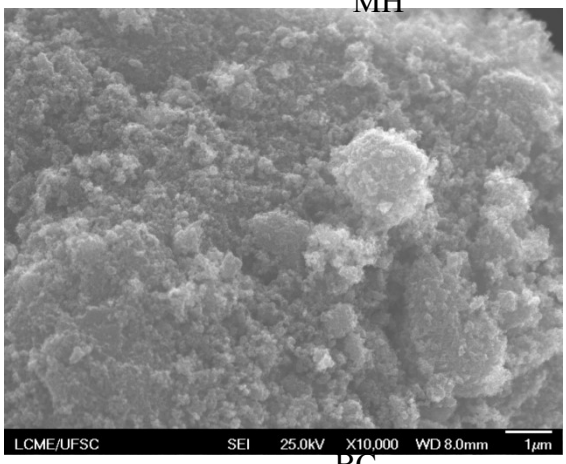

HN

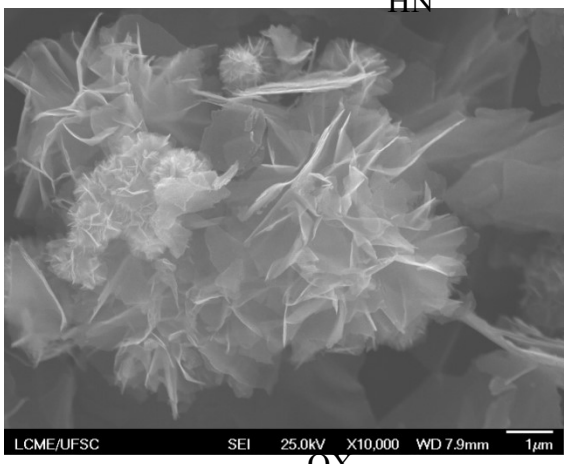

BC

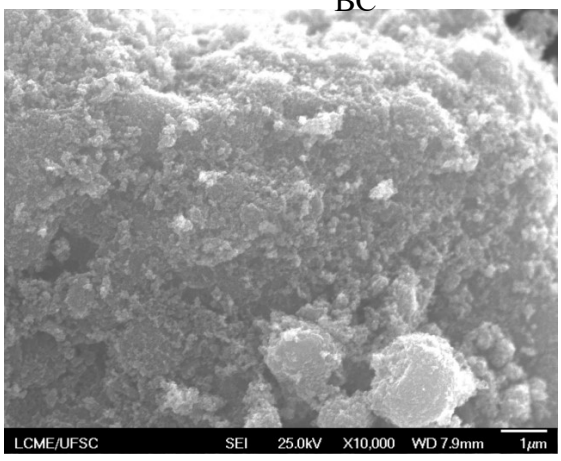

OX

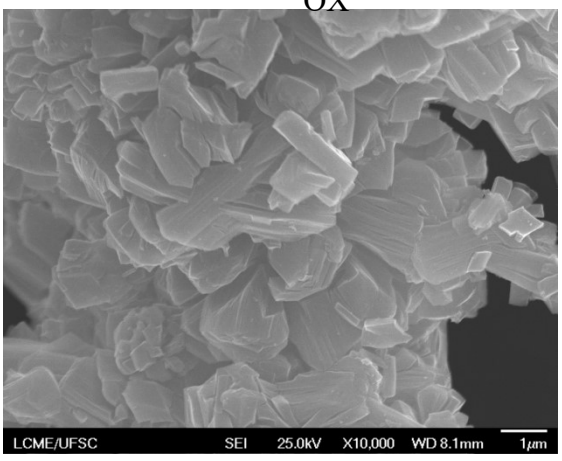

Bright field images (Figure 13) obtained by transmission electron microscopy performed on NiO samples indeed show essentially porous particles for AH and BH, and nanoparticles of average diameter of 6 nm for MH and 5 nm for BC. All the electron diffraction spots display the crystalline signature of NiO for the area of the analyzed samples.

Figure 13: TEM image at different magnification of NiO samples after heat treatment at 350°C for 2 h from different precursors

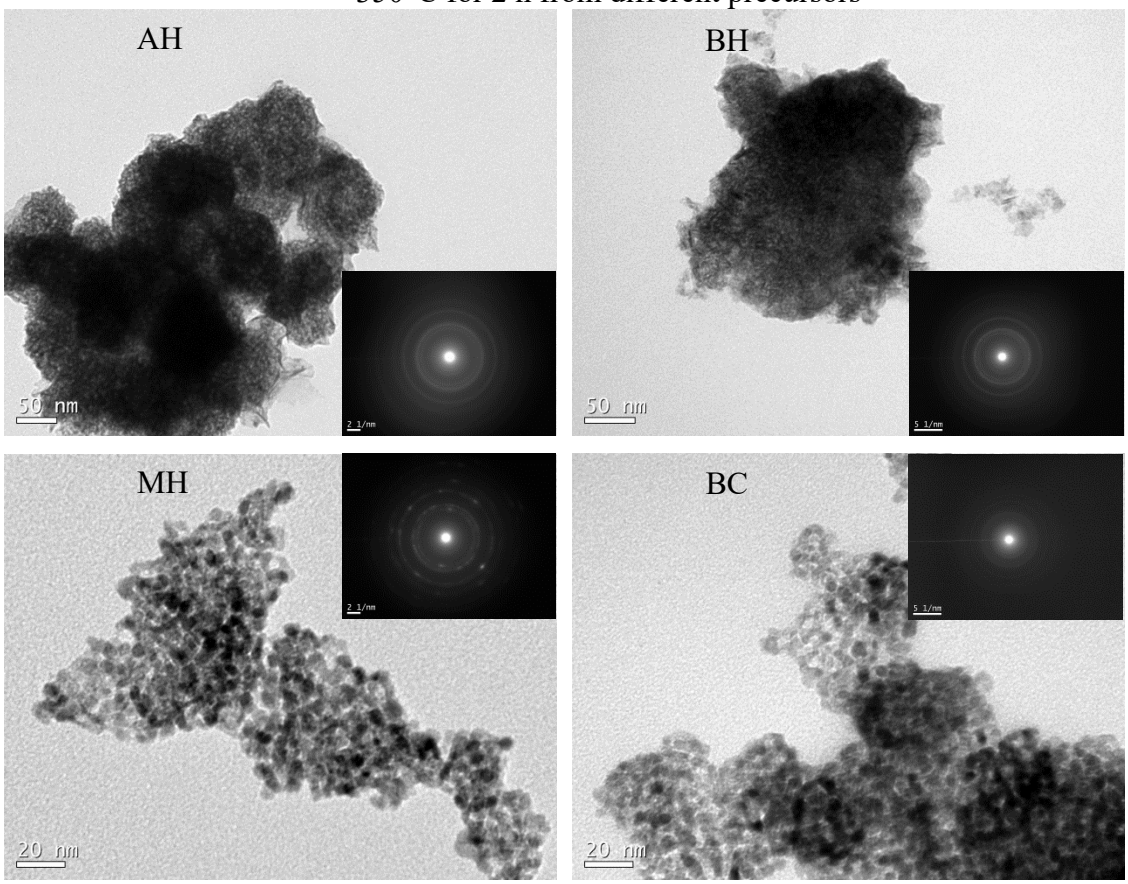

3.1.3 Catalytic performance

The NiO samples were tested in the ODH reaction; ethane conversion is plotted in Figure 2.14 as a function of temperature. Selectivity to ethene as a function of both, temperature and conversion, has also been plotted in Figure 14. All materials in this series show an increase in conversion with reaction temperature. The oxides obtained from carbonate or oxalate precursors showed better catalytic performance, especially those from alpha hydroxide. The oxides from mixed nickel hydroxide precursor showed high selectivity at low reaction temperatures, but reducing with increasing conversion rate. For conversions higher than 10% up to close to 20% the same materials present selectivity to 60% ethylene with few variations. The NiO-AH exhibited the highest conversion at 310°C with an

appreciable selectivity to ethene of 65%. Based on the information obtained from the characterization apparently, there is no clear influence of other oxide properties such as particle size and surface area on the activity of the catalyst and selectivity to ethene.

Figure 14: Catalytic performance of nickel oxides after heat treatment at 350°C for 2 h from different precursors.

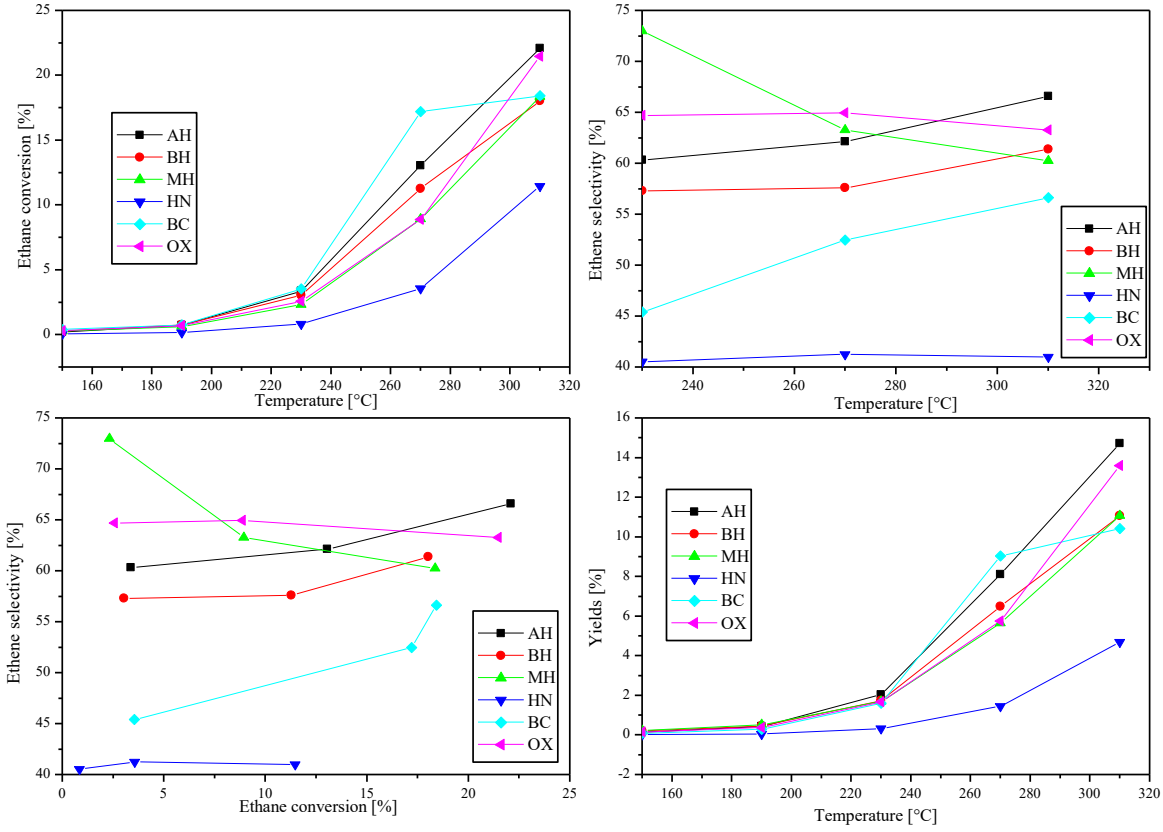

Table 3 gives the intrinsic activity at 270 °C in ethane ODH and the apparent activation energies for the total ethane reaction in the studied samples. The pertinent apparent activation energies was estimated from the Arrhenius equation in the temperature range from 180 to 270°C, as shown in Figure 15. For the reaction of ethane at 270°C the specific activity follows the sequence: HN < MH < BH < BC < AH < OX. However, the apparent activation energies are lower for oxalate, and higher for basic nickel carbonate precursor, following that order: OX < MH < BH < AH < HN < BC. High activity of basic nickel carbonate (BC) in spite of high activation energy values suggests the increase of the pre-exponential factor A (number of centers) in this case. Low activity of oxide (OX) catalyst may be due to both high value of activation energy and low value of number of the active centers.

Table 3 also lists the catalytic performance of all oxides in the oxidative dehydrogenation reaction of ethane at 270 °C. The sequence of the increasing selectivity for the samples series is: HN < BC< BH < AH < MN< OX. The conversion also follows a different order: HN < OX < MN < BH< AH < BC. The best yield of the process at a temperature of 270 °C was obtained for the sample oxide prepared from basic carbonate (Figure 14).

Table 3: Catalytic performance and kinetic properties of nickel oxides obtained by heat treatment at 350°C for 2 h from different precursors.

Sample	Catalytic performance at 270°C		Kinetic Properties	
	Conversion (%)	Selectivity (%)	Specific activity ($\mu mol.m^{-2}.s^{-1}$)	Activation Energy (kJ / mol)
AH	13.05	62.1	13.75×10^{-10}	75
BH	11.27	57.6	11.5×10^{-10}	70
MH	8.93	63.3	09.47×10^{-10}	69
HN	3.56	41.2	08.75×10^{-10}	80
BC	17.21	52.5	11.7×10^{-10}	81
OX	8.88	65.0	15.90×10^{-10}	66

Figure 15: Arrhenius plots of ln(activity) vs. 1/T for ethane ODH using nickel oxides catalysts after heat treatment at 350°C for 2 h from different precursors

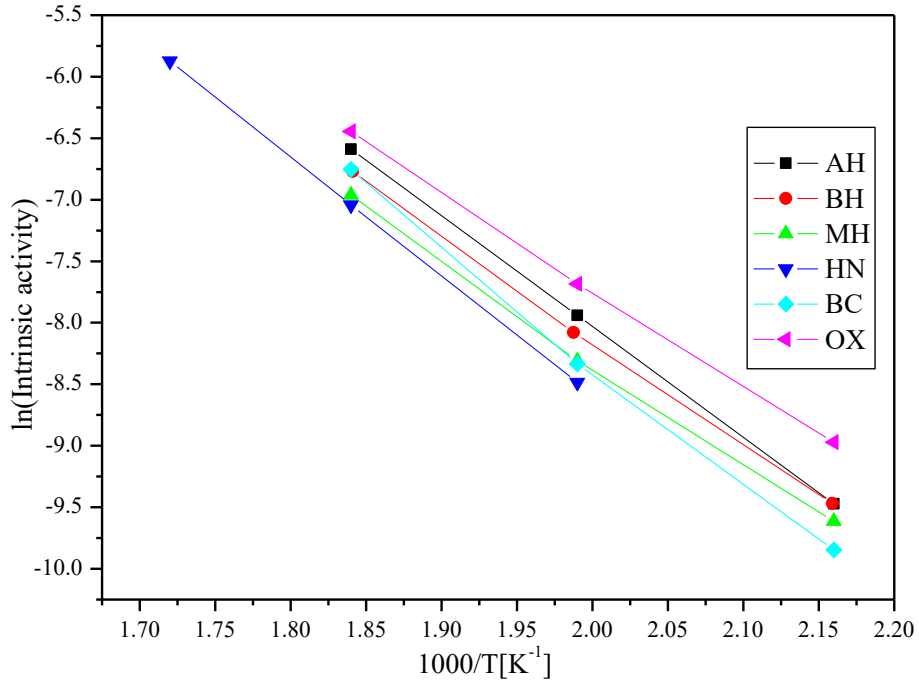

Figure 16 compares the catalytic performance of all oxides in the oxidative dehydrogenation reaction of ethane at 270 °C.

Figure 16: Catalytic performance for nickel oxides in ethane ODH reaction at 270 °C

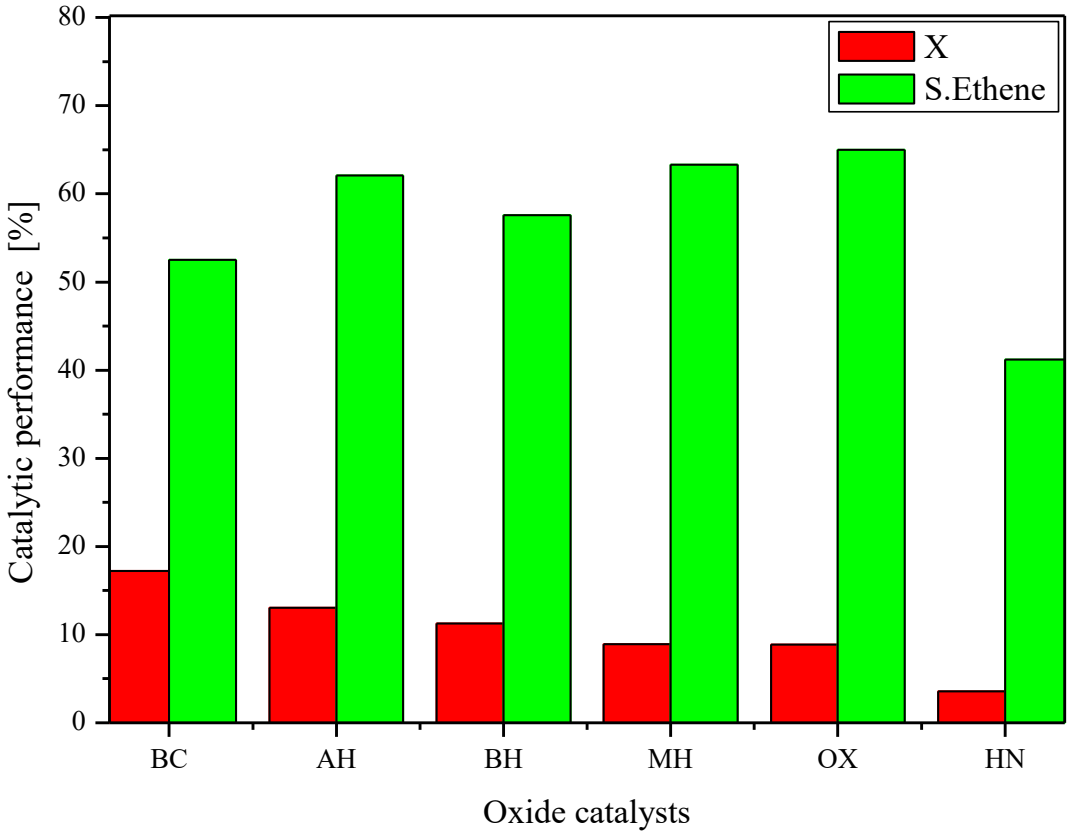

Table 4 presents a summary of physical characteristics of four nickel oxide prepared by different precursor and the catalytic performance together with its kinetic properties. The first three NiO's were obtained by different strategies by Zhu et al. [57] to study the effect of NiO preparation method in their catalytic performance. The protocols used were coprecipitation varying the precipitating solution (oxalic acid and NH_4OH) and sol–gel (citric acid). The ODH reaction was conducted at 300 °C, the gas mixture of 10% C_2H_6/10% O_2 in He was introduced through the catalytic bed with W/F = 0.6 g s/mL. The fourth NiO sample prepared by partial reduction with oxalic acid and thermally decomposed, was tested in the work developed by Savova et al. [43]. The reaction was conducted at 350 °C fed with a mixture of O_2:C_2H_6:N_2 = 9:9:82 and the weight to flow ratio (W/F) of 0.54 g.s/mL.

Table 4: Summary of the physical and chemical characteristics, and catalytic performance for nickel oxide in selected works

Catalyst	Sample	S_{BET}	P. Size	W/F	Catalytic performance				A. Energy	Reference
	NiO-T(°C)	(m2/g)	(nm)	g.s/mL	T. ºC	X (%)	S. Ethene (%)	ν, $mol.m^{-2}.s^{-1}$	(kJ /mol)	
$NiO\_{oxalic\ acid}$	400	65	8	0.60	300	15	55	1.76×10^{-8}	79	[57]
NiO_{NH4OH}	400	60	18	0.60	300	16	8	1.97×10^{-8}	100	[57]
NiO_{SG}	400	31	9.2	0.60	300	15	59	2.40×10^{-8}	80	[57]
$NiO\_{oxalic\ acid}$	450	12	28	0.54	350	12	31	5.10×10^{-8}	78	[43]

NiO-T (calcination temperature), S_{BET} (BET Surface Area), W/F (catalyst weight-to-flow rate), T. (Reaction Temperature), X (Ethane Conversion), **ν** (intrinsic rate),

The best performance in ethane ODH was obtained by NiO_{SG}, presenting a conversion of 15 %, ethene selectivity of 59% and intrinsic rate of 12.40 $\times10^{-8}$ $mol.m^{-2}.s^{-1}$ on test at 300 °C. For comparative purposes, the selected reference had a particular catalytic performance for each oxide as well as values reported in this work. Although there is no clear trend of the influence of the properties studied such as surface area, band gap energy or oxide defect content on performance, but the results show different values for each oxide. This denotes the difficulty in bringing the properties of materials to catalytic performance, but in the work, the influence of the precursor both on the properties of the oxides and on its catalytic performance is perceived.

Analyzing the data on the catalytic performance of the oxides for the test carried out at 270°C, it is verified that there is a significant difference between the conversions and the selectivity of the studied samples. In an attempt to relate the catalytic performance with the characteristics of the oxides, the differences that stand out between the samples are the morphology, which suggests a deeper study, mainly of the topography of the exposed surfaces. It can be highlighted that the sample of flower-shaped structure (HN) offered the worst performance in terms

of conversion (3.5%) and selectivity (40.0%) for the test performed at 270 °C, one of the Hypothesis may be related to the difficulty of flowing the reagent and the reaction product through the uneven surface. This structure can offer accumulation of the gaseous mixture in floccules, blocking the active sites and promoting preferential paths resulting in less conversion and re-oxidation of the accumulated product. In contrast, the material in the form of nanoparticles (BC) which allows a greater fluidity of the gas mixture, resulted in the highest conversion (17.2%) in the test carried out at 270 °C, perhaps the re-oxidation of the product harmed the selectivity (52%). The best selectivity's were observed in materials that showed porous structure, in sponge-like (HA) 62% and 65% plate-like and moderate conversion for the test performed at 270 °C. The morphology of the particles seems to be a very important factor in the catalytic performance, especially the microtopology of the exposed surface, which can directly influence the flow of the reaction mixture and the product of the reaction, suggesting future studies. Reaffirming the possibility of empirically assigning, the influence of particle morphology on the catalytic performance of materials.

3.1.4 Conclusions

In the present work, a clear influence of the precursor was observed on the catalytic behavior of NiO in ethane ODH reaction. This was demonstrated in the form of a different conversion for each catalyst. On the other hand, the selectivity to ethylene showed small variations, but always with values above 60%. The best catalytic performance was observed in the oxides form of nanoparticles, which allows a greater fluidity of the gas mixture and the worst for a sample that hinders the flow. This difference in the conversion of ethane was empirically attributed to the morphology of the particles, mainly the microtopography of the exposed surface, which presented a different structure for each oxide in the scanning electron microscopy images. The apparent activation energy was found to be independent of Ni(III) content and band-gap energy. In general, he results suggest that for the best catalytic performance, NiO catalysts should have large surface area and high crystallinity and that provides good fluidity of the mixture.

Effect of calcination temperature

3.1.5 Physical and chemical properties

The precursor as well as the catalyst oxides obtained after thermal treatment at different temperatures were identified through XRD patterns and FTIR spectra.

Figure 17 shows the XRD patterns that can be indexed to beta phase nickel hydroxides. All the characteristic peaks can be indexed to β-$Ni(OH)_2$ phase with the lattice parameters of a =3.08 Å and c = 4.62 Å (ICSD No. 169978), with no impurity detected. A brucite type structure $Mg(OH)_2$ was formed with space group P-3m1 (164) [77]. Major diffraction peaks (2θ = 19.2°, 33.2°, 38.4°, 51.9°, 59.3°, 62.8°, 70.1°, and 72.8°) can be attributed to the diffractions of (001), (100), (101), (102), (110), (111), (103) and (201) crystal planes, respectively. The unusual broadening of the (001) and (100) lines in XRD patterns of $Ni(OH)_2$ (Figure 17), may be attributed to stacking faults within the structure along the direction of the crystallographic c-axis [79, 80].

Additionally, the FTIR spectrum (Figure 18) presents the band at ν = 3634 cm^{-1}, which can be assigned to O-H stretching mode of the hydroxide. The broad absorption band centered at 3438 cm^{-1} is attributed to O–H stretching mode of water and the band at 1637 cm^{-1} is related to the bending mode of adsorbed water. The two other peaks that appear at 518 cm^{-1} and 446 cm^{-1} are attributed to δ(O–H) and ν(Ni–O) vibrations in β-$Ni(OH)_2$, respectively [77]. The peaks at about 1455 cm^{-1}, 1382 cm^{-1}, 1053 cm^{-1} and 640 cm^{-1} are attributed to carbonate groups, which originate from chemisorption of CO_2 from air. The bands at 1455 cm^{-1} and 1382 cm^{-1} are related to asymmetric stretching (υ_3 band), while that at 1053 cm^{-1} corresponds to symmetric stretching (υ_1 band). The band at 640 cm^{-1} is attributed to in-plane bending vibration (υ_4 band). A shoulder at about 880 cm^{-1} is assigned to out-of-plane bending mode (υ_2 band). Broken degeneracy of the υ_3 band indicates symmetry lowering of the adsorbed ion. Thus, the IR spectrum confirms the β-phase structure and basicity of the sample.

Figure 17: XRD pattern of the synthesized sample of β-$Ni(OH)_2$.

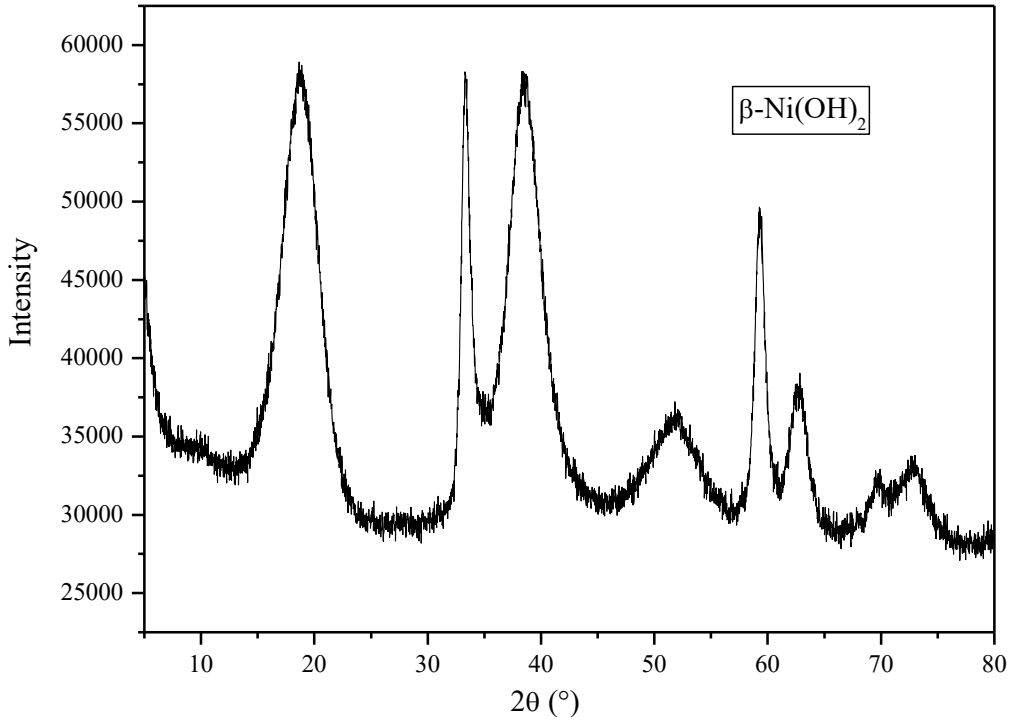

Figure 18: FTIR spectrum of the synthesized sample of β-$Ni(OH)_2$

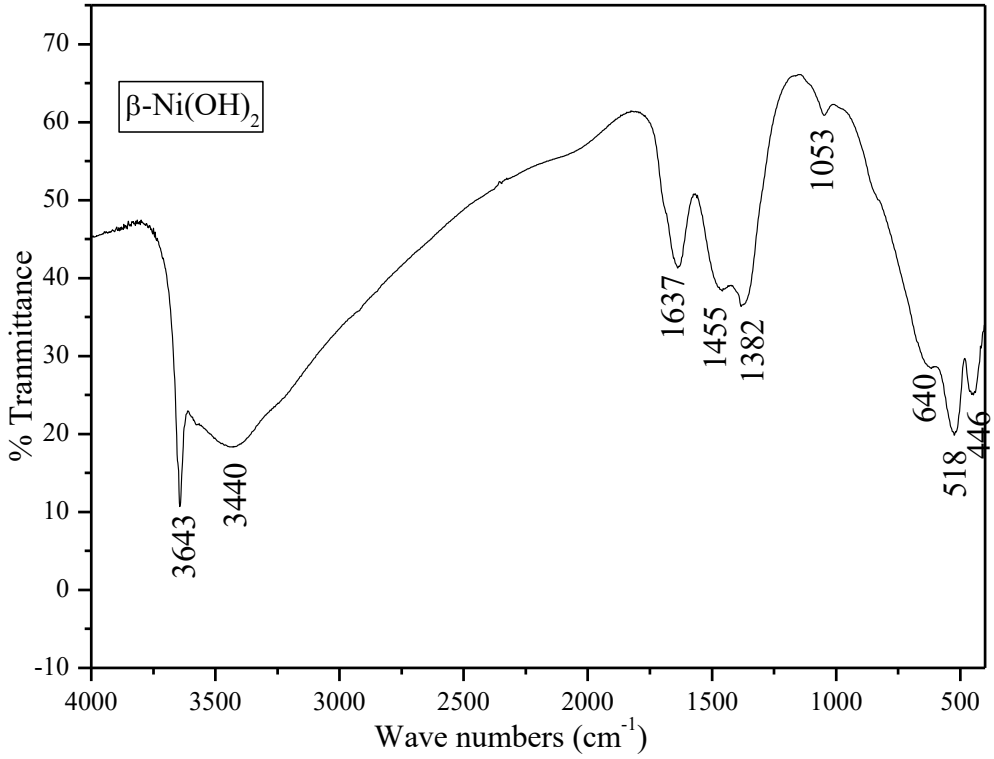

Figure 19 depicts the XRD patterns obtained after heat treatment of beta nickel hydroxide at different temperatures (250 to 400 °C). The observed peaks in all recorded XRD patterns correspond to the (111), (200), (220), (311) and (222) crystallographic planes, which

can be ascribed to the cubic crystal structure of NiO (space group Fm-3m) in agreement with standard data (ICSD-9866). Overall, the XRD analysis showed a single phase with small variations in the cell parameter, as presented in Table 5. The values of crystallite size, which were calculated by the Scherrer equation, are also shown in Table 1. The NiO crystal size increased with the calcination temperature of precursors.

Figure 19: XRD standard of non-stoichiometric NiO samples after heat treatment of β-$Ni(OH)_2$ in the temperature range of 250 to 400 °C.

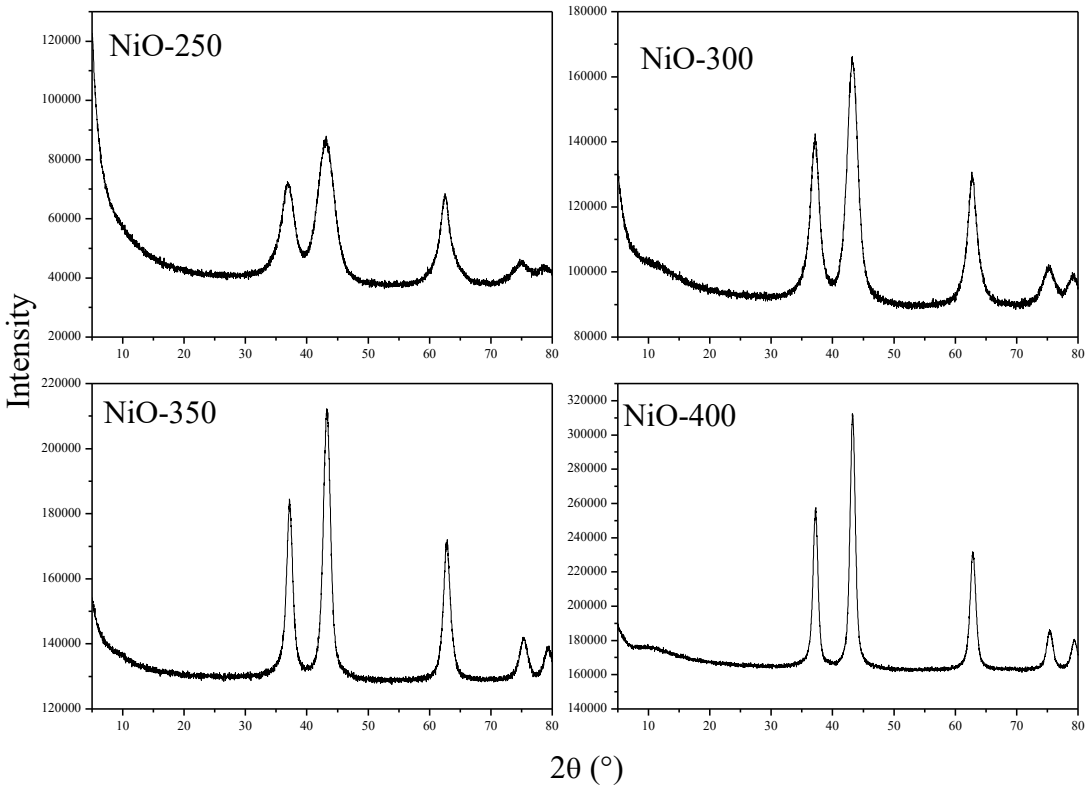

The main physical and chemical characteristics of nickel oxide are listed in Table 3.1. BET surface areas present a similar behavior to that found by Abbas and Jung [37] after calcination of mesoporous α-$Ni(OH)_2$. Particles coalescence during the rise in temperature, leading to an increase of particle sizes, and decrease of specific surface areas. The increasing number of contacts between the particles triggers an increase in mesoporosity [90].

Table 5: Main physical and chemical characteristics of nickel oxide obtained from the calcination of β-$Ni(OH)_2$ at 250 to 400 °C.

Sample	Sample Data				
	Cell Parameter (Å)	Crystallite size (Å)	BET Surface Area (m^2/g)	Pore Diameter (Å)	Bandgap energy (eV)
NiO-250	4.2008	28	245	35	2.45
NiO-300	4.1872	45	173	43	3.03
NiO-350	4.1816	70	131	57	3.41
NiO-400	4.1816	104	82	69	2.89

In the corresponding FTIR spectra (Figure 2), the strong band at 423 cm^{-1} corresponds to the bending vibration of NiO [78]. A broad band at about 3445 cm^{-1}, and a less intense band at 1624 cm^{-1} are related to the stretching and bending vibrations of water molecules adsorbed by the sample. As above, the bands observed at 1450 cm^{-1}, 1382 cm^{-1} and 1053 cm^{-1} are attributed to superficial carbonate groups; it is known that the calcined powder tends to chemisorb acidic compounds as CO_2 at basic sites [81, 89].

Figure 20: FTIR spectra of NiO samples after calcination of β-$Ni(OH)_2$ at 250 to 350 °C.

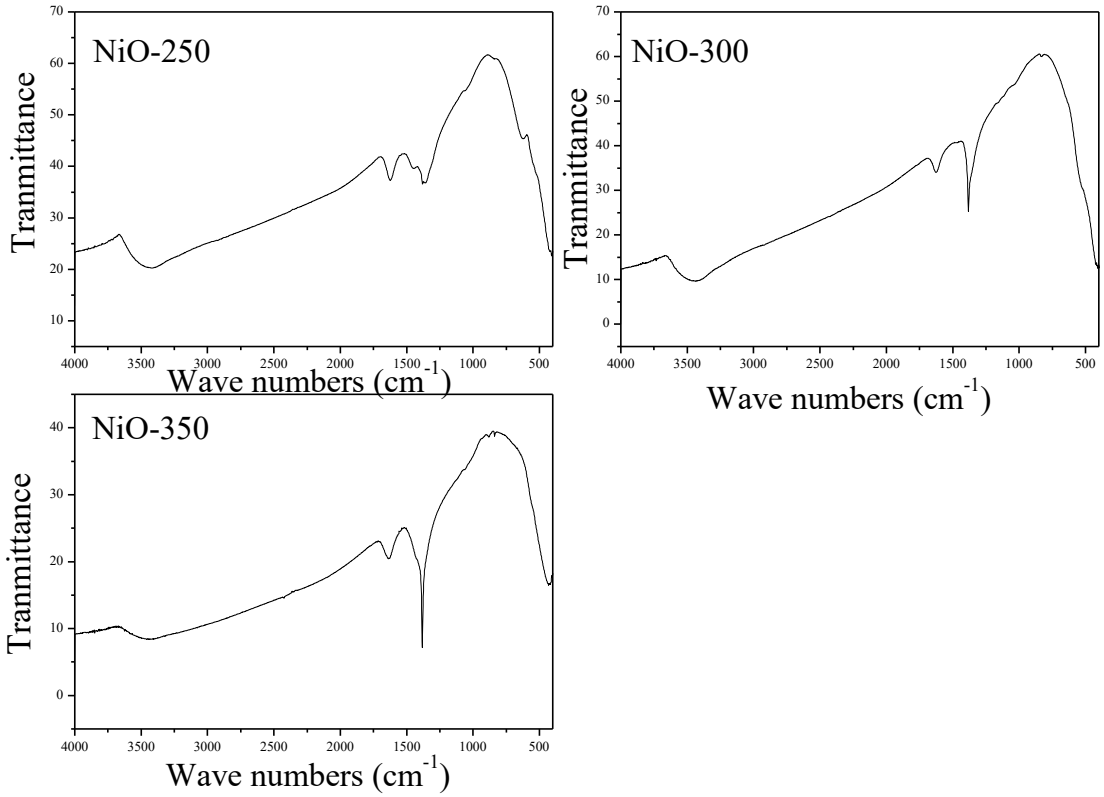

Figure 21 shows the diffuse reflectance UV–vis spectra of NiO, with bands at similar positions for all the samples. Based on Tanabe-Sugano diagrams, the strong band at 14,500 cm^{-1} and the weak band at 26,500 cm^{-1}, ascribed to the $^3A_{2g} \rightarrow {}^3T_{1g}(F)$ and $^3A_{2g} \rightarrow {}^3T_{1g}(P)$ electronic transition in octahedral Ni(II) ion, are fingerprints for NiO. The weak absorption band at 30,500 cm^{-1} and the broad band at 35,500 cm^{-1} are supposed to be absorption lines corresponding to $^4T_{1g}(F) \rightarrow {}^4T_{1g}(P)$ and $^4T_{1g}(F) \rightarrow {}^4A_{2g}(F)$, respectively, and are assigned to the transitions in octahedral Ni(III) ($3d^7$) ion. From the analysis of the graphs in Figure 5, it can be seen that the peaks attributed to Ni(III) ions in relation to Ni(II) increase proportionally for the sample calcined at 250 to 300 °C and from 300 to 350 °C but decrease from 350 to 400 ºC. Samples calcined at 300 and 400 °C provide very similar Ni(III) concentrations.

Figure 21: Diffuse reflectance UV–vis spectra of the NiO samples obtained after the calcination of β-$Ni(OH)_2$ at 250 to 400 °C.

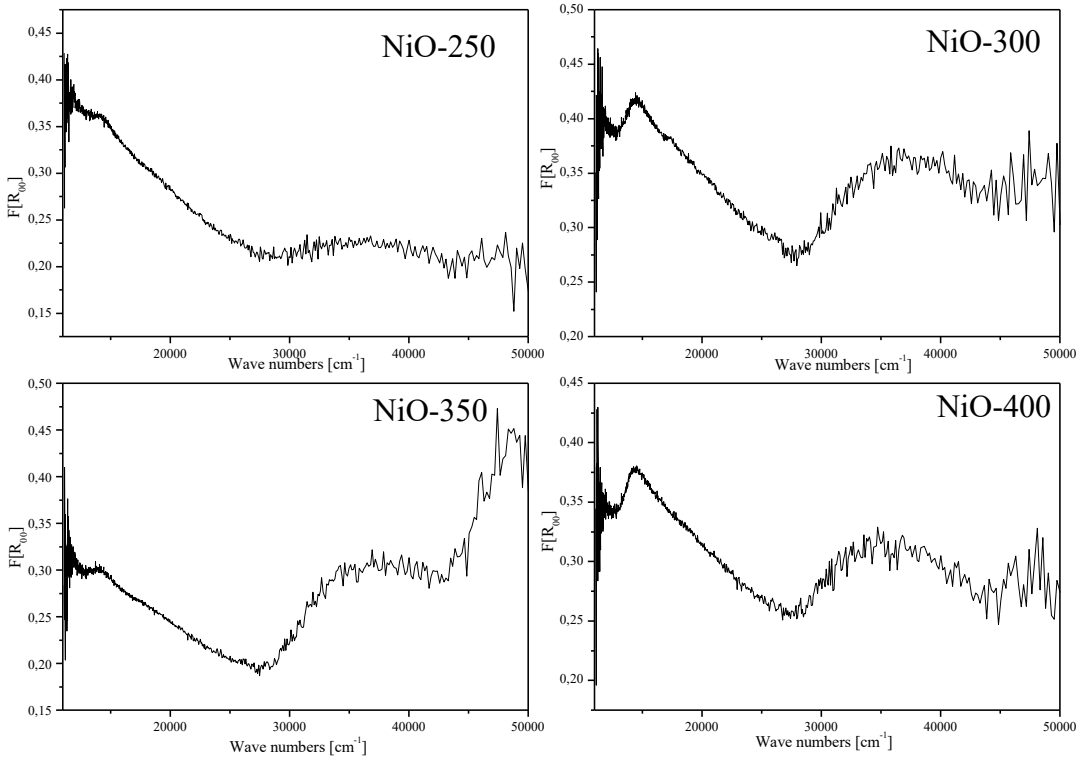

The optical band gaps Eg have been estimated by extrapolating the linear fitted region at $[F(R_\infty)h\upsilon]^2 = 0$ in the plot of $[F(R_\infty)h\ \upsilon]^2$ versus $h\cdot\upsilon$ in Figure 22. The Eg values obtained are listed in Table 5. The highest values of bandgap energy were observed for the beta nickel hydroxide precursor calcined at 350°C (3.41 eV). This value is close to that obtained by Zhu et al. [48] for NiO with flower-like morphology, which presented gap energy

between 3.12-3.41 eV, increasing with calcination temperature (300 to 500°C). However, NiO thin films developed by Shadrach et al. [47] showed a decrease in gap energy, 3.71, 3.64 and 3.55 eV with an increase in the calcination temperature (400 to 600 °C). This shows that the bandgap energy is strongly influenced by the morphology of the oxide.

Figure 22: Optical bandgap of NiO samples obtained after the calcination of β-$Ni(OH)_2$ at 250 to 400 °C.

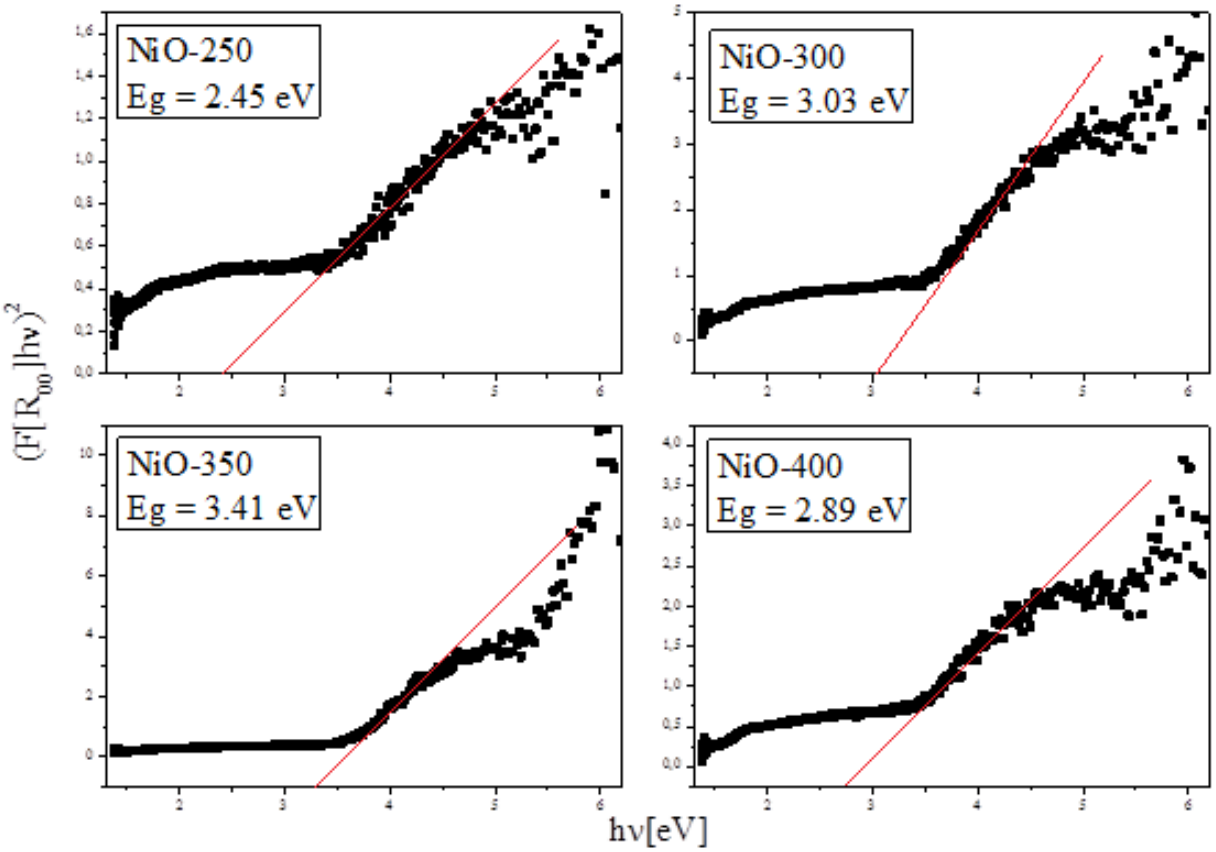

Figure 23 shows SEM images of the β-$Ni(OH)_2$ samples calcined between 250 and 400 °C. The samples presented heterogeneity of particle sizes, mostly over 1 µm. In general, they are sponge-like with laminar structures and high porosity. There are no important differences in shape regardless of the calcination temperatures.

Figure 23: SEM images at different magnifications of NiO after the calcination of β-$Ni(OH)_2$ at 250 to 400 °C.

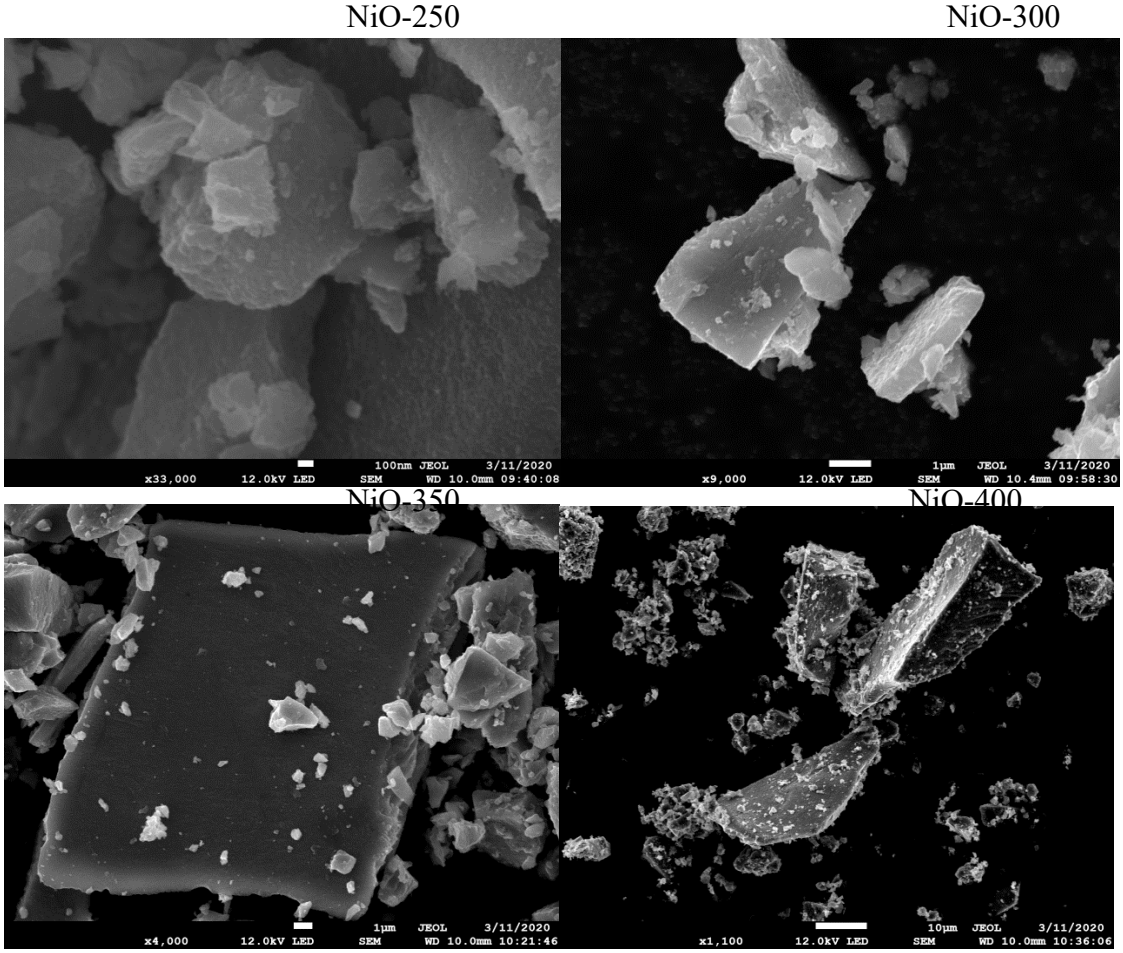

3.1.6 Catalytic performance

Nickel oxide activity was tested in the ODH reaction of ethane. Ethane conversion and selectivity to ethylene are shown in Figure 24 as a function of reaction temperature. All materials in this series show temperature dependence. For conversions close to 20%, the same materials present selectivity up to 60% ethylene. The samples calcined at 250 and 400 °C showed a maximum selectivity of 55%. NiO-300 exhibited the highest conversion at 270 °C with an appreciable selectivity of 60%.

Figure 24: Catalytic performance of nickel oxide catalysts for ODH of ethene after the calcination of β-Ni(OH)2 at 250 to 400 °C.

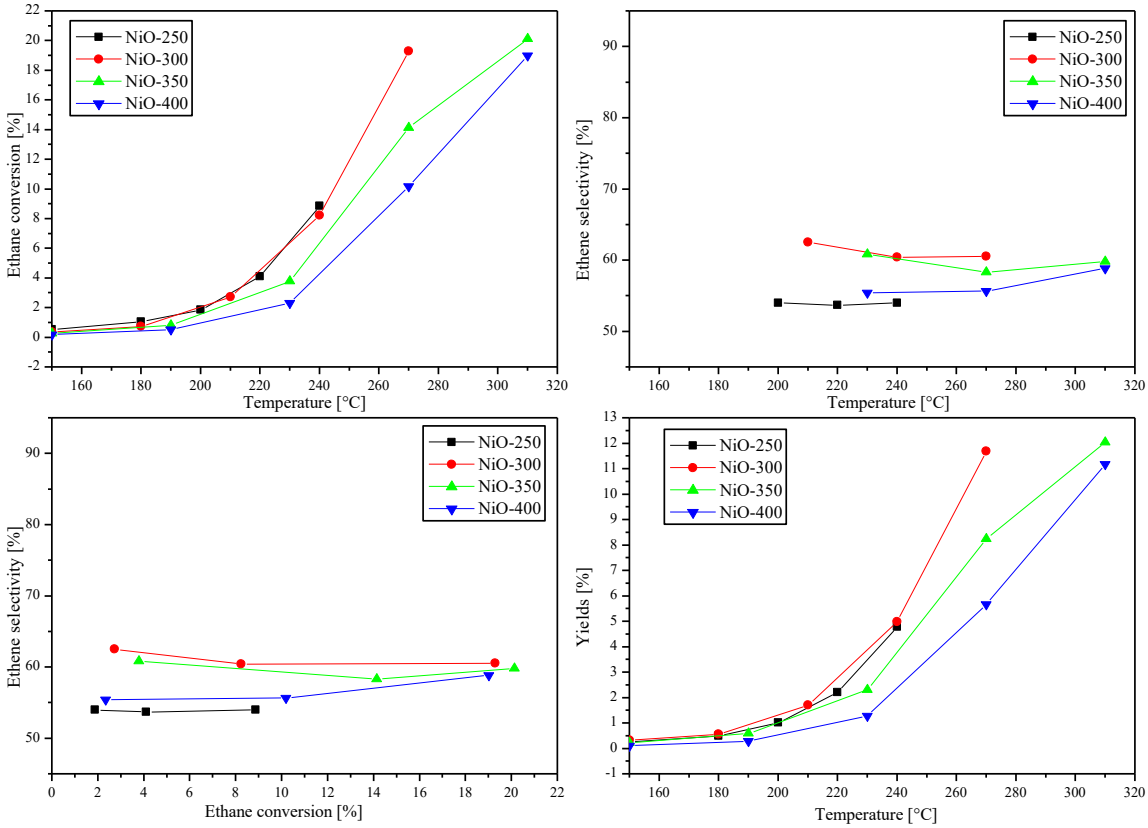

Table 6 compares the catalytic performance of all oxides in the oxidative dehydrogenation reaction of ethane at different temperatures. At 240 °C the samples showed increasing selectivity in this sequence: NiO-250 = NiO-400 < NiO-300 = NiO-350. The conversion follows a different order: NiO-250 > NiO-300 > NiO-350 > NiO-400. The best yield of the process at 240 °C was obtained for the sample prepared at 300°C. The tests carried out at 270 °C show a tendency to decrease conversion with increasing calcination temperature, but similar selectivity.

Table 6: Catalytic performance of nickel oxides obtained by heat treatment at 250 to 400 °C.

Sample	**Catalytic performance**					
	240 °C		**270 °C**		**310 °C**	
	Conversion (%)	**Selectivity (Ethene) [%]**	**Conversion (%)**	**Selectivity (Ethene) [%]**	**Conversion (%)**	**Selectivity (Ethene) [%]**
NiO-250	8.75	55	_	_	_	_
NiO-300	8.24	60	19.5	60	_	_
NiO-350	6.7	60	14	58	20.3	60.7
NiO-400	4.25	55	10	55	19.3	60.4

Table 7 gives the intrinsic activity at different temperatures in ethane ODH and the apparent activation energies Ea/R for the four samples. Ea/R values were determined from the slopes of the Arrhenius plots shown in Figure 25 in the temperature range from 180 to 270°C. The reaction of ethane carried out at 240 °C, 270 °C and 310 °C shows an increase in intrinsic activity with increasing temperature of calcination of the samples. Apparent activation energies, however, are all similarly about 77 kJ/mol, in agreement with reported values (see Table 8). The possibility of influence of the band-gap energy measured at room temperature on the apparent activation energy was not verified as in the work developed by bell. The results suggest the values of apparent activation energy follow qualitatively that the Ni (III) content according to the UV-Vis curves.

Table 7: kinetic properties of nickel oxides obtained by heat treatment at 250 to 400 °C.

Sample	intrinsic activity (mol m^{-2} s^{-1})			Activation
	240 °C	270 °C	310 °C	Energy (kJ/mol)
NiO-250	4.82×10^{-10}	_	_	78.4
NiO-300	6.37×10^{-10}	15.00×10^{-10}	_	77.8
NiO-350	6.67×10^{-10}	14.40×10^{-10}	20.50×10^{-10}	74.7
NiO-400	7.26×10^{-10}	16.61×10^{-10}	31.00×10^{-10}	76.6

Figure 25: Arrhenius plots of ln(intrinsic activity) vs. 1000/T for ethane ODH using nickel oxides catalysts after heat treatment in the range 250 - 400 °C.

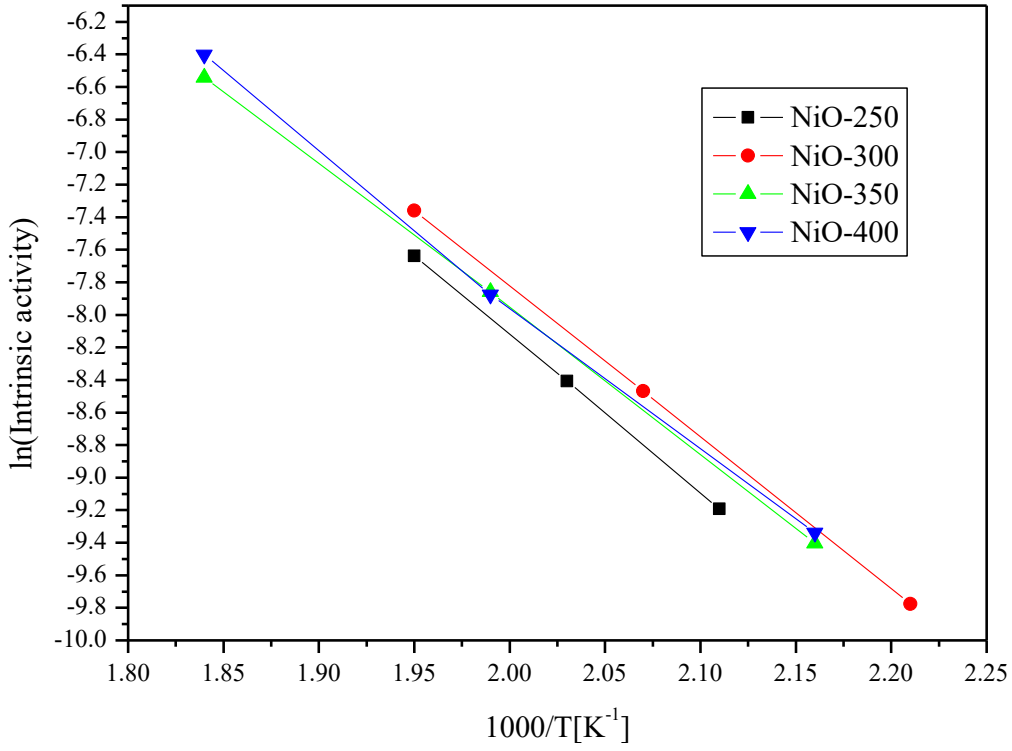

Table 8 presents a summary of physical characteristics of three nickel oxide prepared by heat treatment and the catalytic performance together with its kinetic properties. The first NiO sample, prepared by partial reduction with oxalic acid and thermally decomposed, was tested in the work developed by Savova et al. [43]. The reaction was conducted at 350 °C fed with a mixture of O_2:C_2H_6:N_2 = 9:9:82 and the weight to flow ratio (W/F) of 0.54 g.s/mL. Santander et al. [91] prepared Ni–Nb mixed oxides sample by alternative technique. In this case, the ODH test for ethane was performed at 350 °C, feeding by a mixture of O_2/C_2H_6/He with a 5/5/90 M ratio, and the catalyst weight-to-flow rate (W/F) was 0.54 g s/mL. Zhu et al. [57] studied the effect of NiO preparation method in their catalytic performance. The ODH reaction was conducted at 300 °C, the gas mixture of 10% C_2H_6/10% O_2 in He was introduced through the catalytic bed with W/F = 0.6 g s/mL.

Table 8: Summary of the physical and chemical characteristics, and catalytic performance for nickel oxide in selected works

Sample	S_{BET}	P. Size	W/F	Catalytic performance				A. Energy	Reference
NiO-T(°C)	(m2/g)	(nm)	g.s/mL	T. ºC	X (%)	S. Ethene (%)	ν, $mol.m^{-2}.s^{-1}$	(kJ /mol)	
450	12	28	0.54	350	12	31	5.1×10^{-8}	78	[43]
450	30	46	0.54	350	14	19	1.8×10^{-8}	_	[91]
400	65	8	0.60	300	15	55	1.76×10^{-8}	79	[57]

NiO-T (calcination temperature), S_{BET} (BET Surface Area), W/F (catalyst weight-to-flow rate), T. (Reaction Temperature), X (Ethane Conversion), **ν** (intrinsic rate),

The best performance in ethane ODH was described by Zhu et al. [57] presenting a conversion of 15 %, ethene selectivity of 55% and intrinsic rate of 1.8×10^{-8} $mol.m^{-2}$ s^{-1} on test at 300 °C. For comparative purposes, the selected reference oxides [43, 57] had close values of apparent activation energy to those reported in this work. It is also worth noting that intrinsic activity varies in opposite direction to surface area, as also observed in Table 3.3.

In contrast with the results reported by Getsoian et al. [48], no influence of the band-gap energy on the apparent activation energy, nor on the activity of the catalysts, was observed in this work. UV-Vis data (Figures 3.5 and 3.6) indicates that band-gap energy values qualitatively follow the Ni(III) content, as estimated from the area of the broad band at 35,500 cm^{-1}. Both results are certainly representative of bulk properties, but might also be correlated to surface properties, in particular to surface Ni(III) or defect content. What our data really suggests is that intrinsic activity increases with the crystallinity of the sample, which, of course, increases with calcination temperature. Interestingly, selectivity to ethene was approximately independent on sample treatment, conversion and reaction temperature

3.1.7 Conclusions

Different Nickel oxides have been prepared by a precipitation-oxidation method followed by heat-treatment in air at different temperatures and studied as catalysts for ethane ODH reaction. All samples showed little variation in selectivity to ethene, with values close to 60%, whatever the calcination temperature or reaction conditions be. The apparent activation energy was found to be independent of Ni(III) content and band-gap energy. Although the activity of the oxide decreased with calcination, as expected from the decrease of specific area, we observed that more crystalline samples displayed the highest intrinsic activity. The results suggest that for the best catalytic performance, NiO catalysts should have both high crystallinity and large surface area.

3.2 EFFECT OF PROMOTER CONCENTRATION

3.2.1Physical and chemical properties

The precursor phases and the oxides obtained from thermal treatment were identified through XRD patterns and FTIR spectra.

Figure 26 illustrates the very amorphous XRD pattern for the precursor sample of the oxides; the broad peaks at 2θ = 10.0, 34.4 and 60.0 can nevertheless be assigned to planes (003), (012) and (110) of the hexagonal structure of alpha nickel hydroxide. The intensity of 2θ = 10.0 peak is stronger than the other, indicating that (003) plane may be preferred growth direction. This structure presents lamellar structure interspersed by water molecules and anionic carbonate similar to structures known as hydrotalcites [77]. The identification of these interlayer species was complemented with the analysis of FTIR spectra (Figure 27). The broad band at 3440 cm^{-1} and another less intense band at 1634 cm^{-1} were assigned to interlayer water molecule [77]. The bands at 1464 and 1400 cm^{-1} are primarily due to the bending vibration of CO_3^{2-} related to asymmetric stretching. The spectrum also exhibits a band at 1065 cm^{-1} attributed to symmetric stretching of CO_3^{2-}, and two bands at 838 and 700 cm^{-1} which correspond to the out-of-plane and in-plane bending vibration of carbonate, respectively. This means that CO_3 ions are not free in the interlamellar space but interact with nickel ions of the Brucite-type layers as for unidentate complexes. The peak at 407 cm^{-1}corresponds to ν(Ni–O) the bending vibrations in α-$Ni(OH)_2$. [78].

Figure 26: XRD pattern of the synthesized sample of α-Ni(OH)$_2$

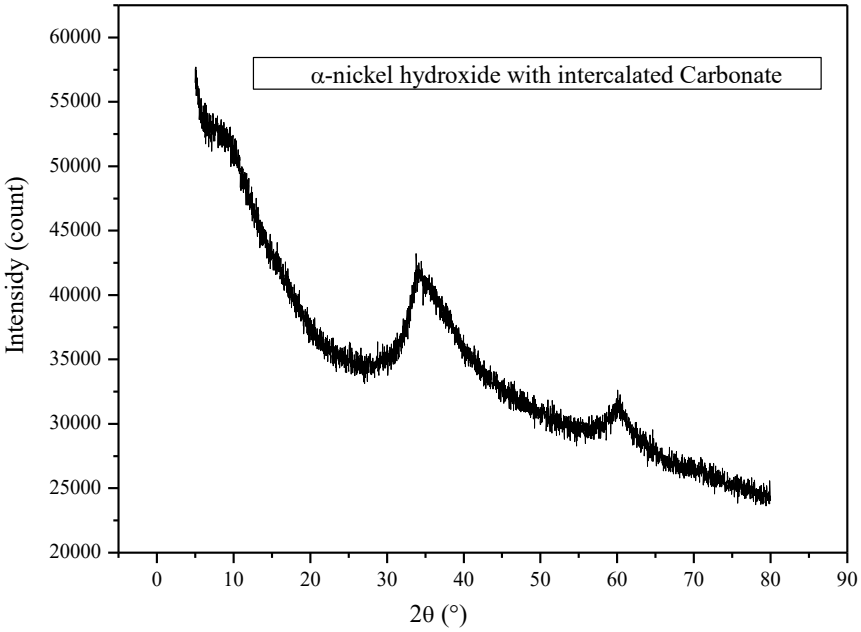

Figure 27: FTIR spectrum of the synthesized sample of α-Ni(OH)$_2$.

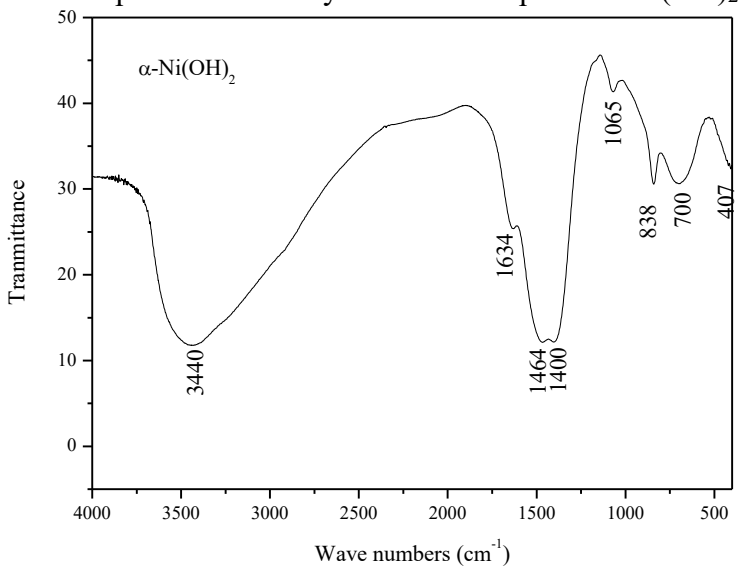

Figure 28 depicts the XRD patterns obtained after heat treatment of alpha nickel hydroxide according to experimental design. The same peaks are observed in all the XRD patterns and correspond to the (111), (200), (220), (311) and (222) crystallographic planes from the cubic crystal structure of NiO (space group Fm-3m), in agreement with standard data ICSD- 9866. Overall, the XRD analysis showed a single phase with small variations in the cell parameter, as shown in Table 9. The values of crystallite size calculated from XRD patterns by using the Scherrer equation are shown in the same table, according to 2^3 factorial design with center point in triplicate. The results indicate a direct influence of the treatment

temperature of the precursors in the properties of the nickel oxides obtained, showing an increased crystal size of NiO with calcination temperature. The largest crystallite size occurred in the samples calcined at 400 °C.

Figure 28: XRD standard of non-stoichiometric NiO samples after heat treatment of α-$Ni(OH)_2$

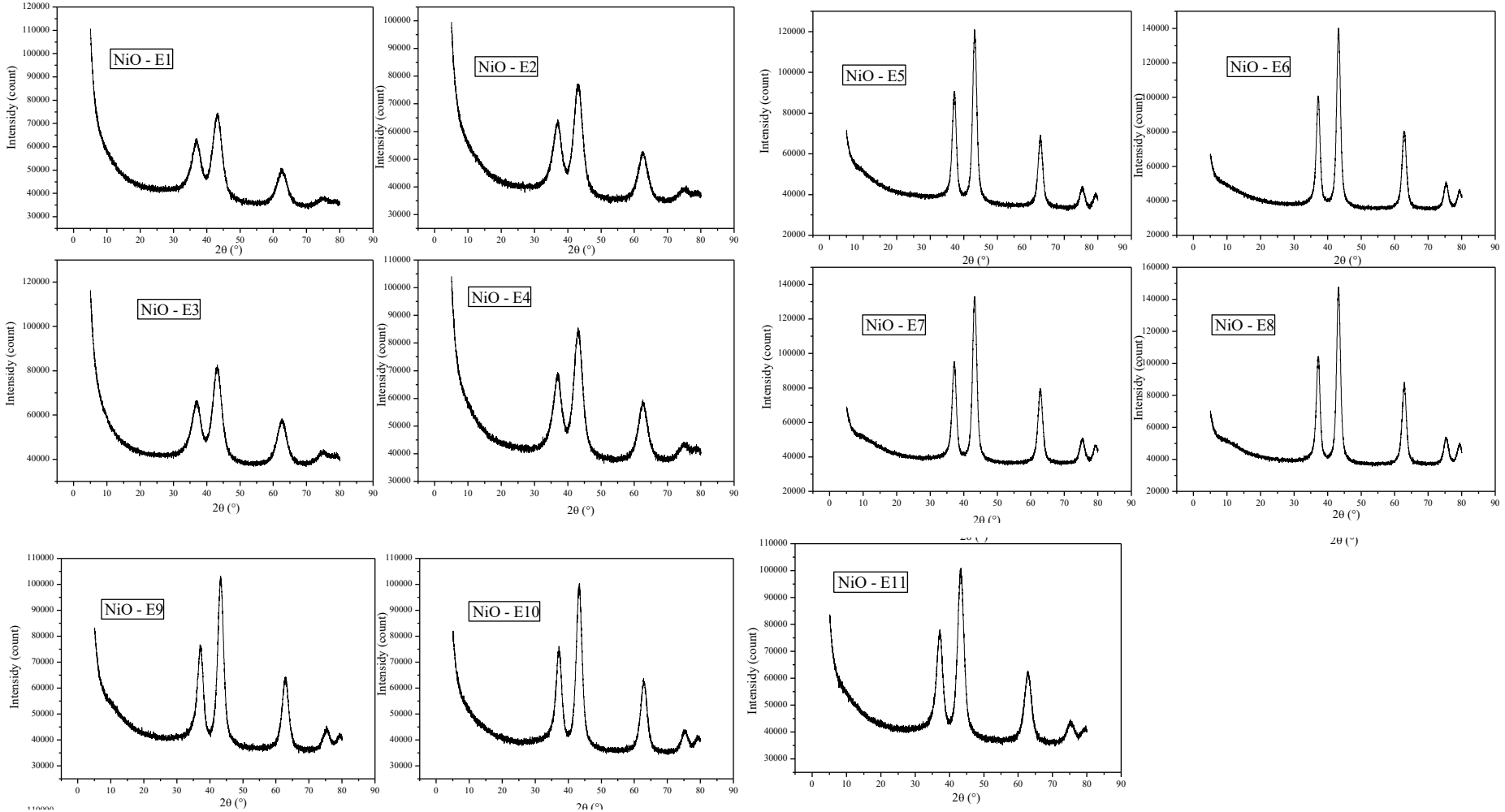

Table 9: Main physical and chemical characteristics of nickel oxide obtained from the calcination of α-$Ni(OH)_2$.

Sample	Variables			Sample data			
	Washing T. (°C)	R. Time (h)	Calc. T. (°c)	Cell p. (Å)	C. size (Å)	Eg [eV]	Comp. (Na %)
E-1	0	1	300	41.979	27	3.20	1.7
E-2	50	1	300	42.011	29	3.17	0.8
E-3	0	9	300	41.992	29	2.84	1.2
E-4	50	9	300	41.998	30	2.20	0.7
E-5	0	1	400	41.840	65	3.42	1.9
E-6	50	1	400	41.836	73	3.43	0.5
E-7	0	9	400	41.848	68	2.21	2.1
E-8	50	9	400	41.839	72	2.93	0.9
E-9	25	5	350	41.860	45	3.25	3.3
E-10	25	5	350	41.835	45	3.12	3.0
E-11	25	5	350	41.855	45	3.30	2.4

T. (temperature); R. (reaction); Cell p. (cell parameter); c. size (crystal size); S (surface); comp. (composition)

The analysis of the effects showed that calcination temperature was the most significant factor determining crystal size, with contributions of 81.39 (Figure 29). Only the interaction between calcination temperature and reaction time showed significant effects, but small contribution. The lack of fit was not significant and the mathematical equation and the regression coefficient obtained for this model are reported in equation 4. The interaction effects which were not significant were removed from the model equation. The response surface is shown in Figure 29. The curvature of the model was significant (measured by difference between the average of the center points and the average of the factorial points) in the design space.

$$Y= 45.85 + 2X_1 + 0.63X_2 + 20.47X_3 + 1.00X_1X_2 +3.22X_1^2 \quad (4)$$

where Y is the crystal size, X_1 is the washing temperature, X_2 is the reaction time and X_3 is the calcination temperature. R^2=0.9996; Adj:0.99866

Figure 29: Pareto (α = 0.05) and response surface for the analyses of crystal size

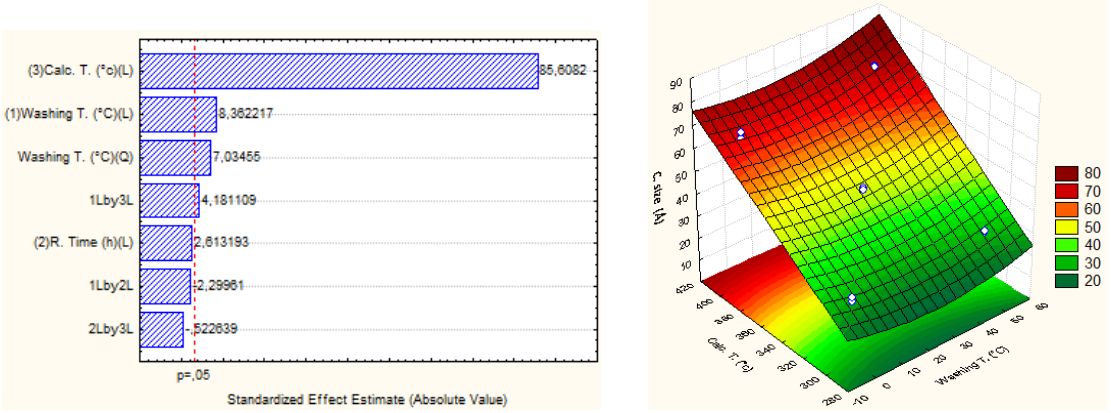

The analysis of the effects showed only the term quadratic of washing temperature as the significant factor for sample composition. The curvature of the model was significant (measured by difference between the average of the center points and the average of the factorial points) in the design space. The response surface is shown in Figure 30.

Figure 30: Pareto (α = 0.05) and response surface for the analyses of composition

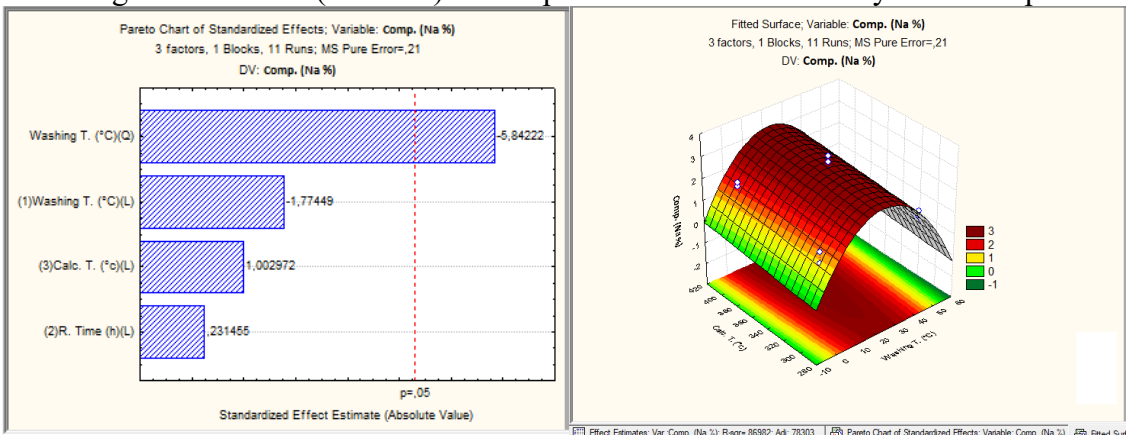

R^2=0.86982; Adj:0.78303

In the FTIR spectra corresponding to the experimental design (Figure 31) the strong band at 423 cm^{-1}corresponds to the banding vibration of NiO [45]. The broad band at about 3445 cm^{-1}, and another less intense band at 1624 cm^{-1} are related to the stretching and bending vibrations of the water molecules adsorbed by the sample. The bands at 1460, 1383, 1053, 840 and 700 cm^{-1} in Figure 4.6 are attributed to carbonate groups due to the fact that the calcined powder tends to chemisorb acidic compounds as CO_2 at basic sites [46, 47].

Figure 31: FTIR spectra of NiO samples after calcination of α-$Ni(OH)_2$

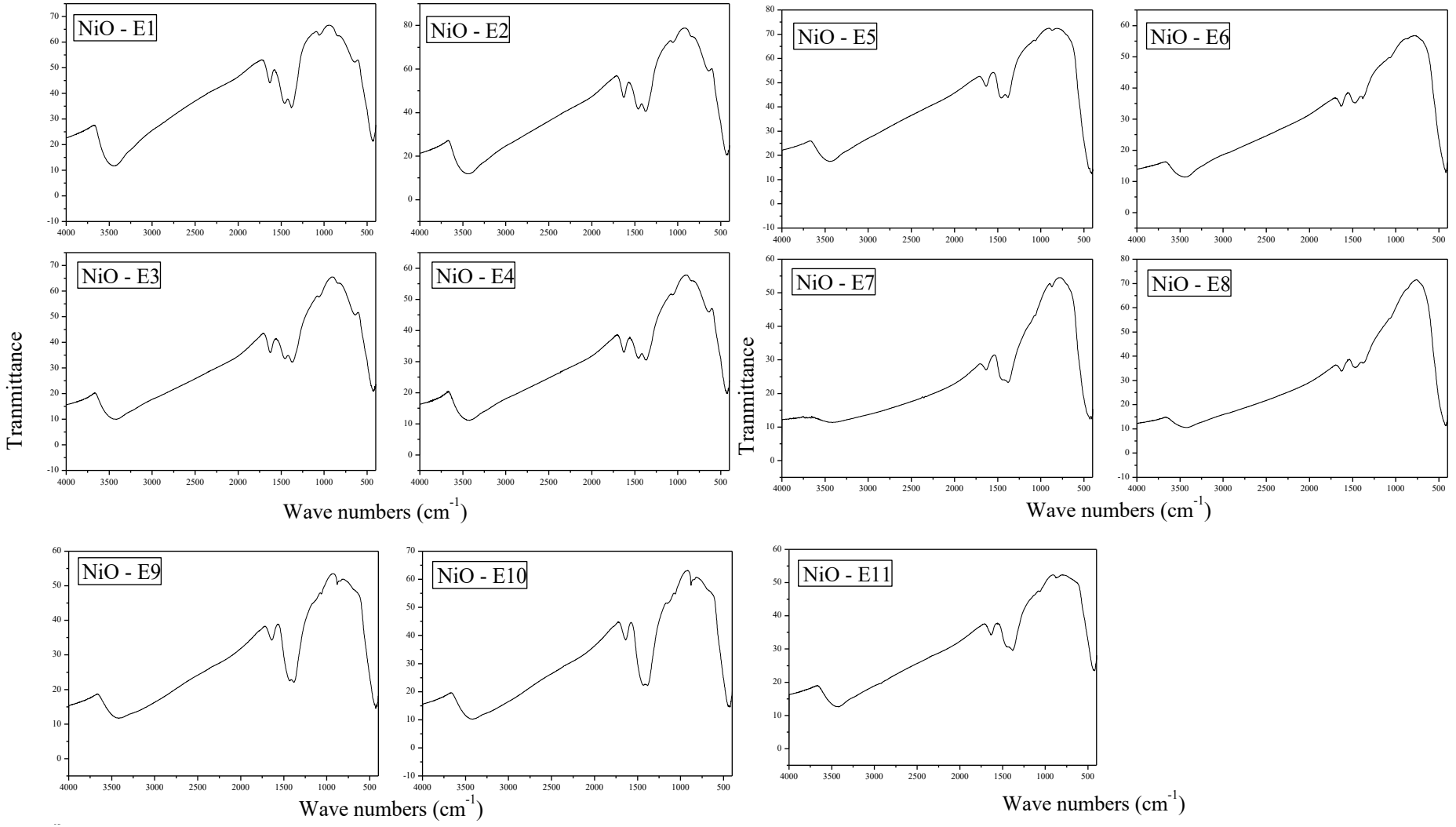

Figure 32 shows the diffuse reflectance UV–vis spectra of NiO, with bands at similar positions for all the samples. Based on Tanabe-Sugano diagrams, the strong band at 14,500 cm^{-1} and the weak band at 26,500 cm^{-1}, ascribed to the $^3A_{2g} \rightarrow {}^3T_{1g}(F)$ and $^3A_{2g} \rightarrow {}^3T_{1g}(P)$ electronic transition in octahedral Ni(II) ion, are fingerprints for NiO. The weak absorption band at 30,500 cm^{-1} and the broad band at 35,500 cm^{-1} are supposed to be absorption lines corresponding to $^4T_{1g}(F) \rightarrow {}^4T_{1g}(P)$ and $^4T_{1g}(F) \rightarrow {}^4A_{2g}(F)$, respectively, and are assigned to the transitions in octahedral Ni(III) ($3d^7$) ion. From the analysis of the graphs in Figure 4.**7**, it can be seen that the peaks attributed to Ni(III) ions in relation to Ni(II) are much larger proportionally for the samples E-1, E-5, E-6, E-9 and E11. For the sample E-4 and E-7 this proportion appears to be lower and the samples E-2, E-3, E-8 and E-10 provide Ni(III) concentrations a little larger than Ni(II).

Figure 32: Diffuse reflectance UV–vis spectra of the NiO samples obtained after the calcination of α -$Ni(OH)_2$

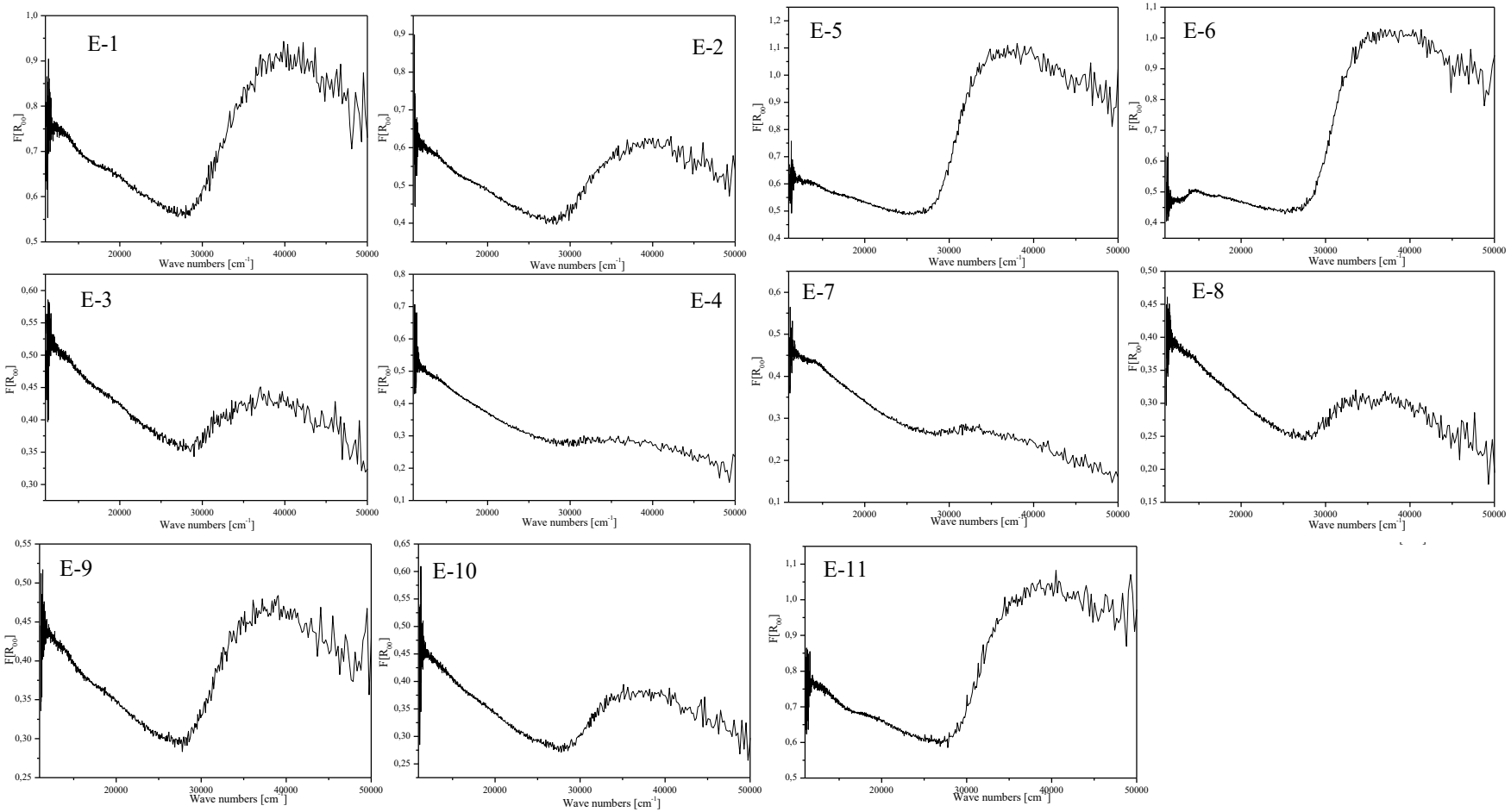

The optical band gaps Eg have been estimated by extrapolating the linear fitted region at $[F(R_\infty)h\upsilon]^2 = 0$ in the plot of $[F(R_\infty)h\ \upsilon]^2$ versus $h\cdot\upsilon$ in Figure 34. The Eg values obtained are listed in Table 9. Most of the samples presented values of energy band gap close to and slightly higher than 3.00 eV, the highest value was observed in E-6 (3.43) and the lowest values for E-4 and E-7 (2.2eV).

The analyses of the effects showed only the term washing temperature were the most significant with a negative contribution of 53.35 %. Only the interaction between calcination temperature and washing temperature showed significant effects. The lack of fit was not significant and the mathematical equation and the regression coefficient obtained for this model are reported in equation 5. The interaction effects which were not significant were removed from the model equation. The curvature of the model was significant (measured by difference between the average of the center points and the average of the factorial points) in the design space. The response surface is shown in Figure 33.

$$Y= 3.22+ 0.01X_1 - 0.38X_2 + 0.07X_3 + 0.18X_1X_3 - 0.30X_1^2 \qquad (5)$$

Where Y is the crystal size, X_1 is the washing temperature, X_2 is the reaction time and X_3 is the calcination temperature. R^2=0.8655; Adj:0.73101

Figure 33: Pareto (α = 0.05) and response surface for the optical band gaps Eg

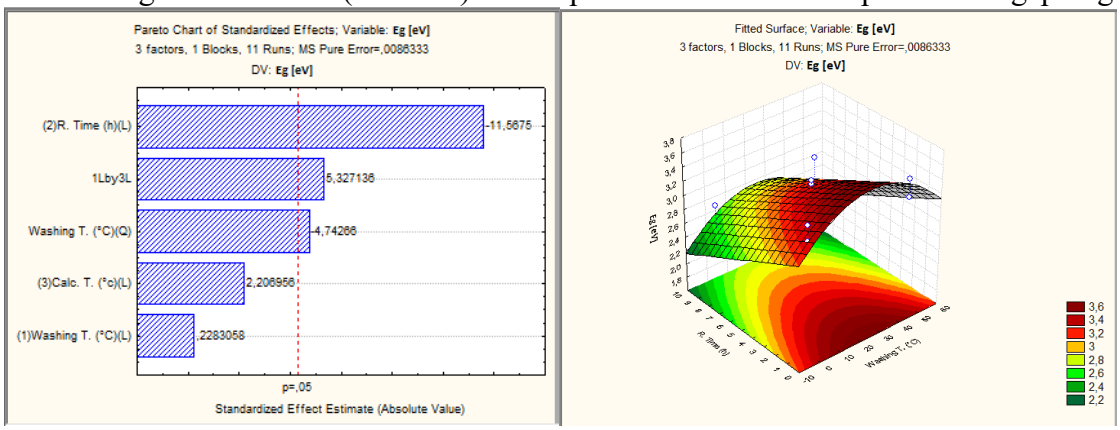

Figure 34: Optical bandgap of NiO samples obtained after the calcination of α-$Ni(OH)_2$.

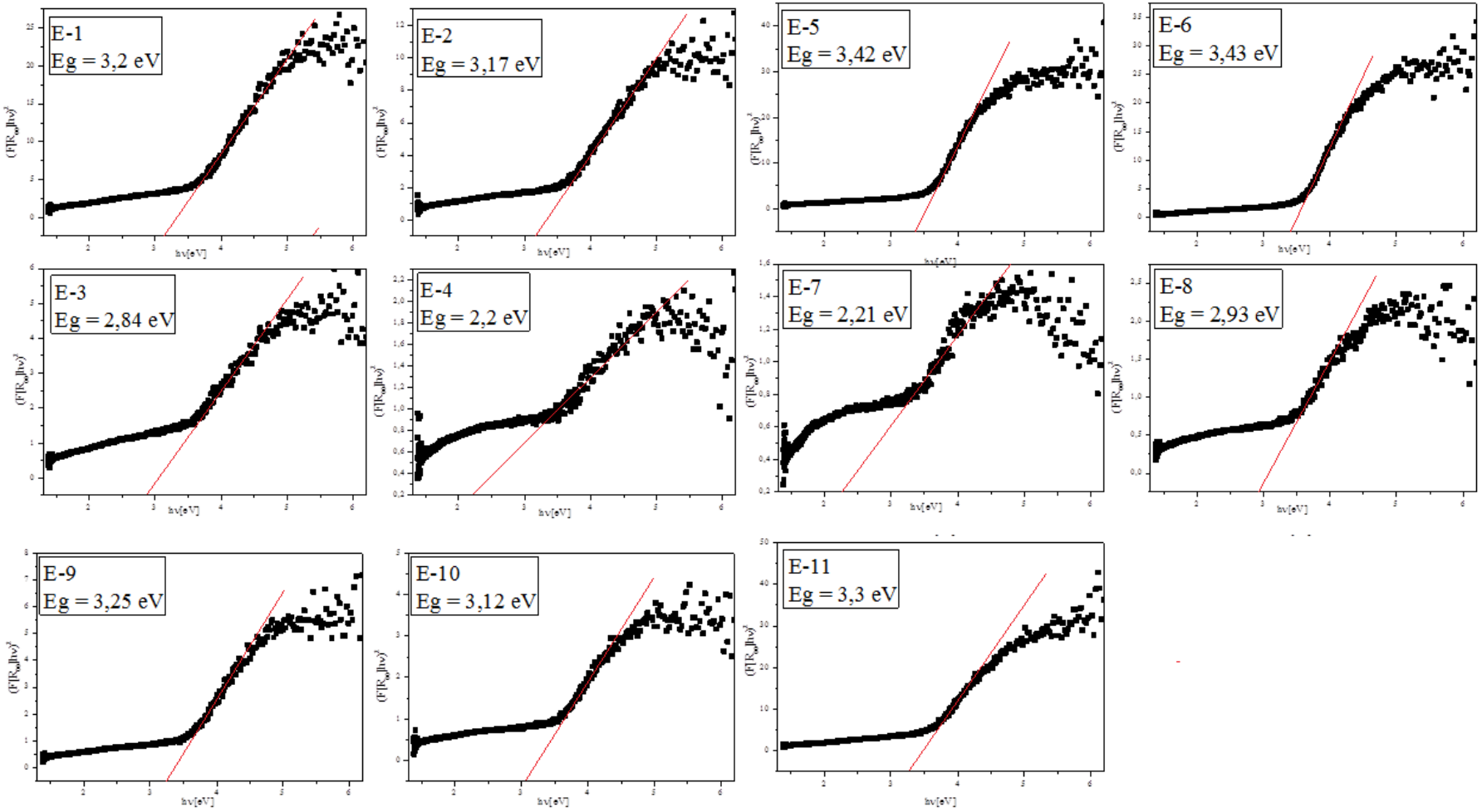

Figure 35 shows SEM images of nickel oxides originated from E-1 to E-4 samples. Despite the poor quality of the images they present clusters of particles in the form of porous plates. Apparently, there are no important differences in morphology between these four samples.

Figure 35: SEM image at different magnification of NiO for E-1 to E-4 samples.

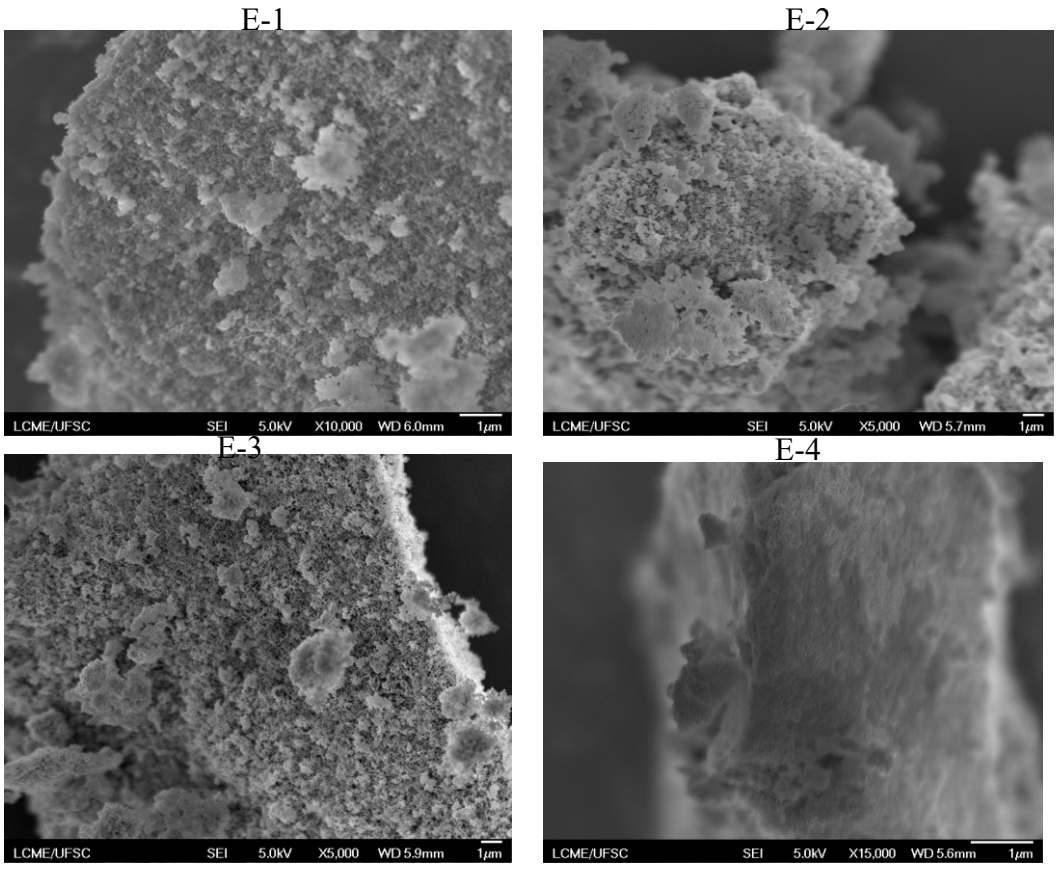

For transmission microscopy we selected three samples treated at different temperature: E-2, E-7 and E-10 (Figure 36). The NiO samples indeed show essentially nanoparticles of average diameter less than 5 nm. All the electron diffraction spots display the crystalline signature of NiO for the area of the analyzed samples.

Figure 36: TEM image at different magnification of NiO for E-2, E-7 and E-10 samples

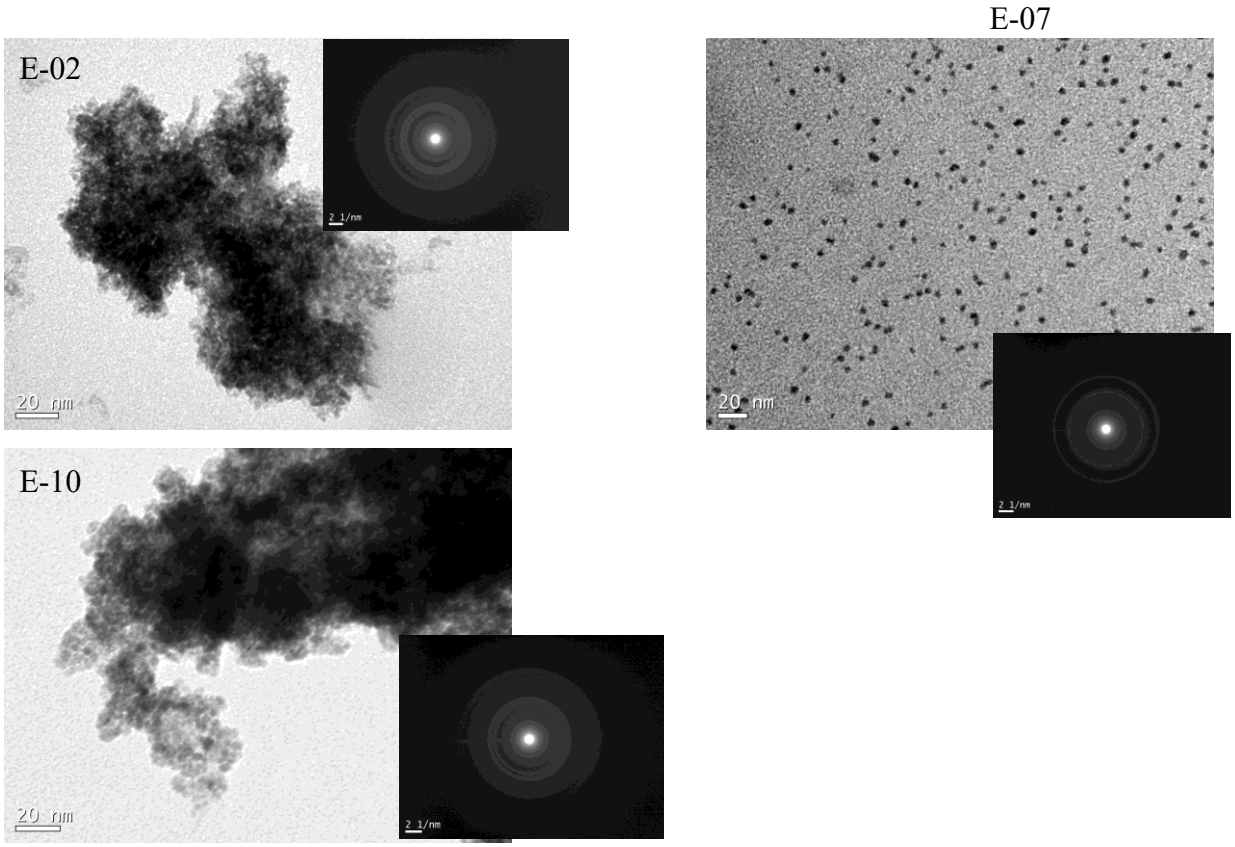

Catalytic performance

Activity of the different samples was tested in the ODH reaction of ethane. Ethane conversion and selectivity to ethylene are shown in Figure 37 as a function of reaction temperature. The materials that show better selectivity in this series were those that exhibited the lowest conversions. Sample E-2 exhibited the highest conversion (22%) at 270 °C with an appreciable selectivity of 66%. A maximum selectivity of 92% was given by sample E-9 at a conversion of 7%. The best yield was obtained for sample E-2 calcined at 300°C.

.

Figure 37: Catalytic performance of nickel oxide catalysts for ODH of ethene after the calcination of α-Ni(OH)$_2$.

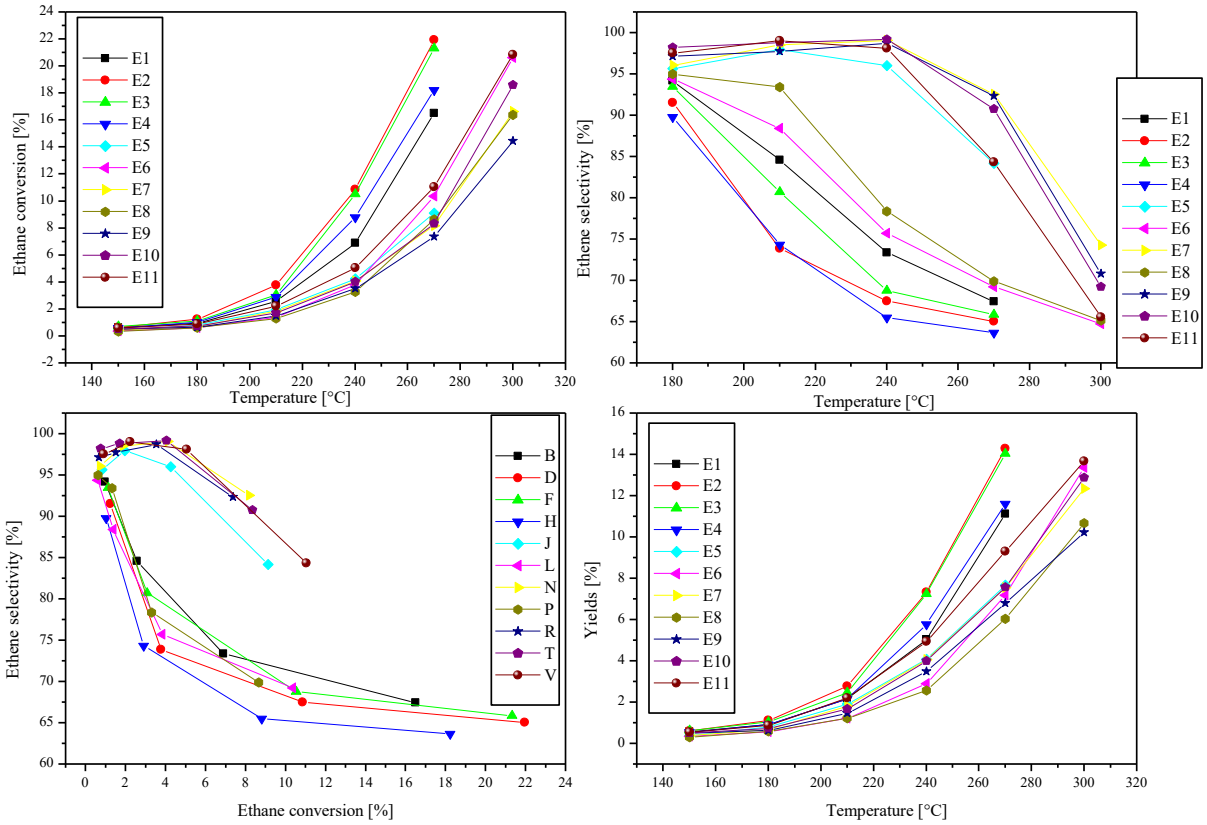

Table 10 compares the catalytic performance of all oxides in the oxidative dehydrogenation reaction of ethane at 270 and 300 °C. At 270 °C the samples showed increasing selectivity in this sequence: E-4 < E-2 < E-3 < E-1 < E6 < E-8 < E-5 = E11 < E-10 < E-7 = E-9. The conversion followed a different order: E-2 > E-3 > E-4 > E-1 > E11 > E-6 < E-5 > E-7 = E-8 = E-10 > E-9. The tests carried out at 270 °C showed a tendency to decrease conversion with increasing selectivity.

.

Table 10: Catalytic performance of nickel oxides obtained by heat treatment.

Sample	Catalytic performance at 270°C		Catalytic performance at 300°C	
	X (%)	S. (Ethene) [%]	X (%)	S. (Ethene) [%]
E-1	16	68		
E-2	22	66		
E-3	21	67		
E-4	18	64		
E-5	9	84		
E-6	10	69	20	65
E-7	8	92	16	64
E-8	8	70	16	65
E-9	7	92	14	71
E-10	8	90	18	69
E-11	11	84	21	65

The analysis of the effects showed that calcination temperature is the only significant factor. The curvature of the model was significant (measured by difference between the average of the center points and the average of the factorial points for washing temperature) in the design space as shown in Figure 38 in response surface. Analysis of the influence of the washing temperature on the conversion indicates that after a certain concentration, the sodium in the sample has an inhibitory effect on the activity. Thus, the samples with the highest sodium concentration showed the lowest conversion.

Figure 38: Pareto (α = 0.05) and response surface for the ethane conversion.

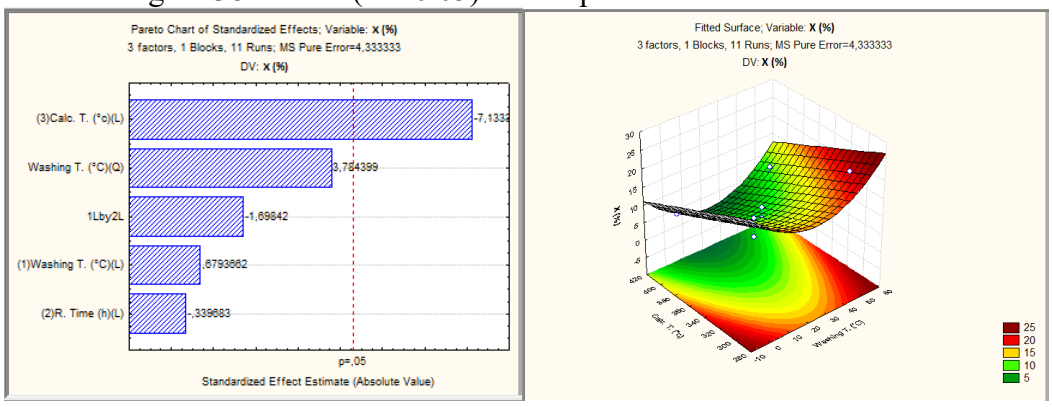

R^2=0.93949; Adj:0.87897.

The analysis of the effects showed that only the quadratic term of washing temperature is the significant factor. The curvature of the model was significant (measured by difference between the average of the center points and the average of the factorial points for

washing temperature) in the design space is shown in Figure 39 in response surface. The calcination temperature also has an influence on the selectivity of the sample, but it is not significant. Contrary to conversion the presence of sodium has a beneficial effect on selectivity. The samples with the highest sodium concentration showed the best performance in terms of selectivity.

Figure 39: Pareto (α = 0.05) and response surface for the ethane selectivity.

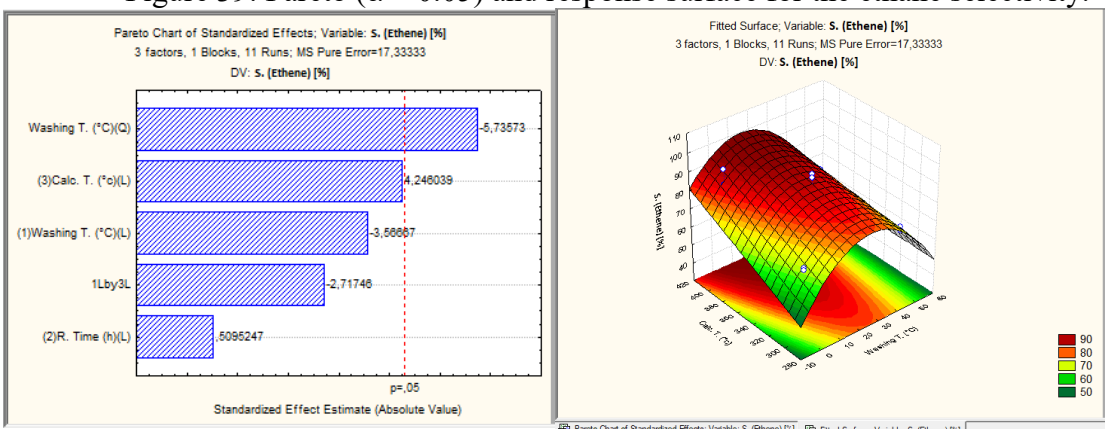

R^2=0.94991; Adj:0.89981

Along with catalytic activity, the stability on stream is an important characteristic of the catalysts. The stability was tested during 90 minutes with measurement every 10 minutes. Different responses, however, were observed for conversion and selectivity at 270 °C, as shown in Figure 40. The results showed us a slight drop in conversion over time and a sharp drop in selectivity mainly for those samples with the highest sodium content.

Figure 40: Catalytic performance of Oxide every 10 minute of reaction at 270 °C.

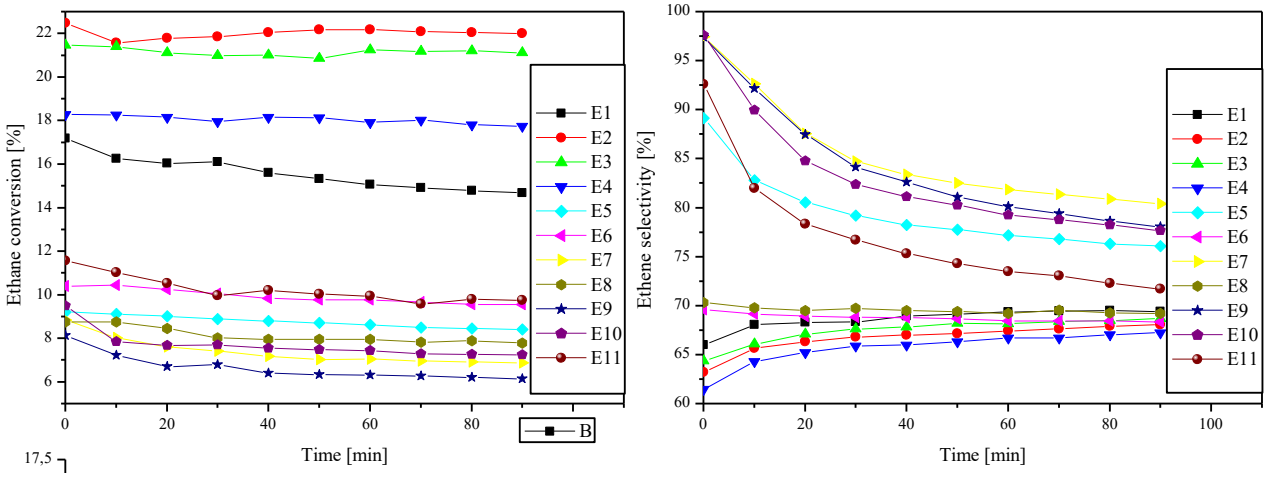

Although the interactions between the analyzed parameters did not show a significant effect for the catalytic properties at the conditions of the study, but it helped to understand the

influence of these factors on the process. The catalytic data show a significant decrease in the ethane conversion for samples with high sodium content, indicating that deactivation may be related to poisoning. The sodium ions used as promoters are considered strong acids, possibly electronically modifying neighboring oxygen atoms as well as metals, thus altering their ability to adsorb and/or dissociate reactant molecules [35, 48]. Generally and as reported in other work the deactivation by poisoning usually leads to a decrease in activity but also there is a possible increase in selectivity. There is even process that intentionally poisons the catalyst to improve its selectivity [48, 49]. In addition to the loss of activity there is also a loss in selectivity as conversion increases. The samples with lower sodium content showed better activity and low selectivity and the more selective ones showed low activity, a typical problem of deactivation by poisoning.

For all samples, as the conversion increases, there is a loss in ethylene selectivity, indicated the existence of a deactivation problem, possibly by adsorption poisoning. The sodium ions added to nickel oxide are considered strong acids the poison would be a base (ethylene - weak base) precisely the product of the reaction [48, 50]. The adsorption force of the ethylene formed is very strong, making it difficult to desorption, blocks access for the adsorption of new reagent molecules. This phenomenon prevents or slows the surface diffusion of adsorbed reactants, caused or hindering mass transfer. The diffusional barrier or mass transfer effect was experimentally verified varying molar flows and measuring conversion, as shown in the Figure 41. As there was variation in the conversion and the decrease in the value of the mass ratio of catalyzed by the flow, it is considered that there are effects of mass transfer.

Figure 41: Mass transfer effects

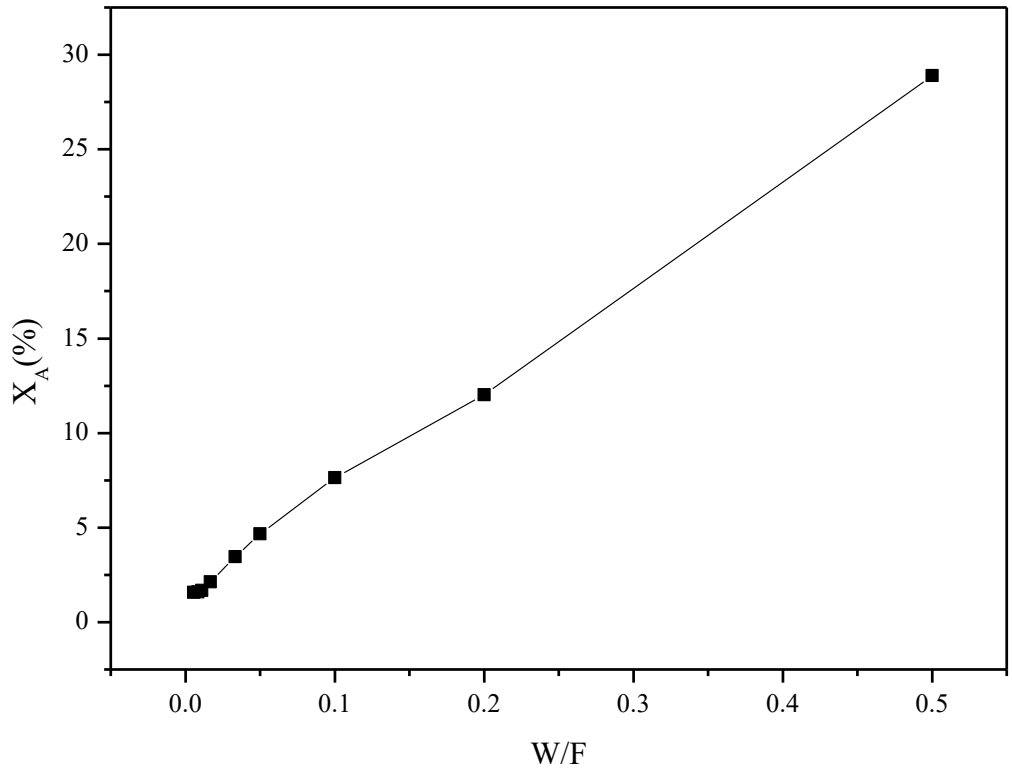

3.2.2 Conclusions

The experimental design used to study a series of nickel mixed oxides solid solution doping with Na^+ cations demonstrated the large effect of the dopant in both the physicochemical properties and the catalytic behavior in the ethane oxidative dehydrogenation reaction. The terms that most influenced the response were the washing and calcination temperature, in all the response variables evaluated. Results obtained for catalytic activity decrease with increase in Na+ concentration, but showing the best selectivity to ethylene. The low Na^+ concentrations showed an increase of the catalytic activity, but with moderate selectivity to ethylene. The maximum yields to ethylene and stability in reaction conditions were obtained at low Na^+ concentrations. Therefore, the addition of sodium indicated benefits promising for ethane ODH, with increasing the ethene selectivity and relatively small drop in reactivity toward ethane as the sodium concentration increases

4 FINAL CONSIDERATIONS AND PERSPECTIVES

In the first sbsection of this work, a clear influence of the precursor was observed on the catalytic behavior of NiO in ethane ODH reaction. This was demonstrated in the form of a different conversion for each catalyst. The apparent activation energy was found to be independent of Ni(III) content and band-gap energy. The best catalytic performance was observed in the oxides in form of nanoparticles, which allows a greater fluidity of the gas mixture and the worst for a sample that hinders the flow. The results suggest that the particles morphology influence in their catalytic performance, especially the microtopoghraphy of the exposed surface of the particles. In the second subsection, all samples showed little variation in selectivity to ethene, with values close to 60%, whatever the calcination temperature or reaction conditions be. The apparent activation energy was found to be independent of Ni(III) content and band-gap energy. Although the activity of the oxide decreased with calcination, as expected from the decrease of specific area, we observed that more crystalline samples displayed the highest intrinsic activity. In subsection three, the nickel mixed oxides solid solution demonstrated the large effect of the dopant in both the physicochemical properties and the catalytic behavior. The catalytic activity decrease with in Na^+ concentrations, but showing the best selectivity to ethylene. The low Na^+ concentrations showed an increase of the catalytic activity, but with moderate selectivity to ethylene. Therefore, the addition of sodium indicated benefits promising for ethane ODH, with increasing the ethene selectivity and relatively small drop in reactivity toward ethane as the sodium concentration increases.

Some further work will be necessary for a better understanding of the physical, chemical and catalytic properties of nickel oxides. For that, I suggest for future works of some characterization techniques as X-ray photoelectron spectroscopy (XPS), characterization of electrical properties and Temperature-programmed reduction techniques. The possibility of in situ characterization of some properties, for a better understanding of the catalyst at the reaction conditions. The possibility of adding a third additive in order to attenuate the acidic properties of the sodium cation thus improving the selective and activated nickel oxide.

5 REFERENCES

1. Tullo AH (2003) Petrochemicals. Chem Eng News Arch 81:21–26. doi: 10.1021/cen-v081n011.p021

2. Zimmermann H, Walzl R (2009) Ethylene. In: Ullmann's Encyclopedia of Industrial Chemistry. Wiley-VCH Verlag GmbH & Co. KGaA, Weinheim, Germany, pp 797–809

3. Ren T, Patel M, Blok K (2006) Olefins from conventional and heavy feedstocks: Energy use in steam cracking and alternative processes. ENERGY 31:425–451. doi: 10.1016/j.energy.2005.04.001

4. Meyers RM and RA (2005) Handbook of Petrochemicals Production Processes, Third. McGraw-Hill Education

5. Cavani F, Trifirò F (1995) The oxidative dehydrogenation of ethane and propane as an alternative way for the production of light olefins. Catal Today 24:307–313. doi: 10.1016/0920-5861(95)00051-G

6. Argyle MD, Chen KD, Bell AT, Iglesia E (2002) Ethane oxidative dehydrogenation pathways on vanadium oxide catalysts. J Phys Chem B 106:5421–5427. doi: 10.1021/jp0144552

7. Martinez-Huerta M V, Gao X, Tian H, et al (2006) Oxidative dehydrogenation of ethane to ethylene over alumina-supported vanadium oxide catalysts: Relationship between molecular structures and chemical reactivity. Catal TODAY 118:279–287. doi: 10.1016/j.cattod.2006.07.034

8. LeBars J, Auroux A, Forissier M, Vedrine JC (1996) Active sites of V2O5/gamma-Al2O3 catalysts in the oxidative dehydrogenation of ethane. J Catal 162:250–259. doi: 10.1006/jcat.1996.0282

9. Tsilomelekis G, Christodoulakis A, Boghosian S (2007) Support effects on structure and activity of molybdenum oxide catalysts for the oxidative dehydrogenation of ethane. Catal TODAY 127:139–147. doi: 10.1016/j.cattod.2007.03.026

10. Thorsteinson EM, Wilson TP, Young FG, Kasai PH (1978) The oxidative dehydrogenation of ethane over catalysts containing mixed oxides of molybdenum and vanadium. J Catal 52:116–132. doi: 10.1016/0021-9517(78)90128-8

11. Heracleous E, Lemonidou AA (2006) Ni-Nb-O mixed oxides as highly active and selective catalysts for ethene production via ethane oxidative dehydrogenation. Part II: Mechanistic aspects and kinetic modeling. J Catal 237:175–189. doi: 10.1016/j.jcat.2005.11.003

12. Skoufa Z, Heracleous E, Lemonidou AA (2015) On ethane ODH mechanism and nature of active sites over NiO-based catalysts via isotopic labeling and methanol

sorption studies. J Catal 322:118–129. doi: 10.1016/j.jcat.2014.11.014

13. Popescu I, Skoufa Z, Heracleous E, et al (2015) A study by electrical conductivity measurements of the semiconductive and redox properties of Nb-doped NiO catalysts in correlation with the oxidative dehydrogenation of ethane. Phys Chem Chem Phys 17:8138–8147. doi: 10.1039/c5cp00392j

14. Botella P, Garcia-Gonzalez E, Dejoz A, et al (2004) Selective oxidative dehydrogenation of ethane on MoVTeNbO mixed metal oxide catalysts. J Catal 225:428–438. doi: 10.1016/j.jcat.2004.04.024

15. Gärtner CA, vanVeen AC, Lercher JA (2013) Oxidative dehydrogenation of ethane: Common principles and mechanistic aspects. ChemCatChem 5:3196–3217. doi: 10.1002/cctc.201200966

16. Stephen Craig Arnold ML, Anne Mae Gaffney WC, Ruozhi Song W, Chuen Yuan Yeh E (2010) Process for producting ethylene via oxidative dehydrogenation (ODH) of ethane. 1:1–5

17. Grabowski R (2006) Kinetics of oxidative dehydrogenation of C2-C3alkanes on oxide catalysts. Catal Rev - Sci Eng 48:199–268. doi: 10.1080/01614940600631413

18. Verwey eJW, Haaijman PW, Romeijn FC, Vanoosterhout GW (1950) Controlled-Valency Semiconductors. Philips Res Reports 5:173–187

19. Zboray M, Bell AT, Iglesia E (2009) Role of C-H Bond Strength in the Rate and Selectivity of Oxidative Dehydrogenation of Alkanes. J Phys Chem C 113:12380–12386. doi: 10.1021/jp901595k

20. Mars P, van Krevelen DW (1954) Oxidations carried out by means of vanadium oxide catalysts. Chem Eng Sci 3:41–59. doi: 10.1016/S0009-2509(54)80005-4

21. Batiot C, Hodnett BK (1996) The role of reactant and product bond energies in determining limitations to selective catalytic oxidations. Appl Catal A-GENERAL 137:179–191. doi: 10.1016/0926-860X(95)00322-3

22. Boschloo G, Hagfeldt A (2001) Spectroelectrochemistry of nanostructured NiO. J Phys Chem B 105:3039–3044. doi: 10.1021/jp003499s

23. N. N. Greenwood And A. Earnshaw (1997) Chemistry of the Elements, Oxford: Pe. Butterworth-Heinemann

24. Cox PA (1987) The Electronic Structure and Chemistry of Solids. Oxford University Press, New York

25. Gray TJ, Darby PW (1956) Semi-conductivity and Catalysis in the Nickel Oxide System. J Phys Chem 60:209–217. doi: 10.1021/j150536a017

26. Varghese JJ, Mushrif SH (2017) Insights into the C-H Bond Activation on NiO

Surfaces: The Role of Nickel and Oxygen Vacancies and of Low Valent Dopants on the Reactivity and Energetics. J Phys Chem C 121:17969–17981. doi: 10.1021/acs.jpcc.7b05226

27. Henry CR (1998) Surface studies of supported model catalysts. Surf Sci Rep 31:235–325

28. Taylor HS, A PRSL (1925) A theory of the catalytic surface. Proc R Soc London Ser A, Contain Pap a Math Phys Character 108:105–111. doi: 10.1098/rspa.1925.0061

29. Roldan Cuenya B (2010) Synthesis and catalytic properties of metal nanoparticles: Size, shape, support, composition, and oxidation state effects. Thin Solid Films 518:3127–3150. doi: 10.1016/j.tsf.2010.01.018

30. Chopra N, Claypoole L, Bachas LG (2010) Morphological control of Ni/NiO core/shell nanoparticles and production of hollow NiO nanostructures. J NANOPARTICLE Res 12:2883–2893. doi: 10.1007/s11051-010-9879-4

31. Duraisamy N, Numan A, Fatin SO, et al (2016) Facile sonochemical synthesis of nanostructured NiO with different particle sizes and its electrochemical properties for supercapacitor application. J Colloid Interface Sci 471:136–144. doi: 10.1016/j.jcis.2016.03.013

32. Xie X, Shen W (2009) Morphology control of cobalt oxide nanocrystals for promoting their catalytic performance. Nanoscale 1:50–60. doi: 10.1039/b9nr00155g

33. Li Y, Liu Q, Shen W (2011) Morphology-dependent nanocatalysis: metal particles. Dalt Trans 40:5811–5826. doi: 10.1039/c0dt01404d

34. Liang X, Xiao J, Gou Y, Chen B (2011) Synthesis and catalysis properties of NiO flower-like spheres and nanosheets: Water-induced phase transformation of nickel hydroxides. J Mater Res 26:3091–3097. doi: 10.1557/jmr.2011.375

35. Kang YC, Park SB, Kang YW (1995) Preparation of High-Surface-Area Nanophase Particles by Low-Pressure Spray-Pyrolysis. Nanostructured Mater 5:777–791. doi: 10.1016/0965-9773(95)00289-Q

36. Wu Y, He Y, Wu T, et al (2007) Effect of synthesis method on the physical and catalytic property of nanosized NiO. Mater Lett 61:2679–2682. doi: 10.1016/j.matlet.2006.10.022

37. Abbas SA, Jung K-D (2016) Preparation of mesoporous microspheres of NiO with high surface area and analysis on their pseudocapacitive behavior. Electrochim Acta 193:145–153. doi: 10.1016/j.electacta.2016.02.054

38. Roberts MW, Smart Rs (1984) The Defect Structure of Nickel-Oxide Surfaces as Revealed by Photoelectron-Spectroscopy. J Chem Soc Trans I 80:2957–2968. doi: 10.1039/f19848002957

39. Wepfer GG, Surratt GT, Weidman RS, Kunz AB (1980) Theoretical-Study of H Chemisorption on Nio .2. Surface And 2nd-Layer Defects. Phys Rev B 21:2596–2601. doi: 10.1103/PhysRevB.21.2596

40. Moroney LM, Smart RS, Roberts MW (1983) Studies of The Thermal-Decomposition Of Beta-Nio(OH) and Nickel Peroxide by X-Ray Photoelectron-Spectroscopy. J Chem Soc Trans I 79:1769–1778. doi: 10.1039/f19837901769

41. Heracleous E, Lemonidou AA (2006) Ni-Nb-O mixed oxides as highly active and selective catalysts for ethene production via ethane oxidative dehydrogenation. Part I: Characterization and catalytic performance. J Catal 237:162–174. doi: 10.1016/j.jcat.2005.11.002

42. Che M, Tench AJ (1982) Characterization and Reactivity of Mononuclear Oxygen Species on Oxide Surfaces. Adv Catal 31:77–133. doi: 10.1016/S0360-0564(08)60453-8

43. Savova B, Loridant S, Filkova D, Millet JMM (2010) Ni-Nb-O catalysts for ethane oxidative dehydrogenation. Appl Catal A-GENERAL 390:148–157. doi: 10.1016/j.apcata.2010.10.004

44. Zhao X, Susman MD, Rimer JD, Bollini P (2021) Tuning selectivity in nickel oxide-catalyzed oxidative dehydrogenation of ethane through control over non-stoichiometric oxygen density. Catal Sci Technol 11:531–541. doi: 10.1039/d0cy01732a

45. Dubey P, Kaurav N, Devan RS, et al (2018) The effect of stoichiometry on the structural, thermal and electronic properties of thermally decomposed nickel oxide. RSC Adv 8:5882–5890. doi: 10.1039/c8ra00157j

46. Lin C, Al-Muhtaseb SA, Ritter JA (2003) Thermal treatment of sol-gel derived nickel oxide xerogels. J SOL-GEL Sci Technol 28:133–141. doi: 10.1023/A:1025653607374

47. Akinkuade S, Mwankemwa B, Nel J, Meyer W (2018) Structural, optical and electrical characteristics of nickel oxide thin films synthesised through chemical processing method. Phys B-Condensed Matter 535:24–28. doi: 10.1016/j.physb.2017.06.021

48. Zhu Z, Wei N, Liu H, He Z (2011) Microwave-assisted hydrothermal synthesis of Ni(OH)(2) architectures and their in situ thermal convention to NiO. Adv POWDER Technol 22:422–426. doi: 10.1016/j.apt.2010.06.008

49. Getsoian AB, Zhai Z, Bell AT (2014) Band-Gap Energy as a Descriptor of Catalytic Activity for Propene Oxidation over Mixed Metal Oxide Catalysts. J Am Chem Soc 136:13684–13697. doi: 10.1021/ja5051555

50. Zhang Y, Zhou YJ, Lin JP, et al (2008) Solid-solution phase formation rules for multi-component alloys. Adv Eng Mater 10:534–538. doi: 10.1002/adem.200700240

51. Turky AM (2003) Electrical surface and catalytic properties of NiO as influenced by doping with CuO and Ag2O. Appl Catal A-GENERAL 247:83–93. doi:

10.1016/S0926-860X(03)00089-9

52. Meier GH, Rapp RA (1971) Electrical Conductivities and Defect Structures of Pure NiO and Chromium-Doped NiO. Zeitschrift Fur Phys Chemie-Frankfurt 74:168-. doi: 10.1524/zpch.1971.74.3_6.168

53. Heracleous E, Lemonidou AA (2010) Ni-Me-O mixed metal oxides for the effective oxidative dehydrogenation of ethane to ethylene - Effect of promoting metal Me. J Catal 270:67–75. doi: 10.1016/j.jcat.2009.12.004

54. Solsona B, Lopez Nieto JM, Concepcion P, et al (2011) Oxidative dehydrogenation of ethane over Ni-W-O mixed metal oxide catalysts. J Catal 280:28–39. doi: 10.1016/j.jcat.2011.02.010

55. Tang C-W, Wang C-B, Chien S-H (2008) Characterization of cobalt oxides studied by FT-IR, Raman, TPR and TG-MS. Thermochim Acta 473:68–73. doi: 10.1016/j.tca.2008.04.015

56. Solsona B, Concepcion P, Demicol B, et al (2012) Selective oxidative dehydrogenation of ethane over SnO2-promoted NiO catalysts. J Catal 295:104–114. doi: 10.1016/j.jcat.2012.07.028

57. Zhu H, Ould-Chikh S, Anjum DH, et al (2012) Nb effect in the nickel oxide-catalyzed low-temperature oxidative dehydrogenation of ethane. J Catal 285:292–303. doi: 10.1016/j.jcat.2011.10.005

58. Li Y, Li X, Wang Z, et al (2016) One-step synthesis of Li-doped NiO as high-performance anode material for lithium ion batteries. Ceram Int 42:14565–14572. doi: 10.1016/j.ceramint.2016.06.071

59. Lopez Nieto JM, Solsona B, Grasselli RK, Concepcion P (2014) Promoted NiO Catalysts for the Oxidative Dehydrogenation of Ethane. Top Catal 57:1248–1255. doi: 10.1007/s11244-014-0288-2

60. Schwab GM, Schmid H (1962) Effect of Added Oxides on P-Conducting Nickel Oxide. J Appl Phys 33:426-. doi: 10.1063/1.1777135

61. Van Houten S (1960) Semiconduction In LixNi(1-X)O. J Phys Chem Solids 17:7–17. doi: 10.1016/0022-3697(60)90169-4

62. Bosman AJ, Crevecoeur C (1966) Mechanism Of Electrical Conduction In Li-Doped NiO. Phys Rev 144:763+. doi: 10.1103/PhysRev.144.763

63. Panagopoulos CN, Eloui S (1986) A Study Of Na Doped NiO Surface. Zeitschrift Fur Phys Chemie-Leipzig 267:608–612

64. Pearson RG (1963) Hard and Soft Acids and Bases. J Am Chem Soc 85:3533–3539. doi: 10.1021/ja00905a001

65. Grabowski R, Grzybowska B, Samson K, et al (1995) Effect of Alkaline Promoters on Catalytic Activity Of V2O5/TiO2 And MoO3/TiO2 Catalysts in Oxidative Dehydrogenation of Propane and in Isopropanol Decomposition. Appl Catal A-General 125:129–144. doi: 10.1016/0926-860X(94)00274-6

66. Chen KD, Xie SB, Bell AT, Iglesia E (2000) Alkali effects on molybdenum oxide catalysts for the oxidative dehydrogenation of propane. J Catal 195:244–252. doi: 10.1006/jcat.2000.3025

67. Martinaranda RM, Portela MF, Madeira LM, et al (1995) Effect of Alkali-Metal Promoters on Nickel Molybdate Catalysts and its Relevance to the Selective Oxidation of Butane. Appl Catal A-GENERAL 127:201–217. doi: 10.1016/0926-860X(95)00037-2

68. Yagi S, Ichikawa Y, Yamada I, et al (2013) Synthesis of Binary Magnesium-Transition Metal Oxides via Inverse Coprecipitation. Jpn J Appl Phys 52:. doi: 10.7567/JJAP.52.025501

69. Kong L-B, Deng L, Li X-M, et al (2012) Fabrication of flower-like Ni-3(NO3)(2)(OH)(4) and their electrochemical properties evaluation. Mater Res Bull 47:1641–1647. doi: 10.1016/j.materresbull.2012.03.051

70. Lee P-Y, Lin L-Y (2019) Synthesizing nickel-based transition bimetallic oxide via nickel precursor-free hydrothermal synthesis for battery supercapacitor hybrid devices. J Colloid Interface Sci 538:297–307. doi: 10.1016/j.jcis.2018.11.108

71. Figgis BN, Martin DJ (1966) Magnetic Properties and Structure of Cupric Alphaomega Dicarboxylates. Inorg Chem 5:100-. doi: 10.1021/ic50035a024

72. Zheng YQ, Adam A (1994) Potassium Trans-Tetraquardicarbonatonickelate(Ii), K2{[}NI(CO3)2(H2O)4]. Acta Crystallogr Sect C-Crystal Struct Commun 50:1422–1424. doi: 10.1107/S0108270193012855

73. Scherrer P (1918) Bestimmung der Grosse und der inneren Struktur von Kolloidterilchen mittels Rontgestrahlen. Nachrichten von der Gesellschaft der Wissenschaften zu Göttingen, Math Klasse 98–100

74. Young RA (1993) The Rietveld Method.Oxford University Press, 298 p

75. Kubelka P MF (1931) An article on optics of paint layers. Z Tech Phys, 12:593–609

76. Tauc J, Menth A (1972) States in the gap. J Non Cryst Solids 8–10:569–585. doi: 10.1016/0022-3093(72)90194-9

77. Hall DS, Lockwood DJ, Bock C, MacDougall BR (2015) Nickel hydroxides and related materials: a review of their structures, synthesis and properties. Proc R Soc A-MATHEMATICAL Phys Eng Sci 471:. doi: 10.1098/rspa.2014.0792

78. Nakamoto K (1986) Infrared and Raman Spectra of Inorganic Coordination

Compounds 4th ed Wiley-Interscience, New York, 95 p.

79. Delmas C, Tessier C (1997) Stacking faults in the structure of nickel hydroxide: a rationale of its high electrochemical activity. J Mater Chem 7:1439–1443. doi: 10.1039/a701037k

80. Tessier C, Haumesser PH, Bernard P, Delmas C (1999) The structure of Ni(OH)(2): From the ideal material to the electrochemically active one. J Electrochem Soc 146:2059–2067. doi: 10.1149/1.1391892

81. Gravelle PC, Teichner SJ (1969) Carbon Monoxide Oxidation and Related Reactions on a Highly Divided Nickel Oxide. Adv Catal 20:167–266. doi: 10.1016/S0360-0564(08)60272-2

82. Biswick T, Jones W, Pacula A, Serwicka E (2006) Synthesis, characterisation and anion exchange properties of copper, magnesium, zinc and nickel hydroxy nitrates. J Solid State Chem 179:49–55. doi: 10.1016/j.jssc.2005.09.040

83. Petrov K, Zotov N, MirtchevA E, et al (1994) Effect of Composition on the Lattice-Parameters and Thermal-Behavior of Nickel(Ii)-Cobalt(Ii) Hydroxide Nitrate Solid-Solutions. J Mater Chem 4:611–614. doi: 10.1039/jm9940400611

84. Rincke C, Bette S, Dinnebier RE, Voigt W (2015) Nickel Bicarbonate Revealed as a Basic Carbonate. Eur J Inorg Chem 5913–5920. doi: 10.1002/ejic.201501094

85. Donia AM (1997) Synthesis, identification and thermal analysis of coprecipitates of silver-(cobalt, nickel, copper and zinc) oxalate. Polyhedron 16:3013–3031. doi: 10.1016/S0277-5387(97)00041-7

86. Puzan AN, Baumer VN, Lisovytskiy V D, Mateychenko V P (2018) Structure transformations in nickel oxalate dihydrate NiC2O4 center dot 2H(2)O and nickel formate dihydrate Ni(HCO2)(2)center dot 2H(2)O during thermal decomposition. J Solid State Chem 266:133–142. doi: 10.1016/j.jssc.2018.07.005

87. Bickley RI, Edwards Hgm, Rose SJ (1991) A Raman-Spectroscopic Study of Nickel(II) Oxalate Dihydrate, NiC2O42H2O, and Dipotassium Bisoxalatonickel(II) Hexahydrate, K2Ni(C2O4)26H2O. J Mol Struct 243:341–350. doi: 10.1016/0022-2860(91)87048-M

88. Li GJ, Huang XX, Shi Y, Guo JK (2001) Preparation and characteristics of nanocrystalline NiO by organic solvent method. Mater Lett 51:325–330. doi: 10.1016/S0167-577X(01)00312-3

89. Pease WR, Segall RL, Smart RSC, Turner PS (1986) Surface reduction in low-temperature formation of nickel oxide from different nickel salts. Thermal analysis, surface area, electron microscopy and infrared studies. J Chem Soc Faraday Trans 1 Phys Chem Condens Phases 82:747–758. doi: 10.1039/F19868200747

90. Bakovets V V, Trushnikova LN, Korol'kov I V, et al (2009) Synthesis of nanostructured nickel oxide. Russ J Gen Chem 79:356–361. doi:

10.1134/S1070363209030049

91. Santander J, Lopez E, Diez A, et al (2014) Ni-Nb mixed oxides: One-pot synthesis and catalytic activity for oxidative dehydrogenation of ethane. Chem Eng J 255:185–194. doi: 10.1016/j.cej.2014.06.048